Technische Universität München

Physik Department

MPQ

State Selective Fluorescence Detection of Cold Formaldehyde

Martin Ibrügger

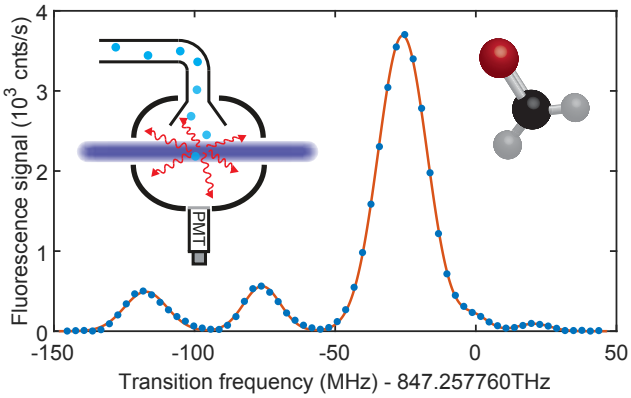

Dissertation

Max-Planck-Institut für Quantenoptik, Garching
and Physik Department, Technische Universität München

January 2021

Cover illustration: The figure shows a UV spectrum of cold formaldehyde (H_2CO) molecules in the presence of an electric field leading to a line splitting allowing to detect individual M-sublevels. The inset shows an illustration of the detection setup and a sketch of the chemical structure of formaldehyde.

Technische Universität München

Fakultät für Physik

State Selective Fluorescence Detection of Cold Formaldehyde

Martin Ibrügger

Vollständiger Abdruck der von der Fakultät für Physik der Technischen Universität München zur Erlangung des akademischen Grades eines

Doktors der Naturwissenschaften (Dr. rer. nat.)

genehmigten Dissertation.

Vorsitzender :		Prof. Dr. Johannes Knolle
Prüfer der Dissertation :	1.	Hon.-Prof. Dr. Gerhard Rempe
	2.	Prof. Dr. Reinhard Kienberger

Die Dissertation wurde am 17.02.2021 bei der Technischen Universität München eingereicht und durch die Fakultät für Physik am 08.11.2021 angenommen.

Abstract

The long ranged dipole-dipole interaction and rich internal level structure of polar molecules render them ideal candidates for applications ranging from quantum information processing to high precision spectroscopy. A prerequisite for these applications is a high level of control over the external and internal degrees of freedom of the molecules. Optoelectrical Sisyphus cooling has proven to be capable of cooling formaldehyde (H_2CO) to sub-millikelvin temperatures, hence bridging the gap for chemically diverse species to the ultracold temperature regime. In this thesis the design and implementation of a continuous wave optical detection scheme based on laser induced fluorescence (LIF) for Sisyphus cooled formaldehyde is presented. The state selectivity of the method is then exploited to prepare the molecules in their rotational ortho ground state. Furthermore, a coherence measurement between specific rotational states is developed and demonstrated.

The detection relies on electronic excitation of the molecules by a UV-laser via the $\tilde{A}^1A_2 \leftarrow \tilde{X}^1A_1\ 4_0^1$ transition and the subsequent spontaneous decay of the molecules under the emission of fluorescence light. Due to a bad Franck-Condon overlap there is no cycling transition available and efficient collection of the fluorescence light is indispensable. To this end, a light collection optics is designed covering a large solid angle of 75 %. Stray background light is suppressed by a factor of more than 10^9 mainly by performing extensive laser beam cleaning, an intricate in-vacuum aperture setup, and the use of filters. This way a state selective detection scheme is realised which even allows to resolve individual Stark-sublevels and has a rotational state dependent detection efficiency of up to 9 %. Due to the state selectivity, optical pumping of Sisyphus cooled formaldehyde molecules into the ortho ground state can be demonstrated. This is a key step towards loading of the molecules into a microwave trap for further cooling in the future. Finally, specific pairs of rotational states, generic to rigid rotor molecules, which are degenerate at arbitrary electric fields are identified. These states are experimentally distinguished by the creation of coherent superpositions with radio frequency radiation and a coherence time of about 130 µs is determined. This value is limited by the movement of the molecules in the trap and achieving significant increases in the near future should be feasible.

Contents

1 Introduction

Today, experiments are able to exert ultimate control over motion and internal states of atoms. This achievement was mainly spearheaded by the rapid advances in the 80s and 90s of the last century. With the advent of laser cooling [Chu98, CT98, Phi98] the fresh field of ultracold atomic gases evolved at an unprecedented pace coming to a first culmination with the creation of Bose Einstein condensates of alkali atoms [Cor02, Ket02]. This development led to a plethora of exciting applications in the fields of e.g. quantum information processing or precision measurements only enabled by the supreme control achieved over the quantum states and the translational degrees of freedom of atoms. Nowadays, molecular systems have become an area of rapidly increasing interest, with the goal of achieving a similar level of control as for atoms.

Molecules in particular offer two distinct features from atoms. Their rich internal level structure not only consists of electronic excitations and nuclear degrees of freedom but also incorporates rotational and vibrational degrees of freedom which add further interesting properties to molecular systems compared to atomic ones. Furthermore, molecules can have a permanent electric dipole moment enabling the interaction with external electric fields and providing the possibility of a long-ranged anisotropic interaction. Therefore, there is great interest in molecules from a number of different fields ranging from quantum information processing and precision measurements to controlled chemistry and quantum simulation. There are many exciting applications for molecules which have been proposed in the past and some have already been realised. An overview over some of these applications and proposals most relevant for the work presented in this thesis is given in Section 1.1. For a broader and more detailed overview the reader is referred to a number of review articles and books published in recent years [Bel09, Car09, Hog11, vdM12, Lem13, Boh17, Saf18, Koc19].

Most applications require or at least greatly benefit from an increased control over the internal and external degrees of freedom. However, the complexity of molecules, which on one hand makes them much more interesting systems than atoms, on the other hand also renders them much harder to control. Due to the promising applications realisable by achieving quantum state control over ultracold[1] molecules, there is great effort to improve control over molecules despite the experimental challenges. For some simple diatomic species there is a workaround by synthesising the molecules from atoms previously cooled to the ultracold temperature regime. For molecules not accessible to this scheme a number of different techniques is employed for cooling, ranging from laser cooling, which in some cases can be adapted to

[1] Typically, the cold molecule community uses the nomenclature of the atomic community and refers to temperatures $< 1\,\mathrm{K}$ as the cold temperature regime, in contrast to the ultracold temperature regime $< 1\,\mathrm{mK}$.

molecules, over beam experiments to approaches such as optoelectrical Sisyphus cooling which forms the basis for the work of this thesis. An overview over different techniques to cool molecules and gain increasing control is provided in Section 1.2.

A further complication of working with molecules is their detection. The standard technique for atoms, which relies on repeatedly driving an electronic transition and either collecting the fluorescence light or measuring the absorption, is only applicable to a limited number of molecule species due to their complex internal level structure. Since the first part of this thesis deals with the implementation of a detection scheme for the special case of formaldehyde, an overview of different techniques used for the detection of molecules is given in Section 1.3. Finally, an overview of the work in this thesis is presented in Section 1.4.

1.1 Applications of cold molecules

Precision measurements An important area of application for cold molecules is the field of high precision measurements which pursues the main goal of testing fundamental physical theories [Wal16, Saf18]. Here, a prime example is the search for the electron's electric dipole moment (eEDM) where molecules have intrinsic advantages over atomic systems due to high effective internal electric fields and a lower susceptibility to systematic effects [Hin97]. The precision of atomic systems was first surpassed in 2011 at Imperial college with the molecule YbF [Hud11]. To date, the most precise upper bound for the eEDM is set by the ACME collaboration in ThO with $|d_e| < 1.1 \times 10^{-29}\, e\,\mathrm{cm}$ [ACM18] with another order of magnitude increase in sensitivity in sight [Pan19, Wu20]. Both groups work with molecular beams resulting in a limited interrogation time and would benefit greatly from being able to work with a trapped cloud of ultracold molecules [Cai19]. Another promising complementary approach is being followed by the Cornell group at JILA where the molecular ion HfF^+ is employed [Cai17, Zho20].

Molecular systems are not only sensitive to a non-vanishing eEDM, but also to other fundamental constants such as the proton-electron mass ratio and the fine structure constant [Tru13, Bie16]. For the diatomic molecule Sr_2 Zelevinsky and coworkers recently demonstrated a vibrational molecular lattice clock with a quality factor of 8×10^{11}, which in the future can also provide further insight into fundamental physics [Kon19].

Cold collisions and chemistry Another very broad field of applications for cold and ultracold molecules is the investigation of chemical reactions and collisions between these molecules which is described in a number of review and special issue articles [Car09, Kre09, Dul11, Jin12, Lem13, Doy16, Bal16, Boh17]. At sufficiently low temperatures many reactions are suppressed by potential barriers. Nonetheless, due to tunnelling, reaction resonances are predicted to appear and were first observed in the case of the Penning ionisation reaction of He with molecular hydrogen [Hen12]. Particularly interesting is the possibility to adjust reaction rates with external fields [Kre05, Tsc15]. This has been demonstrated for the polar molecule KRb [Ni10] where the molecular gas close to quantum degeneracy shows an in-

creased loss rate depending on the applied electric fields. The investigation of reactions in a gas of ultracold KRb has recently been intensified by the Ni group at Harvard that could directly observe reaction intermediates [Hu19] and furthermore, steer reaction pathways via this short-lived intermediate [Liu20b]. For this type of molecule an important loss process turned out to be 'sticky collisions', where the colliding molecules stay in relatively long-lived two-molecule collision complexes enabled by the high density of rovibrational states in molecules, leading to an increase in losses [May12, May13, Chr19, Cro20]. This is experimentally confirmed by the mentioned experiment with KRb [Hu19, Liu20b] as well as in RbCs [Gre19].

This type of controlled chemistry experiments at the time being is limited to molecules accessible to 'indirect' cooling methods (see Section 1.2) which can only address a few diatomic species consisting of alkali atoms. For the investigation of chemical reactions with a similar level of control with chemically more diverse species, 'direct' cooling methods have to advance further. Nonetheless, first dipolar collisions have been observed within an electric quadrupole guide for CH_3F and ND_3 molecules [Wu17]. By cotrapping O_2 and Li in a magnetic trap [Ake17] an increased loss rate has been observed, demonstrating losses due to collisions between trapped molecules and atoms. For directly laser cooled CaF molecules loaded into an optical tweezer [And19] an increased two-particle loss rate is observed compared to loading only a single molecule [Che20].

Quantum information processing As a final application, polar molecules have been proposed as ideal candidates for quantum information processing applications. The strong electric dipole moment allows for a long ranged dipole-dipole interaction for e.g. gate operations, whereas the stable rotational states provide ideal qubit storage possibilities [Koc19]. A first proposal from D. DeMille dates back to 2002 [Dem02] where polar molecules are placed in an one-dimensional array with an electric field gradient which allows addressing of the individual sites. The dipole-dipole interaction can be exploited to create entanglement between the trapped molecules. In Ref. [Wei11] it is pointed out that using symmetric rotor molecules for such a system is advantageous due to the low electric fields needed as a consequence of their linear Stark shift and the fact that the effective dipole moment is nearly independent from the applied electric field. Other proposals based on polar molecules investigate the possibility to turn the dipole-dipole interactions between the molecules 'on' and 'off' by switching between states with high and low electric dipole moments in order to allow for robust quantum computation [Yel06, Kuz08]. An alternative approach consists of coupling polar molecules to a microwave stripline resonator [And06, Rab06, Rab07] which could help to overcome the issue of fast decoherence typically present in solid-state systems. In a recent proposal by Yu et al., the possibility is discussed to trap certain types of symmetric top molecules, which in principle should be laser coolable, in an optical array [Yu19]. Individual lattice sites could be addressed by tightly focussed laser beams and by changing the internal states of the molecules appropriately, universal quantum gates should be realisable.

All of the above proposals require ultracold trapped molecules with exquisite internal state control. First steps into this direction have already been taken. For

indirectly cooled ultracold NaK molecules a coherence time between nuclear spin states on the order of 1 s has been achieved [Par17]. Between rotational states coherence times of 0.75 ms and 0.61 ms have been reported for two very different systems, namely optically trapped RbCs and magnetically trapped CaF [Bla19]. For the latter system Caldwell et al. have recently improved the result to 6.4 ms by using rotational states with exceptionally low magnetic sensitivity [Cal20]. The measurements presented in the last chapter of this thesis directly line up with these results, as for the polyatomic slightly asymmetric rotor formaldehyde a coherence time between rotational states insensitive to electric fields of $> 100\,\mu s$ is shown (see Chapter 6).

1.2 Cooling techniques for molecules

As mentioned previously, cooling techniques for molecules can generally be separated into two categories. For 'indirect' cooling techniques molecules are synthesised from atoms previously cooled to ultracold temperatures. 'Direct' cooling refers to techniques which work with preexisting molecules.

Indirect cooling methods To create a gas of ultracold diatomic molecules the constituent atoms can be cooled by conventional techniques, i.e. laser-cooling, and subsequently diatomic molecules can be forged from these atoms. By scanning a magnetic field over a Feshbach scattering resonance, vibrationally highly excited molecules can be formed. The molecules are then brought into the ground state via coherent state transfer (STIRAP). This technique was first demonstrated for polar molecules in 2008 where a gas of ultracold KRb near quantum degeneracy was produced [Ni08]. Due to extraordinary experimental challenges involved with this type of experiment only in recent years this feat could be repeated for molecules such as RbCs [Tak14, Mol14], NaK [Par15, See18, Vog20], and NaRb [Guo16]. Most recently the development culminated in the creation of a quantum-degenerate Fermi gas of KRb molecules with a temperature of 0.3 times the Fermi temperature [De 19].

Another indirect approach to cooling of molecules is photoassociation where two ultracold atoms are electronically excited such that a bound, electronically excited molecule is formed. The excess energy is removed via the emission of a photon. This technique was first demonstrated for Cs_2 [Fio98] but has since then also been applied to the creation of polar molecules [Sag05, Dei08]. However, the temperatures and densities achieved with photoassociation are not competitive with the ones that have been demonstrated with Feshbach association.

While these indirect cooling methods are able to produce the coldest temperatures and highest phase-space densities to date, their applicability is limited to a few diatomic molecule species whose constituent atoms can be laser cooled. At the time being only molecules consisting of alkali atoms have been demonstrated, but there are also efforts to extend the schemes to earth-alkali atoms [Bar18].

Direct cooling methods In order to bring chemically more diverse molecules species into the cold or ultracold temperature regime direct cooling methods have to be ap-

plied which work with already preexisting molecules.

A particularly simple and robust approach to create molecules samples at cold temperatures applicable to a wide variety of species is velocity filtering. The basic idea relies on the fact that a thermal gas contains a certain number of very slow and cold molecules. By inserting such a gas into a finite potential of e.g. an electric quadrupole guide, only the molecules below a certain threshold are trapped. Strictly speaking this method does not cool, however, it has been employed very successfully for the creation of high flux molecule beams of polyatomic molecules [Ran03]. The technique can produce velocities $< 10\,\frac{\mathrm{m}}{\mathrm{s}}$ which are ideal for trapping of the molecules [Eng11]. For this work, the first step to produce cold molecules samples is velocity filtering of molecules inserted via a liquid nitrogen cooled nozzle into a quadrupole guide (see Section 2.2.2).

Another technique to provide cold molecules is supersonic expansion which relies on letting a high pressure gas expand into vacuum. Due to collisions during the expansion the internal and external degrees of freedom of the molecules are cooled. However, they move at a fast velocity on the order of $400\,\frac{\mathrm{m}}{\mathrm{s}}$. In order to slow this molecule beam down, a number of deceleration techniques have been developed which are summarised in two review papers [Hog11, vdM12] and only a few examples are presented here. The approach of a Stark decelerator relies on the switching of electric fields, such that the moving molecule beam continuously experiences a potential hill, and was first demonstrated for the molecule CO by Bethlem et al. [Bet99]. For paramagnetic molecules a moving trap Zeeman decelerator can be employed where the molecules are trapped in a rapidly moving magnetic potential which is brought to a stand-still to slow down the molecules. This technique has been used successfully to load molecular oxygen into a magnetic trap [Ake17].

In order to create a slow beam of internally cold molecules buffer gas cooling is used which is reviewed in Ref. [Hut12]. The molecules are cooled by collisions with a cryogenic inert buffer gas, typically He or Ne, and the technique is applicable to almost any type of molecule. It has been used for cooling of naturally occurring molecules such as ND_3 and H_2CO from a room temperature source [vB09] but also for molecules created within the buffer gas cell by laser ablation at temperatures of $\sim 1000\,\mathrm{K}$ [Max05]. Upon extraction of the molecules from the cell they typically have a forward velocity of about $100\,\frac{\mathrm{m}}{\mathrm{s}}$ and therefore still have to be slowed. However, using the above mentioned conventional Stark and Zeeman decelerators is difficult due to a continuous, or at least very broad, molecule output. Therefore, other slowing techniques have to be employed. A very versatile method is using a centrifuge decelerator where the molecules have to overcome a centrifugal potential barrier on a rotating disc and are hence decelerated efficiently [Che14]. With this apparatus a flux exceeding $1 \times 10^{10}\,\frac{1}{\mathrm{s}}$ at velocities $< 20\,\frac{\mathrm{m}}{\mathrm{s}}$ could be realised for the molecules ND_3, CH_3F and CF_3CCH making it an ideal option for loading of a trap [Wu17]. A different approach applicable to molecules which can be laser cooled (see next paragraphs) is laser slowing which was first demonstrated for SrF [Bar12]. Most notably, it was used to slow a beam of CaF such that the velocity spread is compressed by a factor of 10 by using chirped laser pulses [Tru17a]. Other proposals include a continuous Zeeman slower for molecules which up to now only has been tested for atoms [Pet18] and a Zeeman-Sisyphus decelerator [Fit16]. However, these

techniques have in common that they are only applicable to a limited number of molecule species which are laser coolable.

The direct cooling techniques mentioned up to now are only suitable to bring molecules into the temperature regime between about 1 K and 1 mK. To bring molecules into the ultracold temperature regime it is indispensable to first trap the molecules and then apply a suitable cooling mechanism. Currently, the main focus in the community lies on advancing the standard techniques used by the atomic community, namely magneto-optical trapping (MOT) and laser cooling of molecules. Since this technique requires to scatter a huge number of photons, an optical cycling transition is needed which is only available for a limited number of molecules species with favourable Franck-Condon factors. After an electronic excitation these molecules preferentially decay back into the vibrational ground state limiting the number of repumping lasers needed to achieve a closed cooling cycle. First transverse laser cooling of the molecules SrF was shown already in 2010 by Shuman et al. [Shu10] with a first MOT of the same molecule species realised in 2014 by Barry et al. [Bar14]. After M. Tarbutt had worked out the detailed working principle of a molecular MOT [Tar15], laser cooled molecules first entered the ultracold temperature regime, again for the molecule SrF, in 2016 where a temperature of 400 µK was achieved [Nor16a]. Since then the field has been progressing rapidly and a temperature of about 50 µK has been achieved with gray molasses cooling for the molecules CaF [Tru17b, And18] and SrF [McC18]. By improving the cooling scheme with velocity selective coherent population trapping even lower temperatures of about 5 µK could be achieved for CaF [Che18, Cal19] and most recently also for YO [Din20]. As a consequence of this rapid development some of these molecules have now been transferred into magnetic traps [McC18, Wil18], dipole traps [And18], and optical tweezers [And19]. Laser cooling is also under development for a number of other species such as BaH [Iwa17], MgF [Xu19], BaF [Che17, Alb20], AlF [Tru19], and also for polyatomic metal hydride radicals such as SrOH [Koz17], CaOH [Bau21], YbOH [Aug20] or $CaOCH_3$ [Mit20].

Despite the recent advances and growing interest, laser cooling is still only applicable to a specific class of molecule species. The Rempe/Zeppenfeld group pursues an alternative approach which does not rely on a good Franck-Condon overlap and hence addresses a complementary group of molecules with different properties. Optoelectrical Sisyphus cooling, unlike laser cooling, does not rely on the photon recoil but exploits the strong interaction of the permanent electric dipole moment of polar molecules with electric fields to create a dissipative cooling process [Zep09]. Cooling takes place in an electric trap [Eng11] and the scheme is in principle applicable to many polar polyatomic molecules. Cooling was first demonstrated for the symmetric rotor molecule CH_3F which was cooled down to a temperature of 29 mK [Zep12]. Cooling to ultracold temperatures could be demonstrated for the slightly asymmetric rotor molecule H_2CO which was cooled to a temperature of 420 µK [Pre16]. This is the cooling scheme which is employed for the work of this thesis.

1.3 Detection of cold molecules

For the detection of cold molecules there are a number of techniques available which can in general be divided into two categories. Either charges, resulting from ionisation of the molecules, or photons, typically following an electronic excitation of the molecules, are detected.

Arguably, the simplest method to detect molecules via their ionisation products is through a quadrupole mass spectrometer (QMS). An electron beam ionises the molecules and the products are guided by an AC quadrupole guide filtering a certain particle mass to an ion detector [Pau53]. The spectrometers are commercially available and the detection method is robust and can quickly be adjusted to detect different molecule species. In particular in the Zeppenfeld/Rempe group it was used with great success in a variety of experiments involving different molecule species [Zep12, Glö15a, Pre16, Wu17]. A caveat of the method is its low detection efficiency and the lack of state selectivity, even though the latter point could be addressed by performing intricate difference measurements [Glö15b].

Another technique based on the detection of charges is resonance enhanced multiphoton ionisation (REMPI) where molecules are excited with high intensity UV laser pulses above their ionisation threshold via a multiphoton transition. This technique has been demonstrated for many different molecule species such as O_2 [Epp97, Ake17], ND_3 [Bet00], NO [Kir13], CH_3F [Men15], or OH [Gra17] and typically rotational state selectivity can be achieved. For formaldehyde there are also a number of REMPI schemes available [Par16], however, they have not yet been employed for the detection of cold H_2CO. Detection of molecules via REMPI has also been combined with velocity map imaging (VMI) which by using ion lenses images charges originating from different positions with equal velocities onto the same position where they can be detected by a multi channel plate, hence providing a velocity resolving detection [Epp97, QP12, vZ14].

When a detection scheme is based on the detection of photons, typically laser induced fluorescence (LIF) is the chosen method which is based on electronic excitation of the molecule and a subsequent decay under emission of a fluorescence photon. For molecules used for laser cooling this is straightforward as they feature a cycling transition which allows to extract a huge number of photons per molecule. Therefore, detection via LIF is the standard technique for the molecule species mentioned above which are being laser cooled. The good signal-to-noise ratio that can be achieved also allows for a precise determination of the temperature of the molecule cloud by measuring its expansion in the absence of confining laser beams [Nor16a, Tru17b, Che18, Cal19].

In the absence of a cycling transition, detection via LIF is more complicated. Signal levels are very low because only a single photon can be extracted from each molecule, making stray light from the excitation laser a problem. Therefore, the detection signal is typically gated with a pulsed molecules source or by using a pulsed laser. This way many molecules species could be detected such as H_2CO [Hud06], YbF [Hud11], NO [Wan13], and OH [Sch16]. A large part of this thesis is dedicated to the implementation of such a detection scheme for H_2CO, however, with the added difficulty of a continuous wave detection.

For indirectly cooled molecules consisting of alkali atoms there typically is no cycling transition available, which is why this type of molecules for detection is dissociated into its constituents which both feature cycling transitions and are easily detected via either fluorescence or absorption imaging [Liu20a]. For very dilute samples a better option can again be ionisation of the molecules by e.g. REMPI which can also detect reaction intermediates or in combination with VMI provide information about the molecules' velocity [Aik10, Liu20a].

Generally, absorption can be a powerful tool to detect molecules as it can also provide deep insights into molecular kinetics [Spa16]. However, typically samples are not dense enough for this technique to be commonly applied. Nevertheless, for astrophysical sources of molecules, where absorption is the only possible way of detection, it is of immense importance [Lac17].

A potential indirect detection technique for cold molecules could be to measure their interaction with Rydberg atoms as proposed by M. Zeppenfeld [Zep17]. Via Förster resonant energy transfer during collisions of molecules with Rydberg atoms the resulting state change in the Rydberg atom can provide a non-destructive way of detecting molecules [Jar18].

1.4 This thesis

This thesis is dedicated to the design and experimental implementation of an optical detection of H_2CO based on laser induced fluorescence for an experiment cooling this molecule via optoelectrical Sisyphus cooling. Furthermore, the state selectivity of the detection is exploited for rotational ortho ground state pumping of H_2CO and first experiments towards achieving long coherence times between rotational states of this molecule.

The necessary background of molecular theory is presented in **Chapter 2** with a focus on the derivation of selection rules via the symmetry properties of the molecule and their interaction with external fields. Additionally, the optoelectrical cooling scheme and the preexisting experimental setup are shortly summarised. The basic idea of a detection of H_2CO via laser induced fluorescence and the experimental apparatus constructed to this end is explained in **Chapter 3**. Particular emphasis is set on the suppression of stray light via laser beam cleaning and an in-vacuum setup of apertures. The detection scheme is characterised in detail in **Chapter 4** and its state selectivity which can even resolve individual M-sublevels is demonstrated. Furthermore, excited state lifetimes of the involved transitions are measured and a quantum yield is extracted which is subsequently used to determine the detection efficiency. As a first application of the detection Sisyphus cooled molecules are prepared in their rotational ortho ground state by optical pumping in **Chapter 5**. These molecules are then used to demonstrate a coherence time between rotational states of H_2CO in **Chapter 6**. In particular, the process on how to distinguish these states in the given setup is theoretically outlined and demonstrated experimentally. Finally, the thesis concludes with an outlook in **Chapter 7** summarising the measurements enabled by the new detection scheme, future applications of the investigated rotational states, and the envisioned future of the experiment.

2 Theoretical and experimental foundations

This chapter discusses the theoretical and experimental basis needed for understanding the experiments presented in this thesis. Only a short overview of the most relevant aspects is given as for many topics a detailed discussion is already presented in previous theses from the Rempe group. The Hamiltonian of the rigid rotors including the interaction with electric fields is presented in the thesis of Christian Sommer [Som11]. Alexander Prehn focussed on the rotational states of formaldehyde and the possibility to describe their interaction with electric fields by a two-level approximation [Pre18], whereas a numerical solution was presented in this authors diploma thesis [Ibr13]. In the diploma thesis of Erich Dobler a summary of how the molecular structure and symmetry lead to electric dipole selection rules is given [Dob16]. A description of the experimental setup can be found in the theses of Barbara Englert [Eng13] and Alexander Prehn [Pre18]. The design of the electric trap for confining the molecules is described in great detail in the thesis of Martin Zeppenfeld [Zep13]. All these topics are only summarised as a comprehensive treatment can be found in the original literature or text books and citations for further reading are provided in each section.

The molecular theory background for this thesis is provided in Section 2.1. The discussion is mainly limited to the special case of the asymmetric rotor formaldehyde as all presented measurements are performed with this molecule. After introducing the structure of formaldehyde, vibronic excitations are discussed and the corresponding selection rules are derived from symmetry considerations. Following this, rotational states are examined and a brief overview of the hyperfine structure of formaldehyde is given. Finally, the interaction with externally applied electric and magnetic fields is presented. In Section 2.2 the employed cooling scheme, optoelectrical Sisyphus cooling, is presented followed by an overview of the experimental apparatus.

2.1 Theory of formaldehyde H_2CO

Formaldeyhde is a naturally occurring molecule relevant to many areas of science. It is part of the present day Earth's atmosphere [Bur99] and is believed to also have occurred in the primitive Earth's atmosphere [Pin80]. It can be found in comets [Sch93] as well as in interstellar clouds [Man08a]. Formaldehyde, despite being polyatomic, still has a relatively simple structure and is a prototype molecule for photochemistry of small molecules [Moo83]. It has various favourable properties such as a sharp absorption spectrum and accessible frequency ranges which together with the aforementioned reasons make it one of the best studied molecules to date [Clo83].

Already almost a century ago the near- and mid-UV spectrum of formaldehyde was investigated in detail [Hen28] and the interest in this molecule continues on to the present day with e.g. precise studies in the submillimeter wavelength regime [Mül17].

A comprehensive treatment of the theory of asymmetric rotor molecules, their structure and resulting energy levels as well as the interaction with external fields can be found in the original literature. These topics are also discussed in great detail in text books [Her66, Gor70, Kro75, Tow75, Dem03, Bun06, Her15]. The purpose of this section is to give a short summary of the basic theory crucial for understanding the measurements presented in this thesis. For most of this section a fully separable wavefunction Ψ_{tot} is assumed [Bun06]. In the Born-Oppenheimer approximation the movement of the electrons is assumed to be much faster than the movement of the nuclei which justifies the separation of the electronic and vibrational wavefunction. Furthermore, in the rigid rotor model there is no interaction between the rotation and vibration of the molecule. Neglecting the influence of hyperfine interaction on the molecular energy, the complete wavefunction can then be separated

$$\Psi_{\mathrm{tot}} = \Psi_{\mathrm{elec}}\Psi_{\mathrm{vib}}\Psi_{\mathrm{rot}}\Psi_{\mathrm{nspin}} \tag{2.1}$$

where Ψ_{elec} is the electronic wavefunction, Ψ_{vib} the vibrational wavefunction, Ψ_{rot} the rotational wavefunction and Ψ_{nspin} the nuclear spin wavefunction. Even including these approximations, solving the Schrödinger equation can be very challenging, in particular for the electronic degrees of freedom. However, by applying group theory, which is a very powerful tool in molecular physics, to the individual components of the wavefunction, a number of useful qualitative results such as selection rules can be derived. To this end, it is instructive to investigate the structure of formaldehyde. A detailed treatment of group theory and its application to molecules can be found in Ref. [Bun06].

Structure of formaldehyde Formaldehyde is a four-atomic molecule with the empirical formula H_2CO. In its electronic ground state[1] $\tilde{X}^1A_1$ it is a planar molecule and its structure is shown in Fig. 2.1(a). The molecule fixed coordinate system $\alpha = (x, y, z)$ is shown together with the principal axes (a, b, c). The coordinate system's assignment is in principle arbitrary and here the recommendations by Mulliken for molecules of point group $\boldsymbol{C}_{2v}$, to which formaldehyde belongs, are followed [Mul55][2]. The principal axes mapping is given by the I^r representation which assigns an axis to the ordered number of rotational constants $A > B > C$ [Kin43]. This particular representation is most convenient for prolate asymmetric tops as it minimizes off-diagonal elements in the rotational Hamiltonian (see Section 2.1.2). Formaldehyde is a polar molecule with a permanent electric dipole moment μ of 2.33 D which in the vibronic ground state points along the internal axis a [Fab77].

[1] The first letter $\tilde{X}$ symbolises the electronic ground state with the spin multiplicity $2S + 1$ as superscript. It is followed by the irreducible representation of the wavefunction. Electronically excited states are labelled in the same way except that the initial letter is exchanged by $\tilde{A}$, $\tilde{B}$, $\tilde{C}$, etc. for electronically excited singlet states and $\tilde{a}$, $\tilde{b}$, $\tilde{c}$, etc. for triplet states [Her66].

[2] The recommendations by Mulliken are not followed consistently in the literature. This results mainly in an inconsistent definition of the B_1 and B_2 irreducible representation of the point group $\boldsymbol{C}_{2v}$.

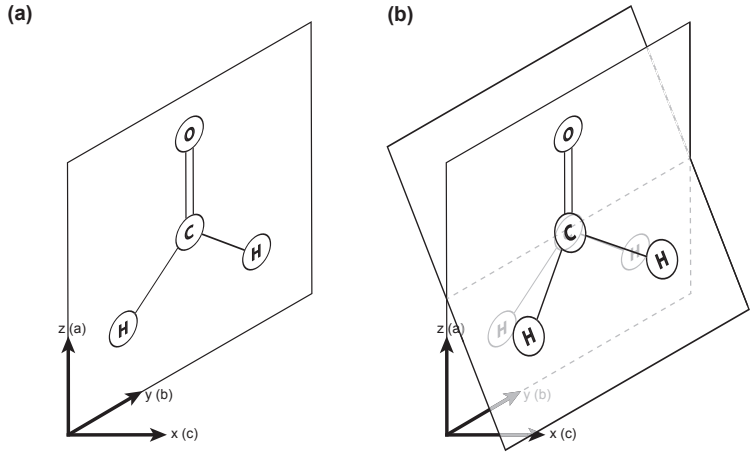

Figure 2.1: Structure of formaldehyde. The molecule fixed axes x, y and z are assigned following the recommendation by Mulliken for the point group $\boldsymbol{C}_{2v}$ [Mul55]. a, b and c are the principal axes of the molecule according to the I^r representation [Kro75]. **(a)** Planar structure of the electronic ground state $\tilde{X}^1A_1$. **(b)** Pyramidal structure of the first electronically excited state $\tilde{A}^1A_2$ where the hydrogen atoms are tilted out of the original plane.

$\boldsymbol{C}_{2v}$	E	C_2	σ_{xz}	σ_{yz}			
A_1	$+1$	$+1$	$+1$	$+1$	T_z		v_1, v_2, v_3
A_2	$+1$	$+1$	-1	-1		R_z	
B_1	$+1$	-1	$+1$	-1	T_x	R_y	v_4
B_2	$+1$	-1	-1	$+1$	T_y	R_x	v_5, v_6

Table 2.1: Character table of the point group of formaldehyde $\boldsymbol{C}_{2v}$. It consists of the symmetry operations unity E, two-fold rotation C_2 and two planes of symmetry σ_{xz} and σ_{yz}. The transformations of the irreducible representations A_1, A_2, B_1, B_2 when a symmetry operation is applied are listed. Also, the elements of translation T_α along and rotation R_α about an axis $\alpha = (x, y, z)$ as well as the vibrational modes v_n are assigned to their corresponding irreducible representation. Table adapted from Ref. [Bun06]

It is possible to derive the selection rules purely from a consideration of the symmetry properties of the molecule which is why they are investigated more closely here. The point group of formaldehyde $\boldsymbol{C}_{2v}$ consists of the following symmetry operations: unity E, two-fold rotation about the z-axis C_2 and the two planes of symmetry σ_{xz} and σ_{yz}. The corresponding character table of its irreducible representations A_1, A_2, B_1, and B_2 is shown in Table 2.1. Also listed are the symmetries of the translations T_α along and rotations R_α about a molecule fixed axis and the symmetries of the vibrational modes of formaldehyde. These elementary symmetry properties of formaldehyde are crucial for the deduction of the selection rules in the following sections.

2.1.1 Vibronic excitation

In this section the selection rules for vibrational and electronic (vibronic) transitions in formaldehyde are discussed which can be determined from the symmetry of the involved wavefunctions. Only electric dipole transitions are considered within the approximations necessary for a fully separable wavefunction (see Equation (2.1)). This implies that the nuclear angular momentum quantum number I does not change (i.e. ΔI=0). Furthermore, no spin-orbit interaction is assumed resulting in the selection rule ΔS=0 for the spin S.

Electronic excitation The first electronically excited state of formaldehyde is the $\tilde{A}^1A_2$ state[3]. In this state the molecular structure is not planar anymore but rather pyramidal as shown in Fig. 2.1(b) [Mou75]. In the rigid rotor case this structure would correspond to the $\boldsymbol{C}_s$ point group but due to tunnelling the $\boldsymbol{G}_4$ molecular symmetry group needs to be used. It is isomorphic to $\boldsymbol{C}_{2v}$ which is why in literature it is commonly referred to the point group $\boldsymbol{C}_{2v}$ instead [Bun06].

To investigate the symmetry selection rules for a transition into this first electronically excited state the dipole transition matrix element for a transition from the initial state $|\Psi'\rangle$ to the final state $|\Psi''\rangle$ is considered

$$D_{f\leftarrow i} = \langle \Psi'_{\text{tot}} | \mu_A | \Psi''_{\text{tot}} \rangle \tag{2.2}$$

where μ_A is the dipole moment in the space fixed coordinate system $A = (X, Y, Z)$ which is connected with the dipole moment in the molecule fixed coordinate system $\alpha = (x, y, z)$ via the direction cosines λ_A^α [Bun06]:

$$\mu_A = \lambda_A^\alpha \mu_\alpha \tag{2.3}$$

Using this relation and the property that the wavefunction can be separated as shown in Equation (2.1), the transition matrix element can be rewritten by exploiting the fact that μ_α only involves vibronic coordinates, and that the λ_A^α only involve the Euler angles connecting the molecules fixed and the space fixed coordinate system [Bun06]:

$$D_{f\leftarrow i} = \langle \Psi'_{\text{elec}} \Psi'_{\text{vib}} | \mu_\alpha | \Psi''_{\text{elec}} \Psi''_{\text{vib}} \rangle \, \langle \Psi'_{\text{rot}} | \lambda_A^\alpha | \Psi''_{\text{rot}} \rangle \tag{2.4}$$

where the nuclear spin component is neglected. Considering only the electronic contribution in Equation (2.4) it can be seen that for the integral to be non-zero the product of the irreducible representation of the two involved electronic wavefunctions $\Gamma(\Psi'_{elec})$, $\Gamma(\Psi''_{elec})$ and the dipole operator $\Gamma(\mu_\alpha)$ has to contain the totally symmetric representation Γ_{sym}, i.e. A_1 for the point group $\boldsymbol{C}_{2v}$ [Her15]

$$\Gamma(\Psi'_{\text{elec}}) \otimes \Gamma(\mu_\alpha) \otimes \Gamma(\Psi''_{\text{elec}}) \supset \Gamma_{\text{sym}} = A_1. \tag{2.5}$$

Since the irreducible representations of the wavefunctions of the electronic ground state and the excited state are of symmetry type A_1 and A_2 respectively the dipole moment μ_A would have to be of type A_2. However, the dipole moment transforms in

[3] Disregarding the triplet state $\tilde{a}^3A_2$ only accessible via a weak spin-forbidden transition

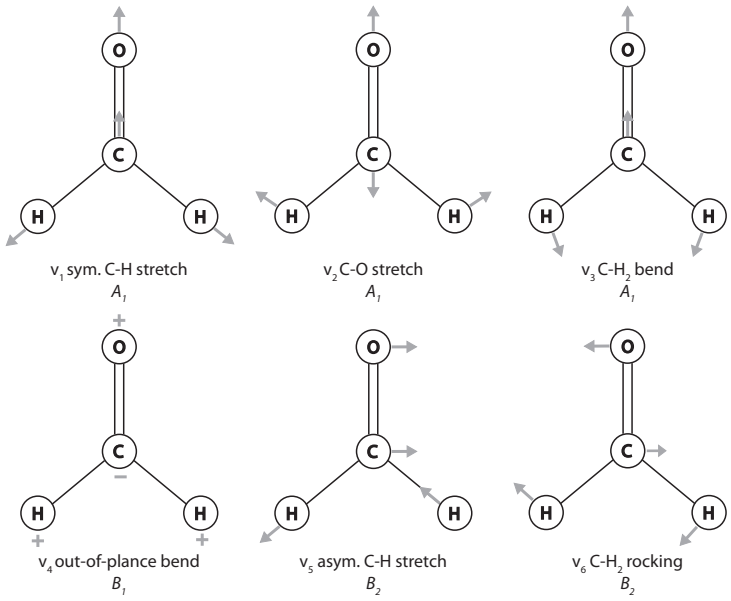

Figure 2.2: Vibrational modes of formaldehyde. The numbering follows the one given in Ref. [Bun06]. Below each mode its irreducible representation in the $\boldsymbol{C}_{2v}$ point group is given. Note that for the symmetry types B_1 and B_2 the definition depends on the choice of the molecule fixed coordinate system. Here, the notation recommended by Mulliken is employed [Mul55].

the same way as a translation vector which according to Table 2.1 cannot be of type A_2 [Bun06]. Therefore, this transition is electronically dipole forbidden. In order to explain the occurrence of this transition it is necessary to also take into account the vibrations of the molecule.

Vibrational excitation Formaldehyde has 6 vibrational modes which are summarised in Figure 2.2. The modes labelled v_1, v_2 and v_3 are totally symmetric (irreducible representation A_1) and give rise to a transition electric dipole moment along the principal axis a (see Figure 2.1). Mode v_4 causes a transition electric dipole moment along axis b and is of irreducible representation B_1 whereas the modes v_5 and v_6 give rise to a transition moment along the c axis and are of type B_2 [Mou75]. Depending on the orientation of the involved transition moment a transition is called a, b or *c-type* [Her66]. Of particular importance for this work is the mode v_1 which in the electronic ground state due to its fast spontaneous decay rate of about 60 Hz is well suited as cooling transition for optoelectrical Sisyphus cooling (see Section 2.2.1 and Ref. [Pre18]). Furthermore, the mode v_5 is used for optical pumping of the molecules into the ortho ground state $|J{=}\,1, K_a{=}\,1, K_b{=}\,0\rangle$ after Sisyphus cooling of the molecules in the state $|J{=}\,3, K_a{=}\,3, K_b{=}\,0\rangle$ (see Chapter 5).

For pure vibrational transitions the selection rules can be derived from similar symmetry considerations as for pure electronic transition by taking into account the corresponding transition electric dipole moment. Within a harmonic approximation of the molecular potential energy the selection rule is $\Delta v = \pm 1$. Only when taking into account the anharmonicity of the Morse potential higher vibrational transitions

can occur governed only by symmetry selection rules.

Following up on the discussion of the electronic transition $\tilde{A}^1A_2 \leftarrow \tilde{X}^1A_1$, in Equation (2.5) the symmetry of the vibrational wavefunctions involved has to be taken into account [Bun06]

$$\Gamma(\Psi'_{\text{elec}}) \otimes \Gamma(\Psi'_{\text{vib}}) \otimes \Gamma(\mu_\alpha) \otimes \Gamma(\Psi''_{\text{elec}}) \otimes \Gamma(\Psi''_{\text{vib}}) \supset \Gamma_{\text{sym}}. \tag{2.6}$$

With the help of Table 2.1 it is now easy to see that a transition between the vibronic ground state and excitations of the parallel vibrational modes v_1, v_2 and v_3 in the electronically excited $\tilde{A}^1A_2$ state stay electric dipole forbidden[4]. However, transitions between the ground state and excitations of the perpendicular modes v_4, v_5 and v_6 of the first electronically excited state are allowed with the $\tilde{A}^1A_2 \leftarrow \tilde{X}^1A_1$ 4_0^1 transition being considerably stronger than excitations of the vibrational modes v_5 and v_6. It is worth mentioning that the pyramidal structure of formaldehyde in the first electronically excited state causes a significant inversion splitting of the corresponding out-of-plane vibrational mode v_4 of about $125\,\text{cm}^{-1}$ [Her66]. An inversion splitting of this type is probably best known from the ammonia molecule NH_3. The intensity of such a vibronic transition is given by the Franck-Condon overlap $|\langle\Psi'_{vib}|\Psi''_{vib}\rangle|^2$, that is the overlap of the vibrational wavefunctions of the two involved states [Bun06].

2.1.2 Rotational states

In this section the rotational part of the wavefunction Ψ_{rot} is investigated. The asymmetric rotor Hamiltonian

$$H_{\text{rot}} = AJ_a^2 + BJ_b^2 + CJ_c^2 \tag{2.7}$$

not only couples states with ΔK=0, as it is the case for symmetric rotors, but also states with $\Delta K = \pm 2$. Here, K is the projection of the total angular momentum J onto the molecular symmetry axis. As a result the degeneracy of the parity eigenstates which form the solution of the Hamiltonian is lifted resulting in rotational K-type doublet states. In this case K is not a good quantum number anymore, nevertheless the K quantum numbers of the limiting cases of a prolate and oblate symmetric rotor K_a and K_c are used to describe asymmetric rotor states $|J, K_a, K_c, M\rangle$ [Kro75]. Asymmetric rotor states can be described by a linear combination of symmetric rotor states of different K but with equal J and M

$$|J, K_a, K_c, M\rangle = \sum_K a_K^{JK_aK_cM} |J, K, M\rangle\,. \tag{2.8}$$

Formaldehyde is only a slightly asymmetric rotor with its dipole moment along the a-axis which means that the main contribution to the expansion in Equation (2.8) are the terms with $|K| = K_a$. A detailed discussion of the solution of the asymmetric rotor Hamiltonian and the resulting energy level structure of the rotational states is given e.g. in Refs. [Som11, Ibr13, Pre18] or in most textbooks on molecular physics.

[4] Magnetically these transition are allowed and can be observed [Her66].

K_aK_c	Γ_{rot}
ee	A_1
eo	A_2
oo	B_1
oe	B_2

Table 2.2: Irreducible representation of different rotational wavefunctions in terms of the point group C_{2v}. e refers to an even K quantum number whereas o represents odd K. Table taken from Ref. [Bun06]

Rotational selection rules The selection rules for rotational transitions can again be derived by looking at the symmetries of the involved wavefunctions. In order to get a non-zero transition moment for a rotational transition the second term of Equation (2.4) has to be totally symmetric

$$\Gamma(\Psi'_{\mathrm{rot}}) \otimes \Gamma(\lambda_A^\alpha) \otimes \Gamma(\Psi''_{\mathrm{rot}}) \supset \Gamma_{\mathrm{sym}}. \tag{2.9}$$

The elements of the direction cosines λ_A^α transform in the same way as a rotation vector [Bun06]. Therefore, the irreducible representations of the elements of the rotations R_α are listed in Table 2.1. They determine the type of the transition, i.e. the directions of the transition dipole moment in the molecule fixed coordinate system. As mentioned before, the three different types of transitions are labelled a-, b- or c-type according to the direction of the transition dipole moment in the molecule frame. The irreducible representation of the rotational wavefunction of an asymmetric rotor can be determined by the symmetry species of the limiting cases of a prolate and oblate symmetric rotor because the asymmetry of the molecular structure does not affect the symmetry classification of the rotational states. This results in an irreducible representation of the rotational wavefunction Γ_{rot} depending on whether K_a and K_c are even e or odd o as summarised in Table 2.2. For a detailed derivation the reader is referred to Ref. [Bun06] or to the thesis of Erich Dobler where a summary for the case of formaldehyde is given [Dob16]. Combining the symmetries of the rotational wavefunction given in Table 2.2 with the symmetry of the direction cosine matrix in Table 2.1 it is easy to see that the selection rules depend on the transition dipole moment:

$$a\text{-type}: \quad \Delta K_a = 0, \pm 2, \ldots \quad \Delta K_c = \pm 1, \pm 3, \ldots \tag{2.10a}$$
$$b\text{-type}: \quad \Delta K_a = \pm 1, \pm 3, \ldots \quad \Delta K_c = \pm 1, \pm 3, \ldots \tag{2.10b}$$
$$c\text{-type}: \quad \Delta K_a = \pm 1, \pm 3, \ldots \quad \Delta K_c = 0, \pm 2, \ldots. \tag{2.10c}$$

Rotational transitions in the electronic ground state without vibrational excitation or including a parallel vibrational excitation are a-type transitions. This means that all transitions involved in the optoelectrical cooling scheme (see Section 2.2.1) obey the selection rules given in Equation (2.10a). The rotational selection rules for the vibronic transition $\tilde{A}^1A_2 \leftarrow \tilde{X}^1A_1\ 4_0^1$ on the other hand are given by Equation (2.10b) as the involved transition dipole moment is of type b. This is the transition employed for the detection of molecules discussed in Chapter 3 and Chapter 4. The selection

rules for J and M are given by ΔJ=0, ±1 and ΔM=0, ±1 just as for symmetric rotors [Tow75].

2.1.3 Hyperfine structure

In this section a short overview of the occurrence and magnitude of the nuclear hyperfine structure of formaldehyde is given. For this work hyperfine structure can mostly be neglected, but in Chapter 6 it does have to be considered as a possible limiting factor, also for future experiments. For the $H_2{}^{12}C^{16}O$ isotopologue neither the carbon nor the oxygen atom carry spin. Since there are no quadrupole moments, the hyperfine structure of this molecule is entirely caused by the two hydrogen atoms which are spin-$\frac{1}{2}$ particles. Due to the Pauli exclusion principle only wavefunctions fulfilling

$$\Gamma(\Psi_{\mathrm{rot}}) \otimes \Gamma(\Psi_{\mathrm{nspin}}) = B_1 \text{ or } B_2 \tag{2.11}$$

are allowed. This is equivalent to a wavefunction antisymmetric to an exchange of the spin-carrying H atoms. Of the $(2I_1 + 1)(2I_2 + 1)$=4 basic spin functions, with the spin of the two hydrogen atoms $I_{1/2}$, three are symmetric to an exchange of the H atoms and only one is antisymmetric [Kro75]. The exchange can be seen as a rotation of π about the principal axis a described by the $\boldsymbol{C}_2$ subgroup of $\boldsymbol{C}_{2v}$. The behaviour of the different irreducible representations of the point group $\boldsymbol{C}_{2v}$ upon a two-fold rotation C_2 is listed in Table 2.1. From Table 2.2 it can now be seen that for even K_a the rotational wavefunction is symmetric under C_2, meaning that in order to fulfil Equation (2.11) these states can only combine with antisymmetric hyperfine wavefunctions, whereas odd K_a rotational states, where the rotational wavefunction is antisymmetric under C_2, only combine with symmetric hyperfine wavefunctions. The result is that in order to fulfil the Pauli principle, for states with odd K_a there are three hyperfine substates whereas for even K_a there is only one state, i.e. no hyperfine structure. When the hyperfine structure is not resolved it manifests in a statistical weight for the population of the rotational state. States without hyperfine structure have a statistical weight of S=1 while the states that do exhibit hyperfine structure have a statistical weight of S=3. This partially explains the choice of $|J{=}3, K_a{=}3, K_c{=}0\rangle$ as cooling state for the cooling experiments with optoelectrical Sisyphus cooling, because due to the existence of hyperfine structure it has a higher statistical weight and the highest population of the initial molecule ensemble[5].

To investigate the size of the hyperfine splitting of formaldehyde the hyperfine Hamiltonian is considered [Shi67]

$$H_{\mathrm{hfs}} = H_{\mathrm{ss}} + H_{\mathrm{sr}}. \tag{2.12}$$

It has two contributions, firstly the direct spin-spin-interaction of the two protons H_{ss} and secondly the spin-rotation interaction H_{sr} which describes the motion of the charges in the rotating molecule creating a magnetic field which interacts with the spins [Tow75]. The spin-spin-interaction is given by

$$H_{\mathrm{ss}} = \boldsymbol{I}_{\mathrm{H}} \cdot \boldsymbol{D} \cdot \boldsymbol{I}_{\mathrm{H}} \tag{2.13}$$

[5] When taking into account the influence of the Stark shift of the molecules on the velocity filtering in the loading electric quadrupole guide. A detailed description is provided in Ref. [Pre18].

where $\boldsymbol{I}_\mathrm{H}$ are the angular momenta of the protons and $\boldsymbol{D}$ is the spin-spin coupling tensor. The elements of $\boldsymbol{D}$ are given by [Rea82]:

$$D_{ij} = g_\mathrm{H}^2 \mu_\mathrm{N}^2 \frac{(\boldsymbol{r}^2 \delta_{ij} - 3 r_i r_j)}{\boldsymbol{r}^5} \tag{2.14}$$

where g_H is the g-factor of the proton, μ_N is the nuclear magneton and $\boldsymbol{r}$ is the vector connecting the two interacting nuclei whose magnitude and orientation is determined in Ref. [Tak63].

The second term in Equation (2.12), the spin-rotation interaction, is given by [Shi67]

$$H_\mathrm{sr} = -C_J \boldsymbol{J} \cdot \boldsymbol{I} \tag{2.15}$$

with the spin-rotation parameter C_J. The molecular rotation is fast compared to the Larmor precession of the nucleus so that the time average of the angular momentum $\langle J_\alpha^2 \rangle$ has to be taken in order to calculate the magnetic field [Gor66]. This results in the following expression for C_J [Tha64]

$$C_J = \sum_{\alpha=x,y,z} M_{\alpha\alpha} \frac{\langle J_\alpha^2 \rangle}{J(J+1)} \tag{2.16}$$

with the spin-rotation tensor $M_{\alpha\alpha}$. This tensor has two contributions arising from the electrons and the nuclei in the molecule. Measured experimental data, however, typically already includes both contributions [Fab77]. In this thesis the calculation of hyperfine splittings for formaldehyde (see Chapter 6) is based on the numerical solution of Equation (2.12) with the free software PGOPHER [Wes17]. The magnitude of the hyperfine splitting of formaldehyde is on the order of a few kHz so that it can safely be ignored for most measurements in this thesis. It only becomes relevant in the course of the coherence measurements presented in Chapter 6.

2.1.4 Interaction with external fields

The interaction of formaldehyde with electric fields is of great importance for this work as they are the key element which enables trapping and guiding of the molecules. Additionally, they are also very important for the detection of the molecules as discussed in Chapter 4. The interaction with magnetic fields is also summarised as it is important for the measurements presented in Chapter 6.

Interaction with electric fields - Stark effect Here, only a brief overview of the interaction of formaldehyde with an external electric fields is given, because much more detailed treatments have already been given previously in theses performed in the Rempe group [Som11, Ibr13]. For formaldehyde in the vibronic ground state the dipole moment is pointing in the $z = a$ direction of the molecule fixed frame so that for an external electric field applied in the Z-direction of the space fixed coordinates the Stark Hamiltonian is

$$H_\mathrm{Stark} = E_Z \mu_z \lambda_Z^z, \tag{2.17}$$

with the direction cosine λ_Z^z connecting the molecule fixed coordinate system with the space fixed coordinate system similar to Equation (2.3). The Stark Hamiltonian

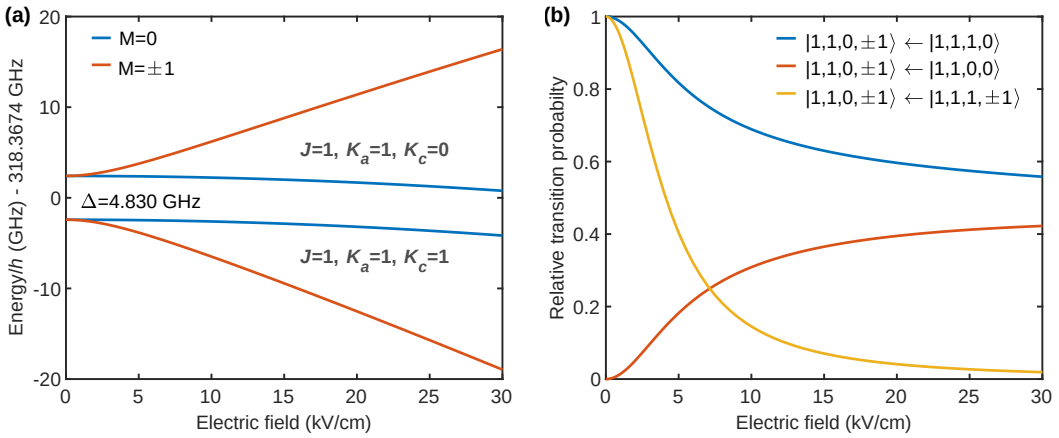

Figure 2.3: Properties of the J=1, K=1 rotational states of formaldehyde. **(a)** Stark shift of the rotational states $|J{=}1, K_a{=}1, K_c{=}0, 1, M\rangle$ of formaldehyde in the vibronic ground state. The energy splitting Δ introduced by the K-type doubling of the asymmetric rotor is shown. For small electric fields the states with $M{\neq}0$ experience a quadratic Stark shift, typical for asymmetric rotors, whereas for large electric fields the shift is essentially linear. Rotational constants for the vibronic ground state up to octic correction are taken from Ref. [Brü03]. **(b)** Relative transition probability for transitions between the $|J{=}1, K_a{=}1, K_c{=}0, M{=}1\rangle$ state and three other states of the J=1, K_a=1 manifold. Transition between sublevels with M=1 are allowed without electric field but suppressed in high electric fields according to symmetric rotor selection rules. The transitions to the M=0 states asymptotically approach a probability of $\frac{1}{2}$.

couples states with different J and leaves M as the only remaining good quantum number. In the field-free case states with different M quantum number are degenerate. By applying an external field this degeneracy is split up and only states with $\pm M$ remain degenerate. The eigenstates are typically expressed in an expansion of symmetric rotor states similar to Equation (2.8).

A numerical diagonalisation results in the Stark shift, i.e. the energy difference to the field-free case, and an exemplary result is shown in Figure 2.3(a) for the states $|J{=}1, K_a{=}1, K_c{=}0, 1\rangle$. Here, for zero electric field the K-type doubling mentioned in Section 2.1.2 can be observed. For higher electric fields the M-degeneracy is split up and the $M{=}\pm1$ states are shifted quadratically as is typical for an asymmetric rotor. The K-type doubled states get mixed so that for large enough electric fields essentially pure symmetric rotor states arise resulting in a linear Stark shift (see Ref. [Ibr13]). This behaviour can also be described in good approximation by a two-level model as is done in Ref. [Pre18]. In this thesis, all Stark shifts are calculated by the more precise but also computationally more expensive approach of a full numerical diagonalisation of the Hamiltonian.

Due to the mixing of the two parity states in the electric field the transition probabilities between rotational states are also altered. This can easily be seen when considering the decomposition of the asymmetric rotor states $|J, K_a, K_c, M\rangle$ in terms of symmetric rotor states $|J, K, M\rangle$ as given in Equation (2.8). The electric field dependent expansion coefficients $a_K^{JK_aK_cM}$ then allow to determine the transition probability between states. An example is given in Figure 2.3(b) where the

relative transition probabilities for a transition from the $|J{=}1, K_a{=}1, K_c{=}0, M{=}1\rangle$ state to three other states of the $J{=}1,\ K_a{=}1$ manifold in the vibronic ground state is shown. The probability for a transition to the state $|J{=}1, K_a{=}1, K_c{=}1, M{=}1\rangle$ starts out at one for zero electric field as is demanded by the selection rules given in Equation (2.10a). For higher electric fields this probability approaches zero as the states gradually turn into the symmetric rotor states $|J{=}1, \pm|K{=}1|, M{=}1\rangle$ and $|J{=}1, \pm|K{=}1|, M{=}{-}1\rangle$ where this transition is forbidden. The two transitions into the $M{=}0$ sublevels approach a probability of $\frac{1}{2}$ because both states are unaffected by the electric fields up to high values where the mixing with different J states starts to play a role. Therefore, only the composition of the state of origin changes and is responsible for the change in transition probability. The transition considered here is of particular importance in Chapter 6.

Interaction with magnetic fields - Zeeman effect For polyatomic closed shell molecules the interaction with magnetic fields is in general quite weak compared to the Stark effect. For moderate magnetic field strengths on the order of 1 G it is of the same order of magnitude as the hyperfine interaction which is why the Zeeman effect, unlike the Stark effect, is treated including hyperfine structure in this work. The Hamiltonian describing the interaction is

$$H_{\text{Zeeman}} = -\boldsymbol{\mu}_{\text{m}} \cdot \boldsymbol{H} \tag{2.18}$$

with the magnetic moment $\boldsymbol{\mu}_{\text{m}}$ and magnetic field strength $\boldsymbol{H}$. Its solution is described in great detail in Ref. [Gor70] for various types of molecules and here only a few results relevant for formaldehyde are summarised. There are three effects contributing to the Zeeman interaction. The first is the magnetic moment arising from the rotation of the molecules interacting with the magnetic field. The second effect are the nuclear spins directly interacting with the magnetic field. The last component arises from the magnetic susceptibility which gives rise to a small magnetic moment when an external magnetic field is applied. This second order contribution is very small, and therefore ignored in this work.

First, the interaction of the magnetic moment caused by rotation is treated. In this case the Zeeman energy shift for a magnetic field H_z in z-direction is given by [Bur53, Fly65]

$$E_{\text{Zeeman}} = -\mu_{\text{N}} g_J M_J H_z \quad \text{with} \quad g_J = \frac{1}{J(J+1)} \sum_{\alpha=x,y,z} g_{\alpha\alpha} \langle J_\alpha^2 \rangle, \tag{2.19}$$

where μ_N is the nuclear magneton[6]. The $g_{\alpha\alpha}$ are diagonal elements of the molecular g-value tensor in the principal axis coordinate system and $\langle J_\alpha^2 \rangle$ is the time averaged square of the angular momentum just as in Equation (2.16), again resulting from the fact that precession around $\boldsymbol{H}$ is much slower than the rotation of the molecule. The g-value tensor consists of a nuclear contribution corresponding to a rigid system of rotating charges, and a more complex electronic contribution arising

[6] The molecular Zeeman effect is typically so small that it is expressed in terms of the nuclear magneton μ_{N} instead of the Bohr magneton μ_{B} as is customary for atoms. This results in molecular g-values on the order of 1.

from the electrons precessing more or less freely in the molecule. Both contributions almost cancel and leave a very small net value for the g-factor [Esh52, Bur53]. Experimental values for formaldehyde have been measured precisely and include both contributions [Hüt68].

For the direct interaction of the nuclear spins of the molecule with the magnetic field two cases have to be distinguished. In the weak-field case the Zeeman interaction is much smaller than the hyperfine structure, resulting in coupling of the rotational angular momentum $\boldsymbol{J}$ with the angular momentum of the nuclei $\boldsymbol{I}$ to a total angular momentum $\boldsymbol{F}$, which precesses about the direction of the magnetic field. This gives rise to a Zeeman energy shift of

$$E_{\text{Zeeman}} = -\mu_{\text{N}} g_F M_F H_z \quad \text{with} \quad g_F = \alpha_J g_J + \alpha_I g_I. \tag{2.20}$$

The prefactors α_J and α_I are given by the coupling of the two vectors $\boldsymbol{J}$ and $\boldsymbol{I}$ as

$$\alpha_J = \frac{F(F+1) + J(J+1) - I(I+1)}{2F(F+1)} \quad \text{and} \tag{2.21a}$$

$$\alpha_I = \frac{F(F+1) + I(I+1) - J(J+1)}{2F(F+1)}. \tag{2.21b}$$

The factor g_I again consists of two contributions arising from the coupling of the two hydrogen angular momenta I_1 and I_2. For the determination of g_I similar prefactors have to be constructed from the addition of the two vectors.

In the strong-field case the magnetic field is so strong, that the coupling between $\boldsymbol{J}$ and $\boldsymbol{I}$ is broken down and both precess separately around $\boldsymbol{H}$. The Zeeman energy in this case is much larger than the hyperfine splitting. In this so-called Paschen-Back regime, which for formaldehyde sets in at magnetic fields strengths of about several tens of Gauss, the Zeeman shift is in principle given by Equation (2.19), just like for molecules without nuclear coupling, however, the hyperfine splitting is changed. The nuclear coupling energy in this case is simply given by

$$E_{\text{nuc}} = -C_J M_J M_I \tag{2.22}$$

with the spin-rotation tensor C_J as defined in Equation (2.16). For formaldehyde there are no nuclear electric quadrupole interactions which means that nuclear coupling is quite small (refer to Section 2.1.3) and the Zeeman energy already exceeds the hyperfine energy for magnetic fields of only a few Gauss. Typical values for the Zeeman shift of formaldehyde are on the order of $1\ \frac{\text{kHz}}{\text{G}}$ meaning that for magnetic and electric fields achievable in a laboratory the Zeeman shift is much weaker than the Stark shift which is rather on the order of $1\ \frac{\text{MHz}}{\text{V/cm}}$.

Combined Zeeman-Stark effect including hyperfine interaction When electric and magnetic fields are applied at the same time the treatment is considerably more difficult. For arbitrary orientations of both fields, M is not a good quantum number anymore resulting in rather complex expressions. This combined Stark-Zeeman effect is investigated in Ref. [Kon60]. A detailed discussion is beyond the scope of this thesis but the special case of parallel electric and magnetic field can be

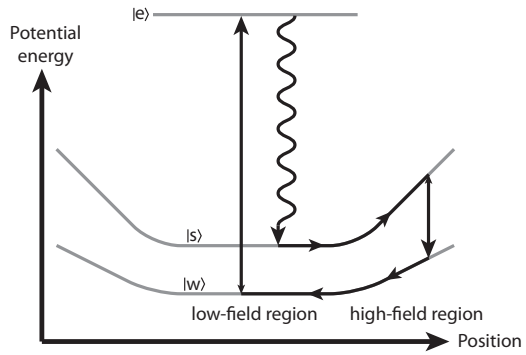

Figure 2.4: Sketch of the optoelectrical Sisyphus cooling cycle. Molecules in the strongly trapped state |s⟩ move into the high-field region where they are transferred to the more weakly trapped state |w⟩. Due to the weaker interaction they loose kinetic energy. From the state |w⟩ the molecules are pumped to an excited state |e⟩ from where they can spontaneously decay back to the initial state |s⟩ which causes the process to be unidirectional.

treated rather easily as the energy shifts are simply additive [Tow75]. Therefore, the result from numerically solving the Stark-Hamiltonian in Equation (2.17) is simply added to the Zeeman shift. When the hyperfine structure needs to be considered in this thesis the free software PGOPHER is used to calculate the Zeeman-Stark effect [Wes17]. This software package also assumes that magnetic and electric field are oriented in parallel which is a valid approximation for the experiments presented in this thesis (see Chapter 6).

2.2 Experimental foundation

In this section a short introduction to the experimental foundations which were already preexisting at the start of this thesis is given. To this end the optoelectrical cooling scheme is introduced in Section 2.2.1 which is the scheme used in the experiment to cool polar molecules down to the millikelvin regime. Furthermore the status of the experimental setup before the work of this thesis began is presented in Section 2.2.2.

2.2.1 Optoelectrical Sisyphus cooling

Optoelectrical Sisyphus cooling was first proposed in Ref. [Zep09]. The basic idea relies on a position dependent electric field trapping the molecules with high electric fields in the border region and low electric fields in the central region with a strongly trapped state |s⟩ and a more weakly trapped state |w⟩ as illustrated in Figure 2.4. When molecules in the state |s⟩ enter the high-field region they are slowed down and their kinetic energy is converted into potential energy. In the high-field region a transition into the state |w⟩ is driven resulting in a loss of energy upon the molecules' return to the weak field centre region due to the weaker interaction, i.e. lesser slope, in this state. In order to make the process unidirectional the molecules are subsequently strongly driven into an excited state |e⟩ from where they can spontaneously

decay back into the initial state $|s\rangle$, thus closing the cycle.

For formaldehyde the states $|w\rangle$ and $|s\rangle$ are represented by the rotational M-sublevels of the J=3, K_a=3 state in the vibronic ground state. Due to the strong interaction of the permanent dipole moment of formaldehyde, i.e. the large Stark shift, a large amount of energy can be removed in a single step [Pre16]. This has the advantage that only a few dozen cooling steps are needed to cool the molecules by several orders of magnitude. Therefore, the cooling scheme is not as susceptible to loss channels as e.g. laser cooling. The excited state $|e\rangle$ is realised by the rotational J=3, K_a=3 state of the first excitation of the v_1 vibrational mode which offers favourable selection rules due to its symmetry combined with a relatively fast spontaneous decay rate of about 60 Hz which sets the time scale for the cooling process. Molecules decaying into J=4, K_a=3 can easily be incorporated into the cooling scheme by adding radiation sources in the millimetre wavelength regime as repumpers.

Optoelectrical Sisyphus cooling has first been demonstrated for the symmetric rotor fluoromethane [Pre12, Zep12, Zep13, Eng13] which was cooled down to a temperature of 29 mK. A result mainly limited by the detection, as is addressed in more detail in Chapter 3, but also by a slow vibrational decay rate and technical problems with the microwave source. After significant improvements to the experiment the cooling scheme was implemented for formaldehyde where a temperature of 420 µK was achieved for a record number of approximately $3 \cdot 10^5$ molecules [Pre16, Pre18]. The limitation for this result was also of technical nature caused mainly by the electric trap for the molecules [Pre16] that is introduced in the next section.

2.2.2 Pre-existing setup

In this section the experimental setup existing before the work of this thesis started is presented. The main change to this setup performed during this thesis is the implementation of a new detection scheme and setup which is discussed in Chapter 3.

Source and guiding of the molecules Gaseous formaldehyde molecules are created by heating up paraformaldehyde in which the formaldehyde molecules are bound in a complex with water. The water vapour is subsequently frozen out in a vacuum trap at dry ice temperatures leaving a pure gas of formaldehyde. This process is explained in more detail in Refs. [Ibr13, Pre18]. The molecules are then inserted into the vacuum chamber via a heated liquid nitrogen cooled nozzle at 150 K [Mie10]. From there the molecules are guided by an electric quadrupole guide [Ran03, Jun04] to the electric trap as shown in the schematic overview in Figure 2.5. The finite potential created by the quadrupole guides leads to velocity filtering of the molecules so that they reach the electric trap with a translational temperature of $\lesssim$ 1 K depending on the applied voltages. Details about electric guiding are provided in Refs. [Mot09, Eng13].

Electric trap The electric trap is the central part of the experiment and creates the box-like potential needed for optoelectrical Sisyphus cooling. It was designed by Martin Zeppenfeld [Zep13] and it is where cooling and trapping take place as well

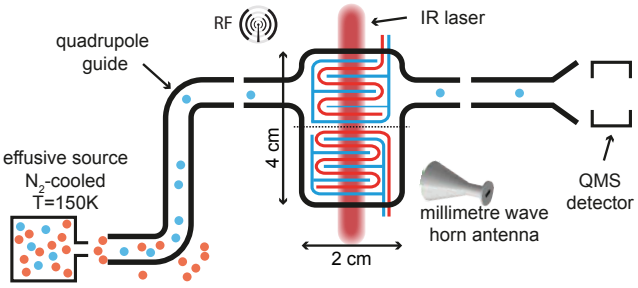

Figure 2.5: Overview of the experimental setup. Formaldehyde molecules are produced in a thermal source at 150 K and guided via a quadrupole guide to the electric trap. Here the molecules are stored and can be manipulated by radiofrequency (RF), millimetre waves or an infrared (IR) laser. For detection the molecules are unloaded via another quadrupole guide and detected by a quadrupole mass spectrometer (QMS).

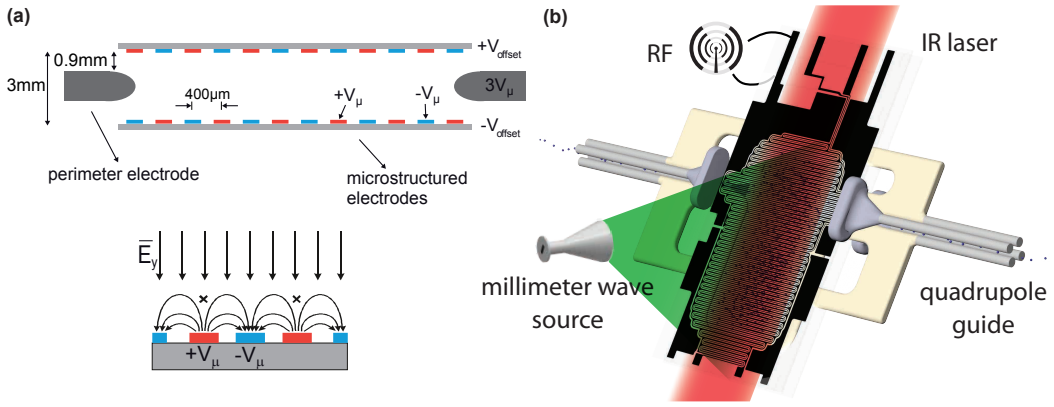

Figure 2.6: Basic design of the electric trap and integration into the experiment. **(a)** The trap consists of two capacitor plates, shown here in a vertical schematic cut, which create a homogeneous tunable offset field by applying the voltage $\pm V_{\text{offset}}$. A microstructuring on each plate allows the application of spatially alternating high voltages $\pm V_\mu$ creating high electric fields close to each plate. **(b)** Integration of the trap into the experimental environment with the connecting quadrupole guide and various radiation sources.

as all other experiments performed to date [Eng13, Glö16, Pre18]. The fundamental design of the trap is shown in Figure 2.6(a). It consists of two plate capacitors that create a homogeneous tunable offset field providing the low-field region shown in Figure 2.4. Each plate is microstructured and by applying spatially alternating high-voltages to the microstructure electrodes a high electric field is created at the edge of the trap as illustrated in Figure 2.6(a). Thereby molecules in low-field seeking rotational states are confined and at the same time the potential hill necessary for Sisyphus cooling is provided. The field decays exponentially towards the centre of the trap and so only minimally distorts the homogeneity of the field in the centre. To close the trap in the remaining two dimensions a perimeter electrode which is directly connected to the electric guides is added as indicated in Figure 2.6. The distribution of electric fields within the trap is shown in Figure 6.7. It has a sharp peak representing the homogeneous electric field in the centre and quickly trails of

towards lower and higher fields. The distribution is very asymmetric with a long tail caused by the high confining electric fields. The achieved $1/e$ trap lifetime ranges from 10 s for uncooled molecules [Eng11] up to 60 s when cooling is applied [Pre16].

Radiation sources For the manipulation of the internal states of the molecules various radiation sources are available. Firstly, there is an infrared (IR) laser for vibrational excitation of the molecules. This laser is frequency stabilised to an optical frequency comb and can be scanned on a ms-timescale over a frequency range of over 60 GHz [Pre17]. Since the ramping time is on the same order of magnitude as the excited state lifetime of the v_1 excitation the system allows a quasi-continuous driving of multiple transitions with sub-MHz precision. Secondly, radiofrequency (RF) is coupled into the vacuum chamber and applied directly to the capacitor plates of the electric trap. Due to the lack of any explicit impedance matching the coupling is much more efficient for frequencies in the few hundred MHz range than for higher frequencies in the GHz regime [Eng13]. The RF is mainly used to drive transitions between M-sublevels of a single rotational state split up by the electric field of the trap. Finally, there is also millimetre wave radiation available. It is created by amplifier multiplier chains fed by a microwave (MW) synthesizer providing frequencies on the order of 10 GHz. Again, fast switching between different frequencies allows for quasi-continuous driving of different transitions simultaneously. In this work the radiation is mainly used as repumper between states with J=3, K=3 and J=4, K=3 for the optoelectrical cooling cycle.

Detection The molecules were unloaded from the trap via another quadrupole guide and brought to a quadrupole mass spectrometer for detection (QMS). Details about this detection can be found in Ref. [Pre18]. The replacement of the QMS by an improved detection method is one of the major topics of this thesis.

3 LIF detection of formaldehyde: Concept and experimental implementation

Efficient detection of molecules is a formidable task. The standard detection technique for atoms, which is based on driving a cycling transition and either collecting the emitted fluorescence photons or measuring the absorption, cannot in general be transferred to molecules. Only for a few select diatomic species such optical cycling transitions are available. Upon electronic excitation many polyatomic molecules predissociate and even when the excited state is stable, a lack of strict selection rules for vibrational transitions results in a multitude of vibrational states being populated after spontaneous decay. Therefore, an impractically huge number of repumpers would be required to achieve a closed transition cycle. An alternative technique is resonance-enhanced multiphoton ionisation (REMPI). However, due to the large ionisation threshold of $> 10\,\mathrm{eV}$ of formaldehyde the multiphoton excitation involved requires either high laser powers or laser wavelengths in the deep UV or in some cases both [Par16]. For these reasons, in the past a quadrupole mass spectrometer (QMS) was employed at the experiment for optoelectrical Sisyphus cooling which is an obvious and convenient choice. They are commercially available, allow robust long term operation with close to no maintenance and are not limited to a particular molecule species [Pre18]. These benefits come at the cost of a low detection efficiency of only about 10^{-4} and a lack of state selectivity. Furthermore, the electric fields present in a QMS, necessary for the ionisation of the molecules and the extraction of ions, lead to problems when working with ultracold molecules. The molecules relevant to optoelectrical Sisyphus cooling have a permanent electric dipole moment whose strong interaction with electric fields prevents the direct detection of very slow low-field-seeking molecules [Pre18].

Due to the disadvantages of a QMS, the concept as well as the technical implementation of an optical detection scheme via laser-induced fluorescence (LIF) is presented in this chapter. The basic idea and the work done prior to this thesis is discussed in Section 3.1. The design of the light collection optics as well as a first setup is presented in Section 3.2. Achieving low background light levels is critical to observe the small number of photons emitted by the molecules. This turned out to be a much bigger challenge than previously anticipated and the mitigation of the influence of stray light is presented in Section 3.3. Finally, the setup which allows detection of formaldehyde via LIF with a greatly improved background level is summarised in Section 3.4.

3.1 Detection via the $\tilde{A}^1A_2 \leftarrow \tilde{X}^1A_1\ 4_0^1$ transition

The basic principle of an all optical detection method for formaldehyde relies on exciting the molecules electronically and detecting the subsequent fluorescence photons emitted upon spontaneous decay. This process of excitation using laser radiation followed by a decay via spontaneous emission of a fluorescence photon is referred to as laser-induced fluorescence (LIF). A key property for an optical detection method is the quantum yield, defined as the fraction of excited molecules decaying under the emission of a radiation quantum. As mentioned above polyatomic molecules such as formaldehyde typically have no cycling transition available due to the decay of the excited state into a multitude of states in the ground state. Furthermore, the molecules often predissociate upon electronic excitation, resulting in a quantum yield significantly smaller than one. Therefore, the quantum yield is directly proportional to the amount of photons that can be extracted from each individual molecule and hence defines the detection efficiency that can be achieved. The main goal of the detection scheme is to detect formaldehyde molecules after optoelectrical Sisyphus cooling, where they end up in the rotational $|\tilde{X}; J{=}3, K_a{=}3, K_c{=}0\rangle$ state of the electronic ground state [Pre16]. Suitable for the detection of formaldehyde is the transition $\tilde{A}^1A_2 \leftarrow \tilde{X}^1A_1\ 4_0^1$ which has favourable decay properties with a high quantum yield and its radiative decay has already been used for the detection of formaldehyde [Möh85, Hud06]. In particular, for the transition $|\tilde{A}; J{=}2, K_a{=}2, K_c{=}1\rangle \leftarrow |\tilde{X}; J{=}3, K_a{=}3, K_c{=}0\rangle$ a value of 32.2 % is given for the quantum yield in the literature [Shi81], which can be used to detect molecules after cooling. For lower J quantum numbers even longer radiative decay times have been measured corresponding to an even better quantum yield [Hen82]. A further benefit of the $\tilde{A}^1A_2 \leftarrow \tilde{X}^1A_1\ 4_0^1$ transition is that the fluorescence spectrum ranges from about 380 nm to 550 nm [Bou96] (see Figure 4.14) and thus is spectroscopically separated from the excitation wavelength which lies in the near UV at 354 nm [Clo83]. An all optical detection of formaldehyde based on LIF on the aforementioned transition should therefore be feasible.

In the master thesis Erich Dobler made in the Rempe group the possibility of a LIF based detection was investigated in a room temperature setup with a pulsed dye laser [Dob16]. A rotational state resolving spectrum was measured and the individual lines could be identified. Furthermore, the quantum yield as a key property of the excitation for the detection was investigated. The quantum yield can be determined by

$$\Phi = \frac{n_{\mathrm{fl}}}{n_{\mathrm{abs}}} = \frac{\tau_{\mathrm{fl}}}{\tau_{\mathrm{rad}}} \tag{3.1}$$

with the number of fluorescence photons n_{fl}, the number of absorbed photons n_{abs}, the fluorescence lifetime τ_{fl} and the radiative lifetime τ_{rad}.

To understand the connection of lifetimes to the quantum yield, the involved decay rates can be considered. The quantum yield is of course given by $\Phi = \frac{\Gamma_{\mathrm{rad}}}{\Gamma}$ with the radiative decay rate Γ_{rad} and the total decay rate $\Gamma = \Gamma_{\mathrm{rad}} + \Gamma_{\mathrm{nrad}}$ which also contains the decay rate of non-radiative transitions Γ_{nrad}. The observable lifetime of the fluorescence is given by $\tau_{\mathrm{fl}} = \frac{1}{\Gamma}$ and the pure radiative lifetime is $\tau_{\mathrm{rad}} = \frac{1}{\Gamma_{\mathrm{rad}}}$. This means that τ_{rad} is not directly accessible in a measurement and the second

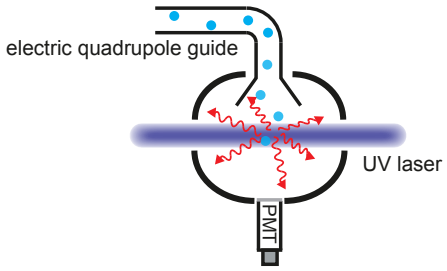

Figure 3.1: Sketch of the LIF detection setup. Molecules leave the electric trap (not shown) via an electric quadrupole guide. The guide bends down and the molecules enter the detection area where they are excited by a UV laser. The fluorescence light is then imaged onto a photomultiplier tube (PMT) for detection.

part of Equation (3.1) cannot be used directly for a determination of the quantum yield. Due to state changing collisions the measurements have to be performed at low pressures [Mil78, Fai81] also making n_{abs} too small to be measured easily. The solution to this dilemma was measuring a pressure quenched value for Φ at high pressures via the photon numbers which in combination with the pressure shortened fluorescence lifetime τ_{fl} allows to determine τ_{rad}[1]. By performing fluorescence lifetime measurements at low pressures the absolute value of Φ can then be determined. This procedure gave a result of 11.9 % for the quantum yield of the detection transition but is potentially accompanied by significant systematic errors due to the indirect measurement procedure. The values given in the literature are suffering from the same problem of collisional relaxation and the values had to be extrapolated to zero pressure [Shi81, Fai81]. A measurement without these shortcomings is presented later on in this thesis (see Section 4.3).

Another important requirement for an efficient detection scheme is the amount of laser power necessary to saturate the transition as it has to be ensured that the majority of the molecules get excited and contribute to the fluorescence signal. It is targeted to operate the detection in a continuous wave fashion in order to avoid loosing fluorescence signal during the unloading of the molecules from the trap which happens on a time scale of several seconds. Therefore, in the thesis of Erich Dobler also an estimate for the laser power necessary to saturate the transition was worked out by determining the Einstein B coefficient. For ultracold molecules with a velocity of 0.5 $\frac{\mathrm{m}}{\mathrm{s}}$ the result was 40 mW, a value easily achievable with a laser setup as presented in the next section.

3.2 LIF detection setup and mirror design

In this section an overview over the 'initial' setup is given, where 'initial' refers to the fact that experimental extensions necessary to control immense stray light background levels are not yet included in the description (see Section 3.3). As mentioned previously, predissociation of the molecules and the bad Franck-Condon overlap which is responsible for the lack of a cycling transition result in less than

[1] This treatment assumes that there is no pressure dependence of the radiative lifetime τ_{rad} [Dob16].

one fluorescence photon emitted per excited molecule. For an efficient detection it is therefore indispensable to cover a large solid angle and have minimal losses to collect as many of the emitted photons as possible. This constraint already excludes excitation of the molecules within the electric guide because a large solid angle would be blocked by the rods of the electric guide, besides the problem of Stark broadening this would would bring along. Consequently, the molecules have to leave the guide to allow detection in free space. To release the molecules the ends of the guide are bent outwards for a focussing effect [Mie10] and covered by an end cap for shielding from the high electric fields at the quadrupole guide. Nonetheless, after leaving the guide the molecule beam still spreads out to some degree so that in order to minimize the necessary laser power, detection close to the exit of the guide is preferential. To allow for the detection of very slow molecules without gravity changing the direction of the beam the guide is bent downwards releasing the molecules along the direction of gravity. The UV laser is sent perpendicular to the molecule beam through the detection area. Now, to achieve a solid angle as large as possible, the fluorescence light is collected by an 'integrating sphere' [Jac55] type light collection optics within the vacuum chamber. The only openings are for the electric guide to enter, for the excitation laser beam to enter and leave the detection region and for the collected light to leave the sphere for detection. This light collection optics is referred to as *LIF mirror* in this thesis. Detection of the light happens outside of the vacuum chamber to maintain flexibility in terms of the detection device and possible spectral filters employed for separating the excitation wavelength from the fluorescence spectrum. In Figure 3.1 an overview of the setup is sketched.

LIF mirror design For the in-vacuum LIF mirror collecting the fluorescence light and imaging it onto a detection unit the following approach is chosen: The first half of the LIF mirror is spherical with a radius of R=47 mm and reflects the light originating from the centre of the sphere back into its origin. The second half of the LIF mirror is a prolate spheroid with a semi-major axis of c=67.65 mm and two semi-minor axes of a=56.43 mm which focuses the fluorescence light originating in the centre of the detection volume onto a photomultiplier (PMT) in the focal plane. This uses the well-known property that an ellipse focusses rays originating from one of its focal points onto its second focal point. A sketch of the imaging principle is shown in Figure 3.2 where the area of origin of the fluorescence light is indicated by a dashed circle. Also included in Figure 3.2 is the result of an optical ray tracing simulation which is discussed later in this section. The centre point of the half sphere coincides with one of the focal points of the spheroid. The semi-major axis of the spheroid is aligned with the connection of the centre point of the half sphere with its top point. This geometry results in light originating in the centre being focused through a hole in the middle of the half sphere onto the second focal point of the spheroid which is located outside of the mirror and of the vacuum chamber. Due to the above mentioned spread of the molecule beam after leaving the guide the fluorescence light is not originating from a point source but rather a volume of finite size. Therefore, the light is not focussed on a point but a larger area influencing the choice of the detector. A main constraint for the LIF mirror is that it has to be ultra-high vacuum (UHV) compatible. To comply with this requisite and allow to build

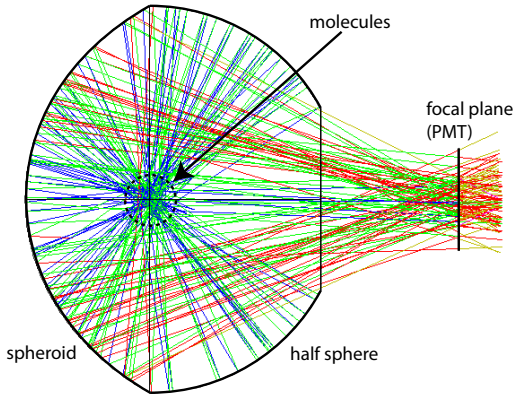

Figure 3.2: Imaging principle of the LIF mirror. Light originating in the centre is retro-reflected into the origin by a half sphere. A spheroid focuses the light onto a focal plane outside of the detection volume where a PMT for detection is placed. Also included is a simulation of beam paths performed with Zemax. 10^3 rays originate in the centre of the detection region in a volume of size 0.2 mm × 2.2 mm × 2.2 mm and are propagated through the system. Here, 0.2 mm accounts for the approximate vertical focus of the laser beam in the centre of the mirror where the molecules are excited. 2.2 mm corresponds to the transversal spread of the molecule beam after leaving the guide (see Section 4.5.1 for details). The rays are coloured according to the number of reflections, *blue* rays originate in the centre, *green* rays have been reflected once and *red* rays have been reflected twice.

arbitrary shapes the base material chosen for the mirrors is oxygen-free copper. The mirrors were then manufactured by the company Kugler by single point diamond turning achieving a roughness of $R_a < 4\,\mathrm{nm}$[2]. A technical three-dimensional drawing of the two LIF mirror halves is shown in Figure 3.3.

To achieve a high reflectivity over the spectral range of the fluorescence light the mirrors are coated with aluminium. Due to technical issues during the manufacturing process the coating in the very steep, outer part of the spherical mirror is very thin, and therefore of bad quality not providing the targeted high reflectivity in this area. In Figure 3.4 a photograph of the spherical part of the LIF mirror is shown and at the upper edges the coating imperfections can be seen. A more detailed discussion of the reflectivity of the surface of the LIF mirror is given in Section 4.5.2 with the discussion of the detection efficiency.

The electric quadrupole guide leads into the LIF mirror volume and releases the molecules 10 mm above the centre point. At the exit of the guide the rods bend outwards in order to minimize the beam spread of the molecule beam [Mie10]. The guide end is covered by a guide cap which can be grounded or set to an arbitrary potential to isolate the detection volume from the high electric fields in the quadrupole guide. Due to the spread of the guide this cap has a diameter of 20 mm covering a substantial solid angle. For this reason, the distance of the excitation volume to the guide is a compromise because for closer distances a larger solid angle is blocked whereas for larger distances the beam spread is larger requiring higher laser powers

[2]The value R_a is the arithmetical mean deviation of a surface commonly used to describe surface roughness.

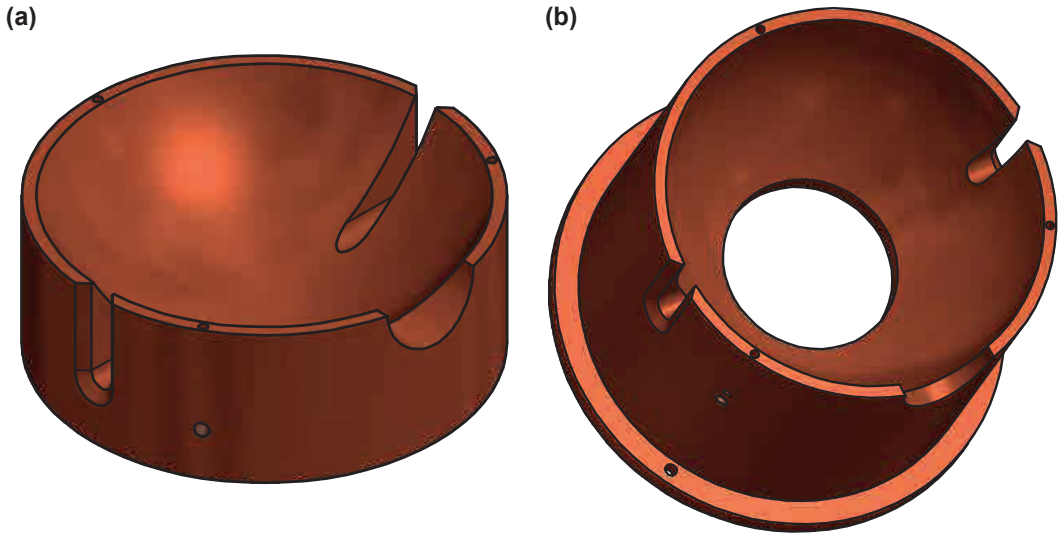

Figure 3.3: Technical drawings of the mirror collecting the fluorescence light for detection of formaldehyde molecules. (a) Elliptical part of the mirror. On both sides an elongated hole can be seen for the UV laser to enter and leave the detection volume. The hole on the lower right of the figure accommodates the guide and the end cap for shielding from the high electric fields at the electric quadrupole guide. **(b)** Spherical part of the mirror. The elongated entrance and exit hole can again be observed just like the space for the electric guide. The big hole in the centre is where the collected light leaves the mirror and is imaged onto a photomultiplier tube.

due to the larger surface to be illuminated. The UV laser enters via an elongated hole of size 6 mm × 50 mm and leaves on the opposite side via another hole of the same size to avoid having to dump the beam close to the detection volume. The holes are asymmetric to be able to accommodate an elliptical beam so that the complete width of the spread-out molecule beam can be illuminated. In the centre of the spherical part of the mirror there is another hole where the collected photons leave the LIF mirror volume. Directly afterwards a re-entrant vacuum window is placed which accommodates the single photon counting unit for detection of the photons at the second focal point of the spheroid. In Figure 3.4 half of the laser entry and exit holes are visible. Furthermore, half of the entry hole of the electric quadrupole guide and the exit hole for the focused fluorescence light can be made out.

The coloured rays in Figure 3.2 are an optical depiction of a ray tracing simulation in Zemax of the LIF mirror. 10^6 rays are simulated and originate in the centre of the LIF mirror in a spheroidal volume given by the size of the excitation laser and the molecule beam. The ray origination density is given by a Gaussian with $1/e^2$ size of 0.2 mm × 2.2 mm × 2.2 mm. The smallest dimension of 0.2 mm corresponds to the focus of the laser in vertical direction (see Section 3.3.3) while 2.2 mm is determined by the size of the molecule beam as measured in Section 4.5.1. In the figure only 10^3 rays are shown for better visibility. The rays are imaged by the elliptical part of the mirror through the hole in the centre of the spherical part onto a detection surface of size 25 mm. The rays are colour coded according to segments. Rays originating in the centre are of blue colour, rays that have been reflected once are red and rays

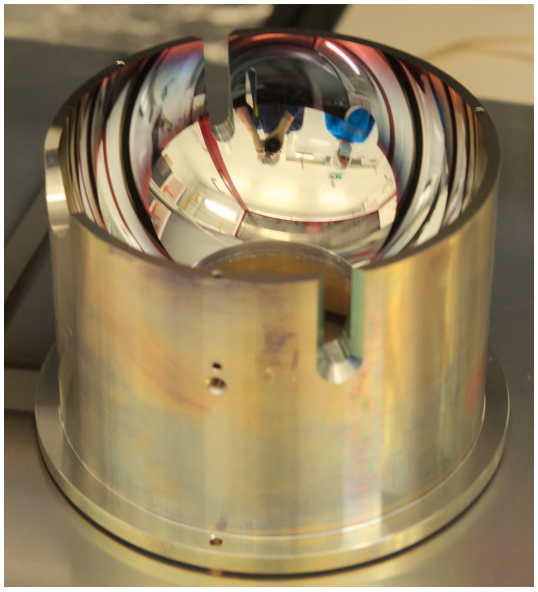

Figure 3.4: Spherical part of the LIF mirror. In the centre the hole where the light leaves for the detector is visible. On both sides half of the elongated hole for the laser can be seen and on the left, half of the hole where the guide enters the detection volume is shown. At the upper edge the imperfect coating can be recognised.

that have been reflected twice are green. This simulation results in an effective solid angle coverage, i.e. the solid angle covered for the excitation volume and not for a point source, of 79.3 %. The biggest loss is due to the close proximity of the guide cap to the excitation volume accounting for a loss in effective solid angle of 15.1 %. The influence of the apertures for the laser beam and of the finite detector surface are much smaller with 2.0 % and 2.7 % respectively.

PMT for detection of photons As detection unit for the fluorescence photons the photomultiplier tube (PMT) R6094P from Hamamatsu is used. It has a large circular active area of 25 mm diameter and a low dark count rate of about 25 $\frac{\text{cnts}}{\text{s}}$. The quantum yield, i.e. the detection efficiency for a single photon, peaks with 25 % at 400 nm, and therefore coincides with the maximum of the fluorescence spectrum. A detailed curve of the quantum yield of the PMT is shown in Section 4.5.2 with the determination of the detection efficiency of the LIF detection setup. For solid state systems much higher quantum yields can be achieved but at the cost of a much higher dark count rate per surface area. Therefore, due to the particular constraints of this experiment using such a detector is not beneficial. The PMT is placed outside of the vacuum chamber in a re-entrant window at the focal plane of the LIF mirror. In front of the mirror filters for the separation of the stray light at the excitation wavelength from the desired fluorescence light can be placed. The re-entrant window has an anti-reflective coating for the fluorescence light. A measurement of the transmission is shown in Section 4.5.2.

UV-laser The excitation frequency of 354 nm is generated by a UV laser combined from several commercial products. First, a seed laser consisting of an extended-cavity diode laser from the company LEOS provides light at a wavelength of 1062 nm with 50 mW of power. This output is then amplified by a fibre amplifier provided by Azur Light Systems with an output power of up to 20 W. The output is fed into a frequency tripler, again manufactured by LEOS. It consists of two elements: First, half of the input light is frequency doubled in a folded ring cavity with a non-linear crystal to 531 nm with about 5 W of power. This light is subsequently combined with the remaining light of the fundamental and sent into another cavity of the same type where the sum frequency is created. This way, an output power of > 400 mW at 354 nm can be achieved. Both cavities are length stabilized using a Hänsch-Couillaud lock with automatic relocking. The seed laser is frequency stabilized onto an optical frequency comb and has a specified linewidth of <100 kHz corresponding to <300 kHz after frequency tripling. This is many orders of magnitude smaller than the typical spacing between rotational lines of formaldehyde, so that rotational state selective detection of the molecules is possible.

Stray light problem First measurements with the setup described in this section showed an immense background caused by stray light of about $4 \times 10^{10} \frac{\text{cnts}}{\text{s mW}}$. This light has several sources: Firstly, there is a direct line of sight from outside the vacuum chamber onto some parts of the LIF mirror which means that stray light created at optics outside of the mirror can get imaged directly onto the PMT. Secondly, light in the outer parts of the laser due to deviations from an ideal Gaussian beam profile can hit the mirror surface directly or can get scattered and create stray light. A third source of background signal is fluorescence light from optical elements. At a wavelength of 354 nm virtually every optics such as mirrors, lenses, or vacuum windows start to fluoresce due to the excitation of e.g. colour centres in the material. This fluorescence background is particularly harmful because it can not be filtered due to the spectroscopic overlap it typically has with the fluorescence spectrum of formaldehyde.

The magnitude of the stray background light problem can be seen with a quick estimate. For a laser power of 100 mW at 354 nm the photon flux of the excitation laser beam is $1.8 \times 10^{18} \frac{1}{\text{s}}$. Now, assuming a number of $10^6 \frac{1}{\text{s}}$ molecules with a detection efficiency of 1 % a typical signal would be on the order of $10^4 \frac{1}{\text{s}}$. Now, if only a tiny fraction of 10^{-10} of the excitation laser light is scattered onto the surface of the LIF mirror and is detected with an efficiency of 1 %, the background would still be about two order of magnitude larger than the molecule fluorescence signal. From this still very conservative example the extent of stray light suppression necessary to achieve efficient detection of formaldehyde becomes clear. The next section is dedicated to the various strategies used to overcome this difficult challenge.

3.3 Stray light suppression

The main strategy to tackle the immense problem of stray light suppression is to add apertures at the entrance and exit of the LIF mirror such that there is no

direct line of sight from the outside of the detection area onto the LIF mirror. This prevents scattered laser stray light or fluorescence light of optical elements from being collected by the LIF mirror and imaged onto the PMT. Equally important as adding apertures is improving the beam quality in order to minimise the amount of laser light hitting the aperture edges, and therefore the amount of stray light created. Both techniques are insufficient on their own and can only unfold their full potential in combination.

Stray light values are given in the unit $\frac{\text{cnts}}{\text{s mW}}$ referring to the number of clicks detected by the PMT due to stray light per second and every mW of laser power sent through the chamber. The laser power necessary to saturate the detection transition is on the order of several tens of mW depending on the temperature (see Section 4.5.1) and the fluorescence signal of the molecules is on the order of 10^3 counts. Therefore, the targeted stray background count rate is about $10\,\frac{\text{cnts}}{\text{s mW}}$ to achieve a good signal-to-noise ratio.

This section presents the implementation of stray light suppression, mainly via both of the mentioned techniques. Firstly, different measurement and detection methods for stray light and the laser beam profile are presented in Section 3.3.1. Secondly, a strategy for improving the laser beam quality is developed and implemented in Section 3.3.2. Thirdly, the in-vacuum aperture configuration used to block stray light is laid out in Section 3.3.3. Lastly, in Section 3.3.4 additional measures helping to reduce the amount of stray light are summarised.

3.3.1 Measurement methods for stray light and laser beam profiles

In the course of the work of this thesis a variety of methods for the detection of stray light and determining laser beam profiles were employed. Here, a short overview over the techniques most widely used is given.

Beam profiler Probably the simplest method to determine a lasers intensity beam profile is to use a beam profiler, i.e. a camera directly detecting the laser light of the beam. For this thesis work the thermal camera Pyrocam III by Ophir-Spiricon is available. In Figure 3.5(a) a beam profile measured with this camera is shown. The main advantage is its ease of use as it allows determination of the beam profile at various positions along a beam in a very short time. However, due to the finite pixel spacing of 100 µm measurements get inaccurate for smaller beams that only cover a few pixels. Also, a precise determination of the outer lobes of the beam profile is not possible, due to a maximum signal-to-noise ratio of about 1000:1.

Knife Edge method Another standard technique for the determination of laser beam profiles is the Knife Edge method. Here, the power of the beam is measured by e.g. a photodiode and a sharp blade to minimise reflection at the edge, hence knife edge, is moved incrementally into the beam covering it partially. The transmitted power is measured and thus the integral over the two-dimensional beam profile can be recorded. This technique is much more cumbersome than using a beam profiler. However, precise values can be obtained even for small profiles on the order of tens of microns. The technique is applicable roughly down to a suppression of 10^{-3}-10^{-4}

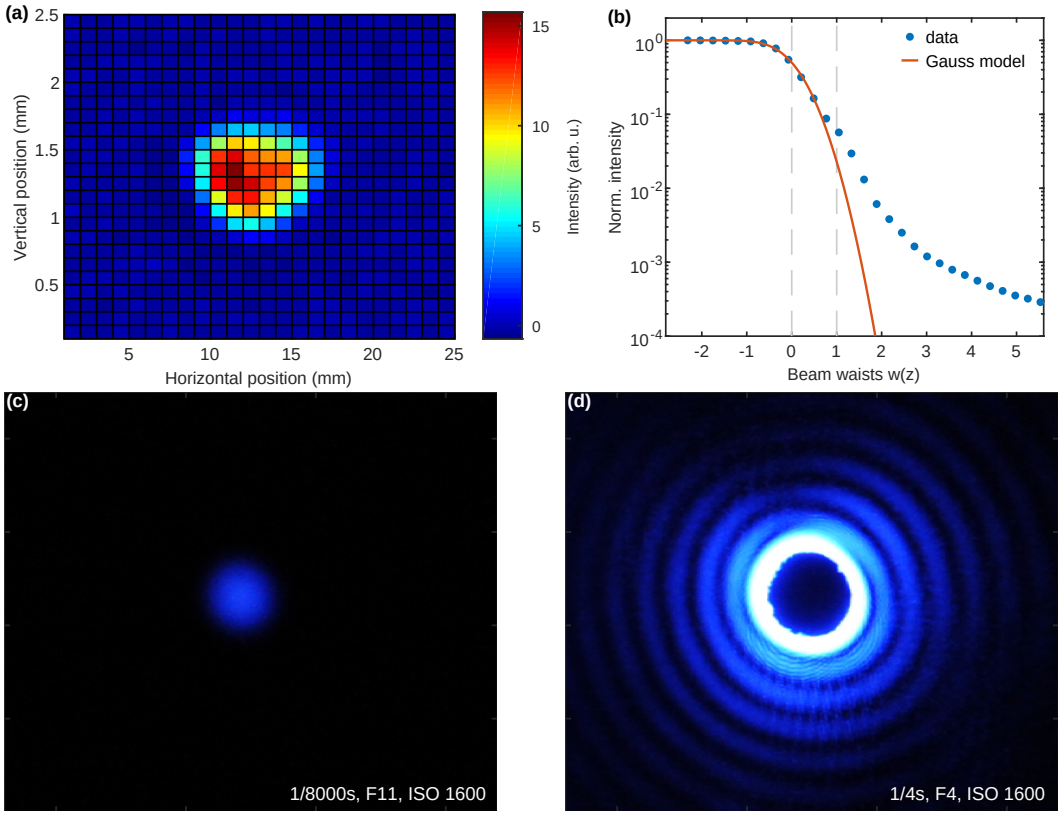

Figure 3.5: Comparison of different laser beam profile measurement techniques. **(a)** Measurement using a Beam profiler. **(b)** Measurement employing the Knife-Edge method. **(c)** Picture of the fluorescence of paper illuminated by UV-light taken with a digital camera. **(d)** Sending the main beam through a hole in the paper also allows the visualisation of the very weak outer parts of the beam. The edge of the dark spot in the centre corresponds to the slightly jagged edge of the hole in the paper.

in intensity in the outer parts of the beam because at some point scattered light at the not perfect edge starts to dominate the measurement. In Figure 3.5(b) such a Knife Edge measurement is shown. The beam profile starts to deviate from the ideal Gaussian shape at about the 10^{-1} level of relative intensity which probably corresponds to an actual physical deviation. However, at the 10^{-3} level there is a further trailing off of the beam shape and it is not clear whether this is just a measurement artefact from scattered light at the edge of the blade or if it actually stems from light far outside of the assumed Gaussian shape.

Fluorescence on paper An excellent but somewhat qualitative detection method for UV light is the observation of the fluorescence of paper. Due to the organic compounds used to bleach white paper it fluoresces with high efficiency. This can be used for either detecting scattered light or also for measuring laser beam profiles. As the central spot of a beam causes the by far brightest spot, the beam can be sent through a hole in the paper so that only the outer parts of the beam become visible. This technique allows for very quick alignment of e.g. pinholes or iris apertures even

for rather low light levels due to the high sensitivity of the eye. To achieve an even higher sensitivity the fluorescence can be recorded with a digital camera. To get a quantitative measurement a calibration photo can be taken of the central part of the beam. To do so, the exposure has to be adjusted in order to not overexpose the photo. Using the whole dynamic range of a modern day commercial digital camera, an extraordinary low relative intensities of $<10^{-10}$ would in theory be resolvable[3]. However, Rayleigh scattering in air dominates at this point and limits the sensitivity to about 10^{-7}-10^{-8}. As an example, in Figure 3.5(c) the overall profile of a laser beam with Gaussian shape is given. In Figure 3.5(d) the same beam is sent through a hole in the detection paper making visible diffraction rings suppressed by about four orders of magnitude.

LIF detection setup Ultimately, the most meaningful way to detect stray light is with the LIF detection setup itself. When a low enough stray light level is detected with this system, the consequence is that the detection of molecules is feasible. For optimisation purposes the highly sensitive PMT can be exchanged by a simple photodiode in order to avoid damage caused by too high light intensities. Once a higher sensitivity is required the measurements can be performed with the PMT. At room pressure Rayleigh scattering contributes to the stray light background with about $1.5 \times 10^5 \frac{\text{cnts}}{\text{s mW}}$ making measurements for further improvements rather tedious due to long waiting times caused by evacuation of the system.

3.3.2 Beam cleaning

In this section a strategy is developed on how the beam quality of the laser used for detection of the molecules can be improved. However, beam quality is not a well defined quantity. The beam propagation factor M^2 based on the second moment of the beam's intensity profile is often quite useful for a description of the beam [Sie98]. For an arbitrary beam this value can be quite challenging to measure [Nem94] rendering it unsuitable for an application where the beam has to be characterised many times to arrive at an optimal solution. Furthermore, the M^2 factor mainly describes the focusing properties of a beam, not its shape. For this work the main interest lies in the side lobes as a high intensity here can cause significant amounts of stray light when the beam gets truncated by apertures and the light is scattered. Therefore, the main focus is on the deviation of the beam profile from an ideal Gaussian shape and at what relative intensity this deviation occurs. Note, that a beam with a perfectly Gaussian intensity profile does not automatically indicate a 0th mode Gaussian beam since the phase profile of the beam is also relevant. This becomes apparent when focusing the beam and results in $M^2 > 1$ [Sie98].

Improving the beam profile by sending the beam through an optical fibre is not a satisfactory solution in the case described here. Optical fibres only approximately support a Gaussian 0th order mode [Brü15] and the resulting beam profile does not satisfy the demands for beam cleaning needed for LIF detection of formaldehyde.

[3] Assuming standard specifications of modern digital cameras, a practical upper bound for the short calibration exposure is 1/8000s, F32, ISO 100. For the long exposure with the beam passing through a hole an exposure of 60s, F2.8, ISO 25600 is assumed.

Using a fibre as an initial beam cleaning step is also not an option as the high UV power needed quickly degrade any standard fibre. As a result, a spatial filtering approach was chosen to improve the beam quality.

Theory Spatial filtering is a very common approach to improve laser beam quality and creates a beam with a large overlap with a Gaussian TEM_{00} mode. The working principle is to focus the beam through a pinhole and subsequently truncate the arising diffraction rings with an aperture. In this paragraph the procedure is investigated theoretically.

A simple method to simulate the influence of pinholes and apertures on a beam consisting of an arbitrary combination of Hermite-Gaussian modes is to use a beam propagation method based on Fourier transformations [Sie86]. To this end, such a beam is considered in two dimensions with direction of propagation z and direction of the electric field x. Its field can be decomposed into a distribution of plane waves at the position $z = 0$

$$E(x, z = 0) = \frac{1}{2\pi} \int_{-\infty}^{+\infty} A(k_x, 0)\, e^{\mathrm{i}k_x x} dk_x, \tag{3.2}$$

with $A(k_x, 0)$ the complex amplitude of each plane wave component. This expression simply corresponds to an inverse Fourier transformation. Propagation of the field to arbitrary values of z is given by $A(k_x, z) = A(k_x, 0)\, e^{\mathrm{i}k_z z}$. Consequently, in the paraxial approximation where $k_z = \sqrt{k^2 - k_x^2} \approx k\left(1 - \frac{k_x^2}{2k^2}\right)$ the field is given by

$$E(x, z) = \frac{1}{2\pi} e^{\mathrm{i}kz} \int_{-\infty}^{+\infty} A(k_x, 0)\, e^{\mathrm{i}k_x x} e^{-\mathrm{i}\frac{k_x^2 z}{2k}} dk_x. \tag{3.3}$$

Therefore, to find the field at position z, first the complex amplitude has to be determined by a Fourier transformation $A(k_x, 0) = \frac{1}{2\pi} \int_{-\infty}^{+\infty} E(x, 0)\, e^{-\mathrm{i}k_x x} dk_x$, which can then be propagated and transformed back to real space by employing Equation (3.3).

The effect of thin lenses onto the beam is also easy to implement in this formalism. To this end, the field of a Gaussian beam in terms of the complex beam parameter $q(z)$ is considered [Sie86]

$$E(x, z) = \frac{1}{q(z)} e^{-\mathrm{i}k\frac{x^2}{2q(z)}} \quad \text{with} \quad \frac{1}{q(z)} = \frac{1}{R(z)} - \mathrm{i}\frac{\lambda}{\pi w^2(z)}. \tag{3.4}$$

A lens simply transforms the complex beam parameter by

$$\frac{1}{q_f(z)} = \frac{1}{q_i(z)} - \frac{1}{f} \tag{3.5}$$

with the lens' focal length f. Since the beam width $w(z)$ is not affected by the lens, its influence on the beam is simply given by a multiplication with the factor

$$e^{\mathrm{i}k\frac{x^2}{2f}}. \tag{3.6}$$

Propagating a beam in this manner has several advantages: Firstly, by relying on Fourier transformations the propagation is computationally fast due to FFT algorithms. Secondly, the method is applicable to arbitrary beams where a decomposition into Laguerre- or Hermite-Gaussian modes would not be feasible anymore.

And lastly, the effect of pinholes and apertures can easily be simulated by adjusting the electric field in real space at the location of the aperture and continuing the propagation with the adjusted field.

In Figure 3.6(a) an arbitrary beam consisting of many higher order contributions, as can be seen by the strong side lobes and the higher frequency components on the beam profile, is shown in blue. The red curve is a fit of a Gaussian TEM_{00} mode of the electric field, which not only takes into account the width of the beam but also the radius of curvature of the wavefront. The beam is in its far-field and gets truncated such that 30 % of the power contained in the beam is cut away, indicated by the gray dashed lines. In the next panel, in Figure 3.6(b), the beam is propagated into its focus. In blue, the beam that got truncated in the far field is shown, now featuring strong but smooth side lobes. The yellow curve is the propagation of the original beam from Figure 3.6(a) without truncation. The gray dashed lines again indicate the position of truncation for the altered beam, this time cutting away the side lobes in the first minimum.

In Figure 3.6(c) the beam is once again propagated into the far field once for the beam truncated in the focus (in blue, denominated 'Beam 2') and once for the beam without truncation in the focus (in yellow, denominated 'Beam 1'), but still including the truncation shown in the first panel. This procedure is repeated in the following panels of Figure 3.6(d)-(f). It can be seen that by this approach, i.e. truncating the beam by cutting away any undesired features and then propagating the beam until a Gouy phase of about $\frac{\pi}{2}$ has been accumulated before again removing the arising side lobes, the beam profile can be cleaned quite effectively. The starting beam has deviations from a Gaussian shape in the few times 10^{-2} relative intensity range, whereas the final beam, after truncation three times in the far field and two times in the focus, is nicely Gaussian down to the 10^{-5} level. Naturally, the exact mode composition or field of the beam used in the experiment is not known. However, the described procedure in theory proved to be effective for arbitrary beams and gives a good starting point for the experimental implementation of a beam cleaning setup.

The above treatment is done for the two-dimensional case which would correspond to rectangular apertures when applied to three dimensions. Since in practice apertures are typically round the integrations in Equation (3.3) have to be performed in cylindrical coordinates. This gives rise to Bessel functions in the transformation stripping the method of the convenience to be able to perform Fourier transformations for the propagation. However, the result is qualitatively the same and the strategy to clean the beam as described above remains.

Setup and result Based on the beam cleaning strategy developed theoretically the beam cleaning setup sketched in Figure 3.7 is implemented. It consists of six apertures truncating the beam in the far field combined with four pinholes cutting into the beam in the focus. The collimated section between Aperture 4 and Aperture 5 is needed for propagating the beam from the optical table onto a small breadboard in front of the vacuum chamber. Two apertures are added because also here some additional Gouy phase is collected. In each step the beam is truncated in the first minimum so that diffraction rings are removed. After the additional collection of a Gouy phase of approximately $\frac{\pi}{2}$ the newly arising diffraction rings are again cut away.

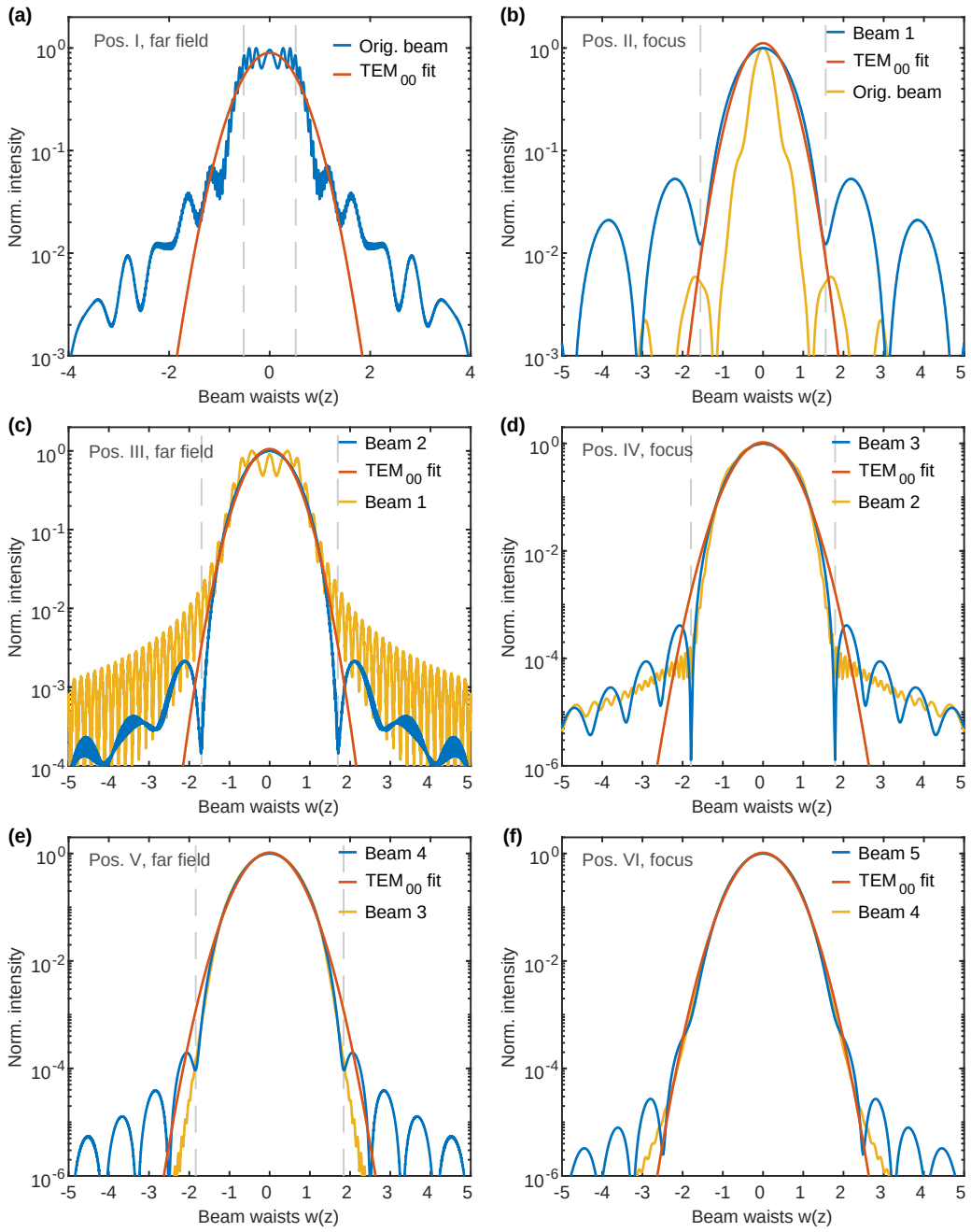

Figure 3.6: Theoretical development of a beam cleaning strategy. **(a)** The starting beam in the far field with significant deviations from a Gaussian shape is shown in *blue* whereas the *red* curve depicts a Gaussian fit of the field. The *gray* dashed lines indicates where the beam is truncated. **(b)** The truncated beam (*blue*) and the original beam without truncation (*yellow*) after propagation into the focus. **(c)** - **(f)** Repetition of the scheme from the first two panels. The beam is truncated at the minimum of the side lobes and then propagated from the focus to the far field and vice versa. The beams represented in *blue* correspond to the beams excluding the previous truncation step but including the truncations performed before.

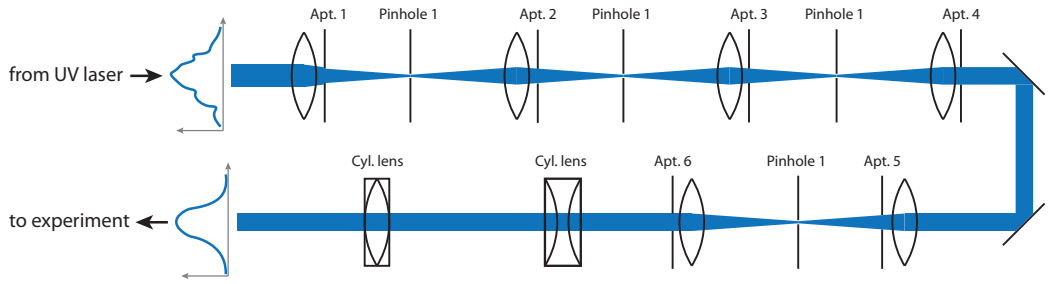

Figure 3.7: Beam cleaning setup for the UV laser. The beam is sent through a succession of apertures and pinholes cutting away undesired features of the beam in the focus and far field of the beam improving the overlap with a Gaussian beam shape in each step.

Experimentally, this is performed by making use of the technique of observing the laser beam via the fluorescence it causes on paper as explained in Section 3.3.1. In the far field, a piece of paper can be placed directly at the position of the aperture to image the beam and determine the necessary aperture size. However, this is not possible at the foci due to the small size of the beam. Therefore, these foci are projected onto much larger foci by a single focusing lens enabling the same procedure as in the far field. Additionally, in both cases the beam can be widened to further improve the visibility by using a defocusing lens without adding additional Gouy phase. It was observed that with extreme care during alignment the end result does no longer improve after three sets of pinholes and apertures. However, adding a fourth pinhole substantially reduces the effort needed for alignment.

The result of the beam cleaning is shown in Figure 3.8. The beam shape is recorded by taking photos of the fluorescence the UV light causes on a sheet of paper with a common digital camera (Nikon D700 equipped with Nikon AF-S Nikkor 24-70mm/2,8 E ED objective). To record the outer weak parts of the beam it is sent through a hole in the paper in order to not saturate the photograph in centre of the beam. To cover the full dynamic range several photographs with different exposures have to be taken. Since the fluorescence of paper is located spectrally in the blue wavelength regime for the evaluation the camera's blue channel value is extracted. The result is stitched together from the different exposures taken for each beam profile. The scaling of each individual contribution to the beam profile measured in this way is determined by the exposure time, F-number and the ISO value[4].

The first two panels of Figure 3.8 show the beam in the near and the far field before beam cleaning, as it is emitted by the laser setup described in Section 3.2. Deviations from a Gaussian shape already occur at the 10^{-1} and 10^{-2} level respectively. The last two panels show the beam after beam cleaning. It now follows a Gaussian shape down to about the 10^{-5} to 10^{-4} level. This corresponds to a typical result and with the appropriate care even better suppressions can be achieved. However, the resulting improvement is small compared to the additionally experimental

[4]The F-number is used in photography to describe the size of the entrance pupil of an objective and determines the light collection efficiency. It is given by the ratio of the focal length and the diameter of the entrance pupil. The ISO value describes the signal gain of a photographic image sensor.

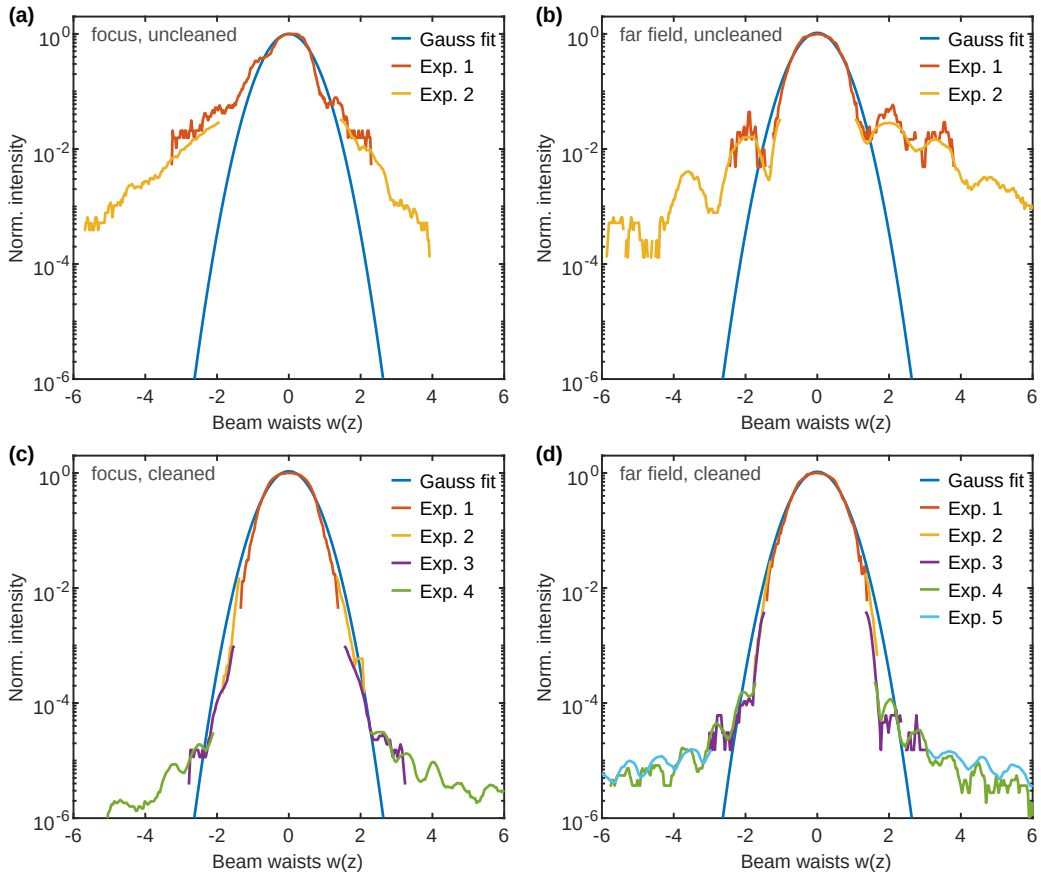

Figure 3.8: Beam profile measurements via fluorescence on paper. The curves are extracted from photographs of the fluorescence the UV laser beam induces on paper. In order to cover the full dynamic range the curves are stitched together from various photos of different exposure. To avoid saturation for the longer exposures the centre part of the beam is sent through a hole in the paper. In panels **(a)** and **(b)**, the beam before passing through the beam cleaning setup is shown in the focus and the far field. Panels **(c)** and **(d)** show the focus and far field after beam cleaning. A clear improvement by several orders of magnitude is achieved.

effort necessary for alignment and already with the shown improved beam shape, truncating the beam at e.g. three time the beam waist $w(z)$ should create orders of magnitude less stray light.

Evidently, these measurements are rather qualitative as perfect linearity is assumed for all photographic parameters as well as the camera chip response or rather the camera internal processing of the light captured by the chip. Also, it is not possible to infer the absolute size of the beam from the measurements as there is no size standard to compare with. However, the purpose of this measurement is not a quantitative determination of beam parameters but rather a qualitative proof of the effectiveness of the beam cleaning setup and this point is proven clearly.

3.3.3 In-vacuum apertures

All optical elements contribute to the stray light background. Surface roughness or bulk inhomogeneities lead to stray UV laser light. Furthermore, all surfaces, in particular anti-reflective coatings, but also optical glass such as UV fused silica fluoresces to some degree. This fluorescence typically spectrally overlaps with the fluorescence of formaldehyde making it a particularly harmful contribution to the stray light background. Due to these sources of stray light it is indispensable to place apertures before and after the detection volume around the UV laser passing through the vacuum chamber for a successful stray light suppression. The purpose of these apertures is to block any direct line of sight path from outside of the vacuum chamber onto the LIF mirror surface. Since the last unavoidable optical elements before the detection area are the vacuum windows, the apertures have to be placed inside of the vacuum chamber.

In order to investigate different aperture configurations and their effect on the stray light background a test setup was built. This test setup has the same proportions as the actual vacuum chamber setup with the difference that it is in air and the inner part, where the LIF mirror would be located, is openly accessible. Thus, investigating the influence of different beam cleaning approaches and aperture configurations is greatly facilitated because the stray light can be observed directly within the mock vacuum chamber. The same laser beam that is used for the vacuum chamber can be used for the test setup.

As a first approach an aperture configuration consisting of two apertures on either side, blocking the direct line of sight, was tested. Position and size of the apertures was optimised such that for a diagonal connection between apertures, i.e. from the upper edge of the first aperture to the lower edge of the second aperture, and a line from the edge of the second aperture onto the surface of the LIF mirror, the intersection angle is maximised. This should minimise the amount of diffracted light hitting the mirror surface. Of course, a boundary condition is the depth up to which the apertures are allowed to cut into the laser beam, because if the beam is truncated to much any previous beam cleaning efforts would be in vain. With this approach the amount of stray light background could be reduced significantly but the achieved background, also including other measures described in Section 3.3.4, was still about three orders of magnitude to high.

The test with two apertures showed that also the light diffracted or reflected at the second aperture edge still causes a considerable amount of background. Therefore, as next step a third aperture was added. The configuration was chosen such that the two apertures closest to the LIF mirror block the direct line of sight onto the mirror surface. The third aperture furthest away from mirror, together with the middle aperture, now also creates a shadow on the edge of the closest aperture. By again maximising the necessary scattering angles a considerable improvement should have been possible by this blocking of the line of sight even for diffracted light. Unfortunately, no significant improvement could be achieved with this configuration. Most likely the reason is that at least one very small aperture is required, making the configuration rather susceptible to misalignment.

As a consequence a more pragmatic approach, relying on practical considerations,

is taken. The approach implements what has been learned with the previous tests, i.e. that even the path onto the LIF mirror surface for scattered light has to be blocked and that the configuration has to be robust towards slight misalignment, which is achieved by further increasing the number of apertures. The configuration was adjusted with the test setup before arriving at the final result. In the following this result is described and the constraints that have to be considered are discussed.

Naturally, placing the outermost apertures as far away from the LIF mirror as possible, facilitates achieving the goal of having multiple scattering events before light can hit the LIF mirror surface. However, for large aperture distances the laser focus in the centre of the LIF mirror has to be chosen larger in order to reduce the divergence of the Gaussian beam. Otherwise the outermost apertures would have to either cut deeply into the laser beam, which would create more stray light, or larger apertures would be required which could not block beam paths from outside of the chamber effectively. A larger focus on the other hand calls for larger apertures close to the detection region in order to avoid truncating the laser beam there. Therefore, a compromise between the size of the laser beam focus, the position of the furthest apertures, and the size of the individual apertures has to be taken. The position of the apertures furthest away from the LIF mirror determines the size of the whole apparatus. The largest distance that can easily be fit into the laboratory with the current infrastructure is 0.8 m which is why this value is chosen. The number of apertures on each side of the detection area is set to six as this is still an experimentally tractable number.

The configuration chosen for the apertures in horizontal and vertical direction is presented in Figure 3.9. The apertures represented in black are spaced such that the distance between individual apertures decreases logarithmically towards the detection region which is shown in red. The laser beam passing through the LIF mirror is indicated in grey. The maximum value to which the apertures can cut into the beam without significantly inducing stray light is experimentally determined to be $3\,w(z)$. This value is also plausible when looking at the beam profile in Figure 3.8, as for this value the beam starts to deviate from the ideal Gaussian shape. The size of the two pairs of apertures furthest away from the detection region is adjusted to the size of the beam, truncating it at $3\,w(z)$. Therefore, their size is ultimately given by the size of the laser beam focus. These apertures are the ones cutting the deepest into the laser beam, thereby potentially creating stray light. The inner apertures slowly open up towards the detection area. It can be seen from the blue dashed line that with this design even light scattered at the second aperture is blocked by several of the inner apertures from hitting the LIF mirror surface directly, giving the setup the desired robustness towards misalignment. If a larger multiple of the waist $w(z)$ was chosen for the outer apertures to cut into the laser beam, this would not be the case anymore. The size of the apertures is different in the vertical (Figure 3.9(a), parallel to molecule beam) and the horizontal (Figure 3.9(b), perpendicular to molecule beam) direction. In the horizontal direction the size of the laser is given by the spread of the molecule beam as mentioned previously in Section 3.2. A value of $w_{0,\mathrm{hor}}$=3.33 mm is chosen as design parameter for the horizontal focus of the elliptical laser beam, which is based on the result of molecule trajectory simulations. A measurement of the width of the molecule beam resulting

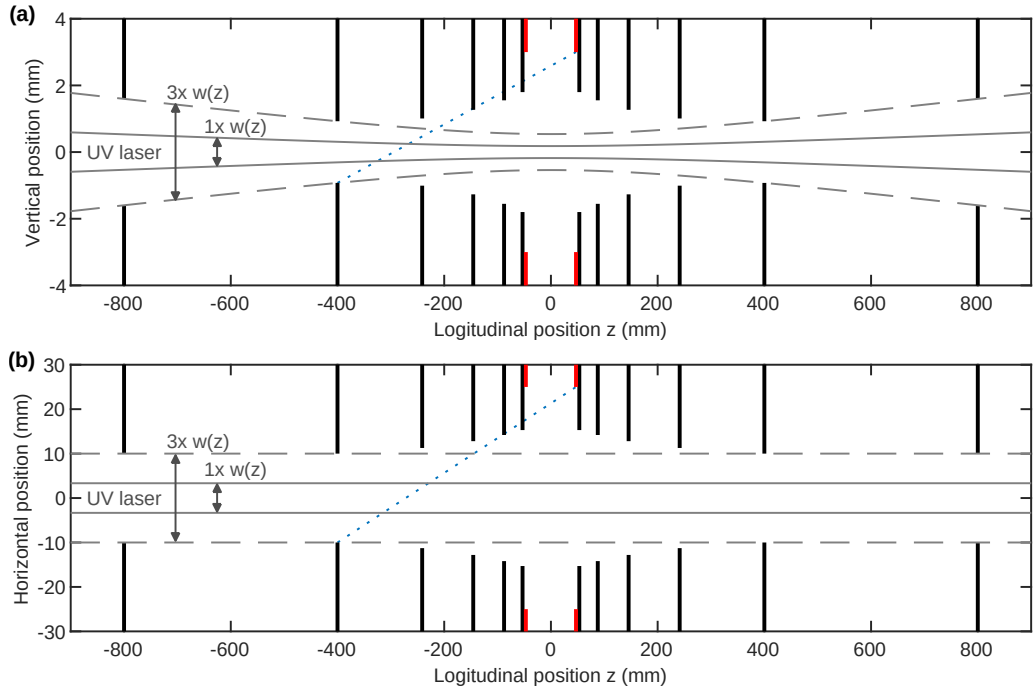

Figure 3.9: Aperture configuration for the LIF detection setup. Apertures are represented in *black*, the LIF detection mirror in *red* and the laser beam in *grey*. The outermost two of the six apertures on each side cut into the beam at $3w(z)$. The remaining apertures gradually open up towards the LIF mirror. Stray light created at the second aperture (dashed *blue* line) is still blocked by several apertures. **(a)** Aperture configuration in the vertical direction based on a beam width in the focus of $w_{0,\mathrm{ver}}$=0.18 mm. **(b)** Aperture configuration in the horizontal direction based on a beam width in the focus of $w_{0,\mathrm{ver}}$=3.33 mm determined by the size of the molecule beam.

in an actual width of 2.2 mm is presented in Section 4.5.1. In the vertical direction the focus has to be much smaller due to the smaller entrance aperture of the LIF mirror. For the reasons already mentioned a compromise has to be found which is fulfilled by the design parameter of $w_{0,\mathrm{ver}}$=0.18 mm in the vertical direction.

The apertures are shaped as elongated holes. They are manufactured out of copper and the aperture edge is made as sharp as possible with a width of <0.1 mm to minimise reflections and diffraction at the edges. The apertures are aligned to each other and to the laser beam with a precision of <0.1 mm. However, the alignment of the apertures to the LIF mirror is less precise due to manufacturing tolerances of the involved vacuum parts. A photograph of a part of the aperture setup is shown in Figure 3.10.

3.3.4 Further measures

Additional measures to lower the amount of the stray light background, apart from beam cleaning and adding apertures, are discussed in this section.

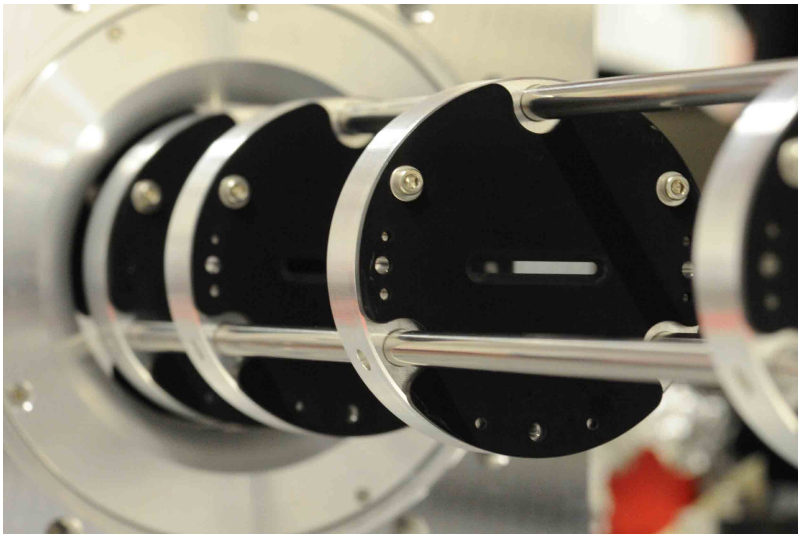

Figure 3.10: Photograph of the aperture setup. The picture shows the innermost four apertures of the setup. The elongated hole with different dimensions in horizontal and vertical direction can be seen. The apertures are manufactured out of copper and oxidised to reduce their reflectivity and make them black (see Section 3.3.4).

Blacken the inside of the vacuum chamber Blackening the insides of the vacuum chamber can greatly reduce the stray light background [Xu18]. For this reason, the apertures are manufactured from copper which allows blackening them by oxidation. The copper is immersed in a hot solution of NaOH and $NaClO_2$ which creates black cupric oxide (CuO) on the surface [Nor16b]. The copper blackened by this procedure has a reflectivity well below 1 % in the UV and experiences virtually no fluorescence. Other parts of the vacuum chamber that cannot easily be manufactured from copper are blackened by using the ultra-high vacuum proof paint MH2200 by Alion Science and Technology which has a reflectivity on the order of a few percent [Ham17].

Vacuum windows under Brewster's angle Instead of using windows with an anti-reflective coating whose surface is oriented perpendicular to the laser beam, uncoated windows under Brewster's angle are used. This way the reflection can be reduced to a bare minimum and even if a part of the beam is reflected due to misalignment or a non-perfect linear polarisation of the laser beam, this part is reflected under a large angle. Therefore, there is no risk of the reflection hitting the aperture edges and creating additional stray light, as is the case for perpendicular windows, but instead the reflection can be dumped safely.

Spectral filters Adding an optical long-pass filter in front of the PMT can lower the background level by several orders of magnitude. The best solution was found to be an absorbing colour filter (Schott GG385) that has a transmission of only 3×10^{-4} for 354 nm while still having a high transmission rising from 0.5 at 380 nm to 0.9 at 450 nm. A detailed transmission curve is plotted in Figure 4.15 together with the determination of the detection efficiency. Adding additional colour filters

does not improve the suppression of the laser frequency anymore because the filter material itself slightly fluoresces with a spectrum in the region of the passband. In principle, for interference filters much higher suppression factors and steeper slopes of the the transmission curve can be achieved. However, due to the particular design of the LIF mirror, many different angles of incidence for the incoming light occur, for which the transmission edge gets shifted. This leads to the effect that stray light at the laser frequency is not blocked by the filter once the angle is steep enough. Furthermore, an interference filter has the disadvantage that the blocked light is reflected instead of absorbed. Due to the elliptical part of the LIF mirror on the opposite side of the filter the light will only be reflected back onto the filter with the main loss mechanism being the finite reflection of the coating of the LIF mirror.

High quality optics The optics used in the beam cleaning setup, in particular all optical elements after the beam cleaning, are chosen with great care. They have a surface with a scratch-dig value[5] of 10-5, which should minimise the amount of laser light scattered by the surfaces. However, no relevant improvement could be found in the detected stray light level by employing this type of low surface roughness optics. What proved to be very important though, is to be aware of lens errors. For many lenses, also from different manufacturer, unexplained lens error were observed which can significantly increase the amount of stray light incident on aperture edges. These errors include e.g. strong focused spots on a line somewhat resembling lens flare or a weak defocussed beam originating in the centre of a focussing lens. The origin of these errors was not further investigated as switching to a second identical lens typically solves the problem.

A further criterion for the choice of optics are the fluorescence properties. All optical elements employed only show a minimal amount of fluorescence under illumination with UV laser light. This is of particular importance for the vacuum windows which are by far the closest to the aperture setup. Mostly, the fluorescence properties of optical glass and anti-reflective coatings are not specified and have to be found by a trial-and-error approach.

Laser beam block In order to avoid creating more stray light in the detection region the laser leaves the vacuum chamber through a similar aperture configuration as it passes for entering the chamber. However, the beam still has to be extinguished with great care. To this end, a special beam dump coated with Acktar black foil is used which is specified to have a reflectivity of $<10^{-6}$.

Mirror insets The origin of the remaining stray light after the implementation of the in-vacuum apertures and the beam cleaning was again investigated in the test setup. By putting a piece of paper with an elongated hole at the position of the laser entry and exit aperture of the LIF mirror, such that the mirror surface is represented by paper, and taking a photograph, the remaining stray light can be made visible

[5] Scratch-dig is a specification based on the number and size of surface impurities like grooves (scratch) and holes (dig). Even though the value is somewhat objective a low scratch-dig value is typically a prerequisite for stray light prevention.

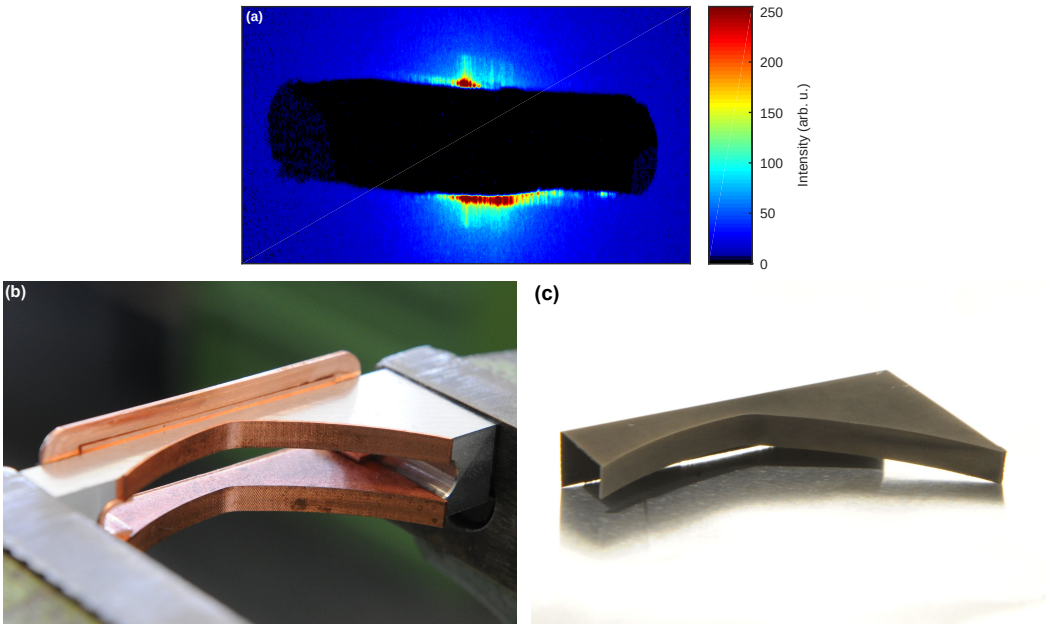

Figure 3.11: Mirror insets for the LIF mirror. **(a)** Blue channel of a photograph of the fluorescence of paper positioned at the laser exit hole of the LIF mirror in a test setup. The stray light remaining after beam cleaning and adding the apertures is mainly found close to the edge of the exit hole. **(b)** LIF mirror insets made from copper before blackening on a dummy model of the laser exit hole of the LIF mirror. **(c)** Picture of a blackened inset. Note that the photo is strongly overexposed outside of the inset due to the low reflectivity of the oxidised copper.

due to its fluorescence. The blue channel of this photo is shown in Figure 3.11(a). In order to not be limited by Rayleigh scattering, in this measurement the amount of stray light was greatly increased by introducing a very thin peace of lens cleaning tissue outside of the aperture configuration. As can be seen from the photograph, the stray light is mostly hitting the edge of the laser exit hole of the LIF mirror and quickly abates away from the aperture. The source of the light is not entirely clear and there is different conceivable options. Most likely it is light which is diffracted or reflected at the edge of the second aperture as this is the last one which actually cuts into the beam as can be seen from Figure 3.9. However, as previously explained from this edge there is no direct line of sight onto the mirror surface. Therefore, it has to be a second order process, i.e. the light is again reflected or diffracted at one of the edges of the following apertures. Another possibility is that the stray light created at the second aperture hits the backside of the apertures on the opposite side of the detection volume and is reflected back into the mirror. For this beam path there is a direct line of sight, but it is also a second order process as it involves a reflection of diffracted light at a blackened copper surface.

Since the origin of the stray light at the LIF mirror edge is not clear it is hard to remove its source. An obvious solution would be to increase the size of the laser entry and exit apertures which would only slightly affect the covered solid angle and prevent the light from being imaged onto the PMT. However, machining the

LIF mirror poses a great risk of damage due to the delicate surface of the mirror. Buying a completely new mirror with adjusted measures is also not an option due to time and funding constraints. Therefore, a less invasive approach is chosen by covering the most strongly affected area of the LIF mirror surface in order to absorb the incident stray light.

Blocking the light at the edges is achieved by the use of special mirror insets. In Figure 3.11(b) the application of the insets manufactured from copper is shown on a dummy model of the laser entry and exit hole of the LIF mirror. The copper is only 0.1 mm thin so that the size of the laser exit hole is not significantly affected. The stripe within the detection volume has a height of 4 mm which results in a loss of solid angle of only 4.5 %. The insets are clamped in place in order to be minimally invasive and avoid any mechanical adjustment which would carry the risk of damaging the diamond turned surfaces of the LIF mirror. Blackening the copper insets by oxidation as previously mentioned ensures that light is effectively absorbed. A photograph of one final blackened inset is show in Figure 3.11(c). The introduction of these mirror insets could lower the stray light background by more than an order of magnitude and hence provides a major reduction in stray light background after the implementation of the in-vacuum apertures and the beam cleaning.

3.4 Final setup

The final setup for LIF detection of formaldehyde now includes all points addressed in the previous sections. The UV laser beam profile is cleaned by a succession of pinholes and apertures which truncate the beam in the focus and far field respectively such that the resulting beam has a Gaussian profile down to the 10^{-5} level. All optical elements are chosen carefully in order to minimise surface scattering and fluorescence. The vacuum windows are uncoated and oriented at Brewster's angle to the beam to minimise the amount of reflection and be able to safely dispose of any remaining reflected light due to the large reflection angle. Within the vacuum chamber six apertures are installed on each side of the detection volume to block as much stray light as possible from entering from the outside. The apertures as well as other parts of the vacuum chamber are blackened to further reduce any reflection of stray light. The edges of the insides of the holes for the laser in the LIF mirror are covered by special blackened insets, absorbing the main part of the remaining stray light. The resulting effective solid angle covered by the LIF mirror in combination with the blackened insets is 74.8 %. The final ingredient is a filter in front of the PMT to filter the stray laser light from the fluorescence light. An overview in the form of a technical drawing of the vacuum chamber including the LIF mirror and the apertures is shown in Figure 3.12. The length of the whole vacuum chamber is about 3 m. Further details about the setup such as the reflectivity of the mirror coating, the transmission of the re-entrant vacuum window and the filter and the quantum yield of the PMT can be found in Section 4.5.2 together with an estimate of the detection efficiency of the detection.

The stray light background achieved with the above setup is $<10\,\frac{\text{cnts}}{\text{s mW}}$ which corresponds to an improvement by about a factor of 4×10^9 compared to the initially

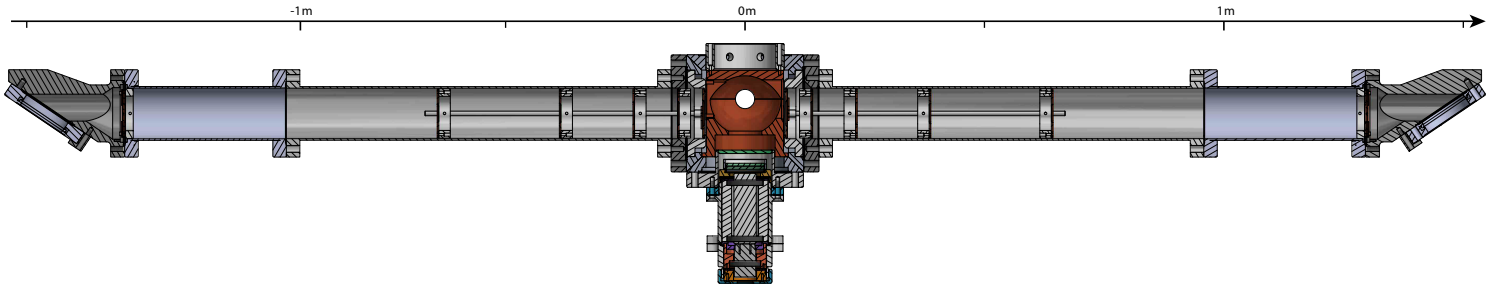

Figure 3.12: Technical drawing of the vacuum chamber containing the LIF detection setup. In the centre the LIF mirror is located. The long arms of the chamber contain the apertures used to block stray light from entering the detection volume. The hole in the centre of the LIF mirror is the entrance pupil for the electric quadrupole guide. On the lower side the casing of the PMT in a re-entrant vacuum window can be seen.

achieved value without stray light suppression (compare Section 3.2). A rough estimate is that only about one of every 10^{15} photons in the laser beam is detected as a background count. The individual contribution of the different measures for stray light suppression cannot always be quantified. One reason is that the parts within the vacuum chamber cannot simply be removed in order to examine their isolated effect. Another reason is that some measures are only effective in combination, such as the beam cleaning whose effect is greatly amplified by the in-vacuum aperture setup. The aperture's contribution is by far the largest even though hard to quantify. An easily quantifiable contribution is that of the spectral filter for the PMT which reduces the stray light by about a factor of 10^3. The insets blocking the stray lights at the edges of the holes of the LIF mirror for the laser contribute with another factor of about 10, however, only in combination with the in-vacuum aperture setup.

In conclusion, with the added improvements to the initial setup it is now possible to send a lasers beam of 100 mW through the detection chamber while maintaining a background level of about the same magnitude as the fluorescence signal for typical molecules numbers. This enables the efficient detection of formaldehyde molecules via an all optical detection scheme with the added improvement of state selectivity as will be shown in the next chapter.

4 Characterisation of LIF detection

The preceding chapter was dedicated to the presentation of the concept of a LIF based detection scheme, its experimental implementation, and a discussion of the solution to the problem of exceedingly high background levels caused by stray light. This chapter deals with the characterisation of the detection method and presents the initial measurements performed with the new setup.

To this end, first signals obtained with the new detection scheme are presented in Section 4.1. The main advantage of the method, namely its state selectivity, is demonstrated in Section 4.2. Following in Section 4.3 are measurements of the excited state lifetimes leading to a value for the quantum yield of the radiative decay of the involved $\tilde{A}^1A_2$ 4^1 $|2,2,1\rangle$ state[1] as well as other rotational states in the vibronically excited state. In Section 4.4 first measurements of cooled molecules are presented with a focus on highlighting the differences to the previous detection method using a QMS, before the detection efficiency of the method is determined in Section 4.5.

4.1 First LIF detection signals

In order to obtain a first signal of formaldehyde molecules with the newly built detection setup a very simple measurement is performed. Voltages are applied to the loading and unloading guides as well as the electric trap. This way molecules are continuously loaded into the trap. The molecules leaving the trap are a mixture of molecules passing directly from the entry to the exit of the guide and molecules that were trapped for a certain amount of time. This configuration is referred to as a fly-through measurement [Eng13] and most of the data presented in this chapter is based on this type of measurement sequence. The exit guide of the trap brings the molecules into the LIF detection volume where they are released. The UV laser passes perpendicular to the molecule beam through the LIF mirror as described in Section 3.2 to electronically excite the molecules. The resulting fluorescence light is then imaged onto the PMT and recorded. Spatial overlap of the molecule beam and the laser beam does not represent a problem, as both have a size on the order of several mm and misalignment on this scale can be excluded. For a precise alignment the exact shape and position of the molecule beam can be measured as shown in Section 4.5.1. Now, to successfully record a first signal the frequency of the UV laser has to be adjusted. The highest occupation of molecules in the loading guide after precooling with liquid nitrogen and velocity filtering is in the rotational state $|3,3,0\rangle$ which is also one of the two states used for optoelectrical Sisyphus cooling. Therefore,

[1] In this work the asymmetric rotor notation $|J,K_a,K_c\rangle$ is employed as a standard. Whenever symmetric rotor states $|J,K,M\rangle$ are used they are indicated as such.

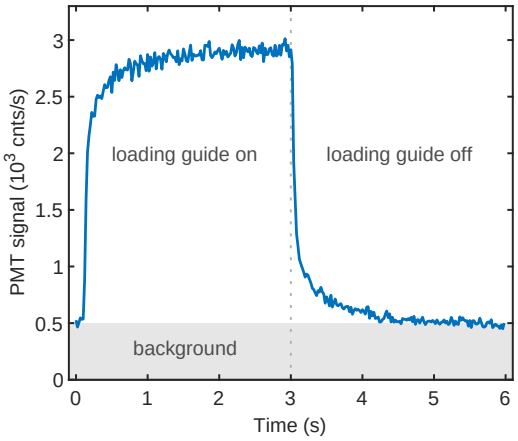

Figure 4.1: One of the first signal recorded with the newly installed LIF detection. Voltages at the electric loading and unloading guide are turned on at 0 s. The steep initial rise in signal is caused by molecules flying directly through the trap and into the LIF detection. The slower rise afterwards is caused by trapped molecules which are loaded into the trap. At 3 s the voltages at the loading guide are switched off causing the signal to decay with the same two time scales, a fast decay due to molecules only flying through the trap and a slower decay caused by trapped molecules leaving the trap.

the laser is tuned to the transition $|\tilde{A}; J{=}2, K_a{=}2, K_c{=}1\rangle \leftarrow |\tilde{X}; J{=}3, K_a{=}3, K_c{=}0\rangle$ as described in Section 3.1. However, the precise frequency is not known well enough from theory. For this reason, to find a first signal, the frequency is adjusted by hand, with the previously mentioned voltage configuration of a fly-through measurement applied, until a live fluorescence signal is recorded by the PMT.

Fixing the UV laser frequency to the found value a first measurement can be taken with the LIF detection setup. The result is shown in Figure 4.1. The voltages at the electric guides and the trap are turned on at time 0 s[2]. This results in a fast rise in signal over ∼50 ms caused by molecules only flying through the trap. The following slower rise is caused by molecules which stay trapped for some time within the trap and are unloaded much slower. At a time of 3 s the voltages at the loading guide are switched off, whereas the trap and unloading guide voltages are still applied. The signal first decays quickly due to the lack of molecules flying directly through the trap. A much slower decay follows with the same time constant a the initial slow increase, caused by the trapped molecules unloaded from the trap. The whole curve is offset by about $0.5 \times 10^3 \frac{\text{cnts}}{\text{s}}$ due to the background caused by stray laser light, which is not subtracted in this plot. This measurement shows a first signal with the newly implemented detection setup and its main purpose is to demonstrate the functionality of the whole system. Of course, there are a number of different parameters whose influence on the measurement has to be characterised. For the UV laser used for detection these parameters include the frequency, power, and polarisation as well as the spectral and spatial width. Furthermore, electric fields in the detection region play an important role and can be exploited to achieve M-

[2] Asymmetric voltages of size 3.6/0 kV are applied to the electric guides and a voltage of 1200 V±5 % is applied to the electric trap. More details are given in Section 4.2.2 or Ref. [Pre16].

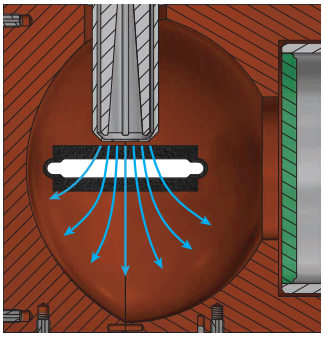

Figure 4.2: Cut through technical drawing of the LIF mirror. To the right the spherical part of the LIF mirror can be seen together with the re-entrant vacuum window which contains the PMT. To the left the elliptical part of the mirror is shown (see Section 3.2 for details). From the top the electrical quadrupole guide enters the detection area with the guide rods bending outwards to minimise the spread of the molecule beam [Mie10]. The cap surrounding the end of the guide shields the detection volume from the high electric fields within the quadrupole guide. Due to a hole in the cap, through which the molecules pass, a small electric field due to the electric guide is still present outside of the cap. Furthermore, an offset voltage can be applied to the guide cap creating an additional electric field between the cap and the grounded LIF mirror. The direction of the electric field within the detection volume is sketched by the blue arrows.

sublevel selectivity. To determine the detection efficiency also the quantum yields of the involved electronically excited states as well as the imaging efficiency are measured. These topics are addressed in the following sections of this chapter.

4.2 Demonstration of state selectivity

Rotational states for the $\tilde{A}^1A_2 \leftarrow \tilde{X}^1A_1$ 4_0^1 transition typically have a spacing of several GHz whereas the resolution of the detection should be on the order of about a MHz. Therefore, state selectivity for different rotational states does not represent a problem. However, rotational states split up by K-type doubling as well as individual M-sublevels whose degeneracy is lifted by an electric field can have a much smaller frequency splitting. In this section the state selectivity is investigated and demonstrated for these cases. To this end, the electric field distribution within the detection region is examined in Section 4.2.1. With this knowledge the UV spectra presented in Section 4.2.2 can be understood. In Section 4.2.3 the spectral resolution is increased by eliminating Doppler broadening with Doppler free saturation spectroscopy which allows measuring precise Stark maps to deduce a value for the electric dipole moment of the electronically excited state as well as the determination of an upper limit for the laser linewidth.

4.2.1 Electric field distribution in the detection area

The design of the LIF mirror is already presented in Section 3.2. A cut through a technical drawing is shown in Figure 4.2. The electric quadrupole guide enters the detection area from the top and is surrounded by a cap meant for shielding the

detection volume from the high voltages applied to the guide. An offset voltage can be applied to the cap while the mirror pieces themselves are always grounded. This configuration leads to two origins of electric fields. The first is a voltage directly applied to the guide cap while the second origin are voltages applied to the electric quadrupole guide. Here, in principle many voltage configurations are possible. However, in practice there are only two relevant cases: Pairs of electrodes opposite to each other are set to the same potential in order to create a rotationally symmetric guiding potential for the molecules. This leaves two different configurations. For *asymmetric* guide voltages one pair of electrodes is grounded and the other pair is set to high voltages such that a smooth transition without difference in potential from the trap to the guide can be achieved. This configuration is chosen for unloading after cooling the molecules via optoelectric Sisyphus cooling [Zep13, Pre18]. For *symmetric* guide voltages the same voltage but with opposite sign is applied to each pair of electrodes. This configuration is used to minimise the electric field in the detection area but comes with the caveat that a small potential hill is created at the exit of the electric trap that can prevent the coldest molecules from leaving the trap due to the asymmetric voltages applied at the trap at the transition into the exit guide [Zep13, Pre18]. For symmetric guide voltages in first order it can be assumed that no electric field is created inside the LIF mirror by the quadrupole guide. Both contributions to the electric field, guide cap and quadrupole guide, lead to an electric field which is approximately pointing downwards as sketched in Figure 4.2. For a quantitative description of the electric field the setup is simulated in SIMION [Man08b] which employs a finite difference method to solve the Laplace equation. The calculation is performed by Maximilian Löw. From the simulation an approximate formula for the magnitude of the electric field at the position of the UV laser can be derived. The field is given by

$$E \approx aU_{\text{cap}} + bU_{\text{guide}}, \tag{4.1}$$

with the voltage applied to the cap U_{cap}, the voltage applied to the electric guide in asymmetric configuration U_{guide} and the two constants $a = 0.37\,\text{cm}^{-1}$ and $b = 8.2 \times 10^{-3}\,\text{cm}^{-1}$ which are determined by the simulation. This approximation is quite sensitive to the exact height of the laser beam through the LIF mirror, i.e. the distance to the guide cap. Also, the fact that the molecular beam spreads out (see Section 4.5.1) is not considered. This spread leads to slightly varying electric fields at different positions of the excitation volume. However, Equation (4.1) gives a good starting point when the magnitude of the electric field needs to be determined to e.g. measure UV spectra.

4.2.2 UV spectra

After understanding the electric fields within the detection volume the next step is to investigate the behaviour of the transition used for detection in the presence of such an electric field. This dependence on the electric field strength of the $\tilde{A}^1A_2 \leftarrow \tilde{X}^1A_1\ 4_0^1\ |2,2,0/1\rangle \leftarrow |3,3,0\rangle$ transition is shown in Figure 4.3(a). Only transitions starting from M-sublevels in the rotational state $|3,3,0\rangle$ which have a positive Stark shift ($|M|$=3, 2, 1), and therefore are populated in the electric trap and guide, are

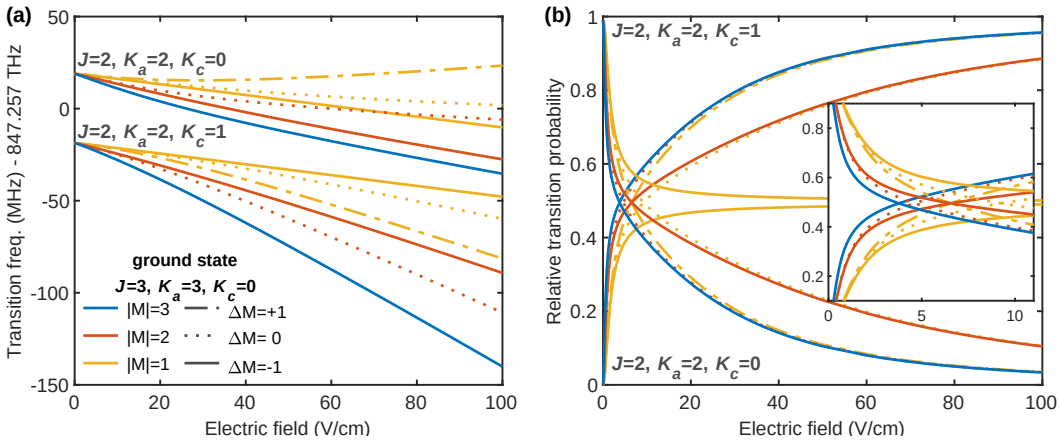

Figure 4.3: Stark map and transition probabilities for the transition $\tilde{A}^1A_2 \leftarrow \tilde{X}^1A_1$ 4_0^1 $|2,2,0/1\rangle \leftarrow |3,3,0\rangle$. The rotational M-sublevels in the electronic ground state are colour coded. The type of transition (ΔM=0, ±1) is indicated by the line style (solid, doted and dash-dot). **(a)** Calculated transition frequencies from the trapped rotational M-sublevels of the $|3,3,0\rangle$ state as given in the legend into the excited rotational states $|2,2,0/1\rangle$ are shown depending on the electric field. The determination of the offset transition frequency of 847.257 760 THz is described in the main text. In the electronic ground state a dipole moment of 2.3321 D is assumed [Fab77] and in the electronically excited state the dipole moment of 1.4566 D is taken from Section 4.2.3. **(b)** Relative transition probabilities for the transitions shown in **(a)**. The inset shows a magnification of the low electric field range.

shown. The curves are calculated using the treatment presented in Chapter 2, with the transition frequency determined later in this section and the dipole moment in the excited state taken from Section 4.2.3. Without the presence of an electric field the transitions into the upper state $|2,2,0\rangle$ of the rotational doublet in the electronically excited state are forbidden due to parity and transitions into the lower state of the doublet $|2,2,1\rangle$ are allowed as can be seen from the selection rules in Equation (2.10b) as well as from a calculation of the transition probabilities in Figure 4.3(b). With an electric field applied this is not the case anymore and for high electric fields the initially allowed transitions become forbidden and vice versa. For very small electric fields on the order of only a few $\frac{\mathrm{V}}{\mathrm{cm}}$ the transition probabilities change quickly as can be seen from the inset in Figure 4.3(b) which is due to mixing of parity states in the ground state where the $|3,3,0/1\rangle$ states have a splitting of only 0.65 MHz. In the excited state the splitting is 37.62 MHz which is the reason why higher electric fields are necessary to couple both states and the transition probability changes more slowly with the electric field.

To record a spectrum a fly-through measurement as described in Section 4.1 is performed. Contrary to the measurement presented there, for the spectrum no time dependence of the molecule signal is investigated but the voltages are continuously applied and a steady state arises as the molecule signal saturates. The fluorescence signal is then integrated for a certain amount of time before the frequency of the laser is adjusted for the next data point in order to measure a spectrum. Such a spectrum measured with symmetric voltages applied to the electric guide and no

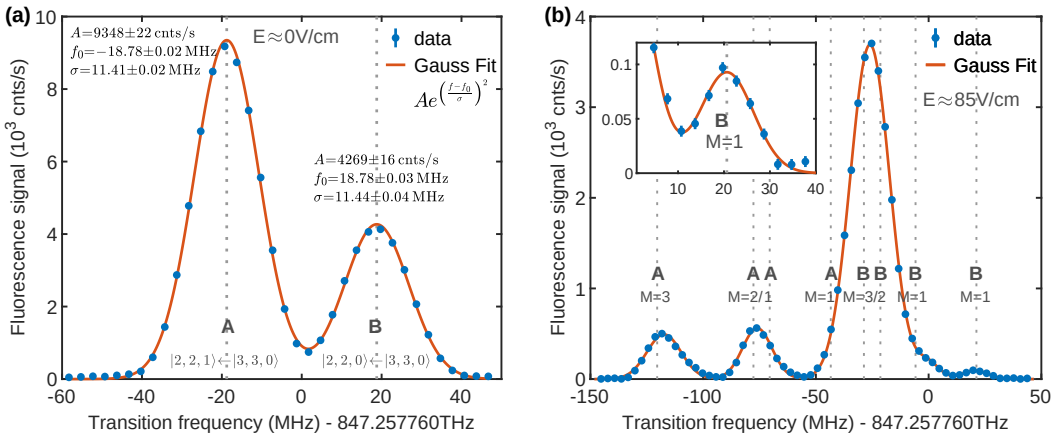

Figure 4.4: Measured spectra of the $\tilde{A}^1A_2 \leftarrow \tilde{X}^1A_1$ 4_0^1 $|2,2,0/1\rangle \leftarrow |3,3,0\rangle$ transition with and without electric field. Transitions are labelled A and B for the $|2,2,1\rangle \leftarrow |3,3,0\rangle$ and the $|2,2,0\rangle \leftarrow |3,3,0\rangle$ transition respectively. Grey dashed lines indicate the theoretical position of the various transitions between M-sublevels. Error bars represent the 1σ statistical error. **(a)** UV spectrum with U_{cap}=0 V and symmetric guide voltages of ±1.8 kV resulting in an electric field of approximately 0 $\frac{\mathrm{V}}{\mathrm{cm}}$. **(b)** UV spectrum with a voltage of U_{cap}=150 V and asymmetric electric guide voltages of 3.6/0 kV applied to the guide cap resulting in an electric field of about 85 $\frac{\mathrm{V}}{\mathrm{cm}}$. This leads to a splitting up of the otherwise degenerate transitions resulting in several peaks. The addressed rotational M-sublevels are labelled. The polarisation is chosen perpendicular to the electric field such that transitions with $\Delta M = \pm 1$ are driven.

offset voltage is presented in Figure 4.4(a).

The two peaks correspond to the two transitions at zero electric field shown in Figure 4.3(a), i.e. the rotational doublet in the electronically excited state consisting of $|2,2,0\rangle$ and $|2,2,1\rangle$. Each peak is a superposition of all possible transitions between the rotational M-sublevels which are degenerate in the absence of an electric field. The lines are fitted with a Gaussian model which allows the extraction of line position, width and signal height. Since the UV laser is referenced to an optical frequency comb the transition frequency can be determined precisely. The centre between the two lines lies at 847.257 760 THz[3] which deviates by about 500 MHz from a value to be found in the literature [Clo83]. The width of the transition is dominated by Doppler broadening. The measured width of 11.4 MHz corresponds to a temperature of 530 mK. The temperature of the molecules determined via a time of flight measurement [Pre12, Eng13] is considerably higher with 3.58 K corresponding to a mean velocity of $\bar{v} = 31.5\,\frac{\mathrm{m}}{\mathrm{s}}$ which would result in a Doppler width of about 29.6 MHz. The much smaller measured value is due to the fact that the UV laser is oriented perpendicular to the direction of the molecule beam. Since the outward bending of the exit of the guide reduces the velocity spread of the molecule beam and converts some of the transversal velocity into longitudinal velocity a smaller transversal temperature is measured in the detection region. Also, for a fly-through

[3]The error of frequencies measured with a laser locked onto the frequency comb in this work is on the order of 100 kHz. Since the UV laser used here is frequency tripled (refer Section 3.2) for values in the UV the error is on the order of 300 kHz.

measurement the longitudinal velocity of the molecules is generally higher than the transversal velocity.

The relative height of the peaks is determined by the transition probabilities shown in Figure 4.3(b) and the quantum yield of the excited state (see Section 4.3). Even though no voltage is applied to the guide cap and symmetric guide voltage are used, the transition to the $|2,2,0\rangle$ state has considerable strength despite being forbidden at zero electric field. This is due to the fact that Equation (4.1) is only an approximation and there still is a small electric field. As previously mentioned, for the parity doublet in the ground state only small electric fields are necessary to couple the states sufficiently so that transitions into both of the rotational states of the electronically excited states become possible.

Rotational M-sublevel selectivity In the presence of an electric field in the detection region the degeneracy of the M-sublevels is lifted as can be seen in the Stark map of Figure 4.3(a). In Figure 4.4(b) a spectrum of a fly-through measurement is shown with a voltage of U_{cap}=150 V applied to the guide cap and asymmetric guide voltages of 3.6/0 kV resulting in an electric field of about 85 $\frac{\mathrm{V}}{\mathrm{cm}}$ according to Equation (4.1). The laser polarisation is chosen perpendicular to the approximate direction of the electric field and the direction of propagation of the molecule beam, meaning that only transitions with $\Delta M = \pm 1$ are driven. Various peaks arise for the different transitions whose degeneracy is lifted by the electric field. The theoretical transition frequencies are indicated by the grey dashed lines and labelled with A and B for $|2,2,1\rangle \leftarrow |3,3,0\rangle$ and $|2,2,0\rangle \leftarrow |3,3,0\rangle$ respectively. Also the M-sublevel in the ground state before excitation by the UV laser is identified for each transition. Some transitions are still relatively close together at the chosen electric field strength so that they are not distinguishable but for M=3 and M=1 the peaks are already isolated so that the individual substates can be detected separately. By further increasing the electric field, sufficient separation between the lines can be achieved so that detection of each individual M-sublevel is possible. The magnitude of the signal for each peak observable in Figure 4.4(b) is, besides the transition probability and quantum yield, mainly influenced by the population of the ground state for each transition. M=3 has the highest Stark shift of the M-sublevels of the state $|3,3,0\rangle$ and as such has the best trapping properties and the highest population. Another important factor is the unloading voltage applied at the unloading electric quadrupole guide. Due to the different Stark shift the size of the exit hole is larger for molecules in lower M-sublevels which subsequently are unloaded less efficiently and comprise an even smaller portion of the molecules arriving at the detection setup.

The possibility to directly detect individual M-sublevels is a main improvement to previously employed techniques which relied on spectroscopically separating MW-transitions in the electric trap, a task which due to Stark broadening is hard to achieve [Glö16]. M-sublevel resolved detection is a powerful tool for the characterisation of e.g. the optoelectrical cooling scheme and Majorana flips in the electric trap. A further application is discussed in Section 6.4.

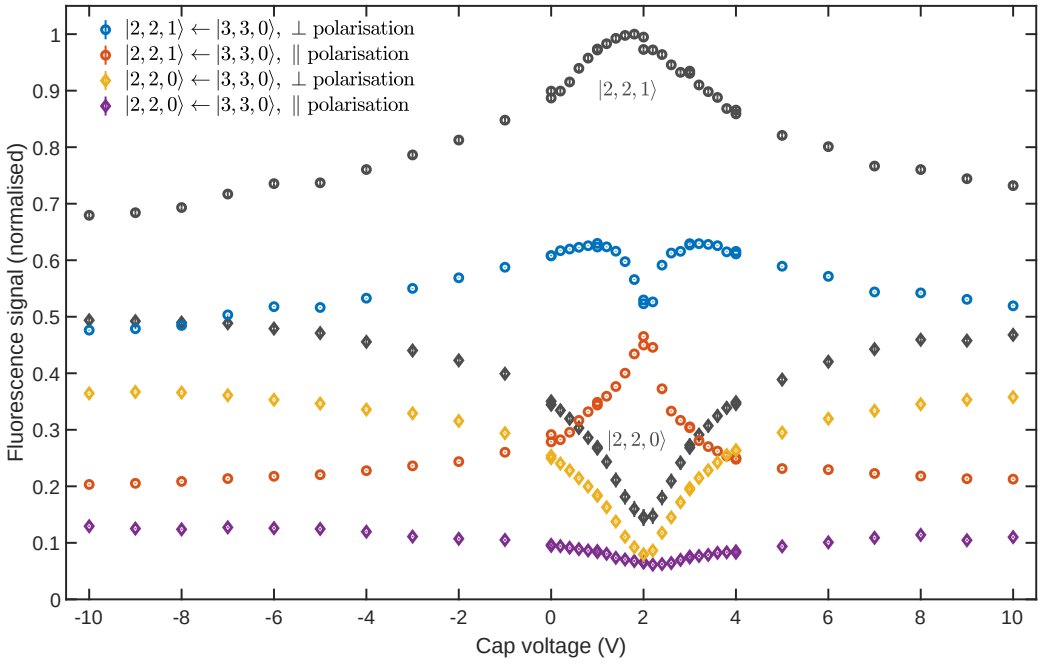

Figure 4.5: Dependence of the fluorescence signal on laser polarisation and electric field. Shown is the dependence of the height of the peak of the signal for the transitions $\tilde{A}^1A_2 \leftarrow \tilde{X}^1A_1\ 4_0^1\ |2,2,0/1\rangle \leftarrow |3,3,0\rangle$ (compare Figure 4.4(a)) on the electric field for laser polarisations parallel and perpendicular to the direction of propagation of the molecules in the detection region. At about 2 V the electric field vanishes leading to an increase and decrease in transition probability for polarisations oriented perpendicular and parallel to the electric field respectively. Additional feature appear due to a change in the direction of the electric field when the contribution from the electric guide and the guide cap start to cancel. The grey curves show the sum of the signal of both polarisations for the two transitions eliminating this additional feature. The overall shape is determined by the transitions probability and the quantum yield as explained in the main text.

Dependence on laser polarisation The UV laser light is polarised linearly. Depending on the orientation of the linear polarisation with regard to the direction of the electric field in the detection region either $\Delta M = \pm 1$ or $\Delta M = 0$ transitions are driven by the laser. As presented in Section 4.2.1 the direction of the electric field is oriented mainly in the vertical direction, meaning that for detection of molecules in the $M=3$ sublevel of the $|3,3,0\rangle$ rotational state via the $\tilde{A}^1A_2 \leftarrow \tilde{X}^1A_1\ 4_0^1\ |2,2,0/1\rangle \leftarrow |3,3,0\rangle$ transition the polarisation has to be perpendicular to the orientation of the electric field. This is the standard polarisation used throughout this work unless mentioned otherwise and also motivates the orientation of the vacuum windows under Brewster's angle mentioned in Section 3.3.4. A measurement of the dependence of the detected fluorescence signal on the polarisation and electric field is presented in Figure 4.5.

Plotted is the measured height of the two peaks shown in Figure 4.4(a), resulting from the transitions to the rotational states $|2,2,0/1\rangle$ in the electronically excited state with symmetric guide voltages of $U_{\text{guide}} = \pm 1.8\,\text{kV}$, for laser polarisations per-

pendicular and parallel to the direction of propagation of the molecules and therefore the electric field in the detection region. The electric field is varied by applying a small voltage to the guide cap. The range of $U_{\mathrm{cap}}=\pm 10\,\mathrm{V}$ corresponds to an electric field of about $\pm 3.7\,\frac{\mathrm{V}}{\mathrm{cm}}$ according to the approximate formula in Equation (4.1). The electric field is sufficient to bring the transition probabilities to about 0.5 from 1 and 0 respectively as can be seen from the inset in Figure 4.3(b). This becomes apparent in the increase and decrease of the signal for larger applied voltages. For the smallest fields, which occur around 2 V, a relatively sharp peak and dip can be seen in the signals for parallel and perpendicular polarisation of the $|2,2,1\rangle$ state respectively. The reason for this behaviour is that for very small voltages the direction of the electric field is not well defined anymore mixing the signal from $\Delta M=\pm 1$ and $\Delta M=0$ transitions. The fact that the centre is shifted to about 2 V is a sign for the presence of a small offset electric field even for symmetric guide voltages which is also confirmed by the electric field simulations. By summing up the signal of both polarisations for the two transitions an artificial 'total' signal can be constructed, consisting of the molecules detected from $M=3$ (perpendicular polarisation) and $M=2$ (parallel polarisation). Thus, polarisation effects are eliminated and smooth curves are obtained without additional features for low electric fields as can be seen from the curves in grey in Figure 4.5. The shape of the curve is determined by the change in transition probability. The difference between both summed up curves at higher voltages is explained by the about 40 % lower quantum yield of the $|2,2,0\rangle$ rotational state compared to the $|2,2,1\rangle$ state of the electronically excited state (see Section 4.3). For the $|2,2,0\rangle \leftarrow |3,3,0\rangle$ transitions the signal level never reaches zero which is due to the fact that the electric field is not completely homogeneous, and therefore never exactly zero for the whole excitation region. Due to the sensitivity of the transition probability to small electric fields this results in a non-zero signal for all applied voltage. The data in Figure 4.5 is stitched together from different data sets with slightly varying background levels causing a systematic bias of about 5 % which is not represented in the error bars. However, the general shape of the curves stays the same as the observed effects have a much bigger amplitude.

4.2.3 Doppler-free spectra

To further increase the resolution of UV spectra such as the ones shown in Figure 4.4 Doppler-free saturation measurements can be performed to eliminate Doppler broadening, the dominating broadening mechanism. To this end the laser is reflected back into itself instead of being dumped after passing through the vacuum chamber. In order to keep the increase in background stray light low, care has to be taken to match the spatial mode of incoming and outgoing laser beam. Measuring a spectrum with this setup leads to the occurrence of saturation dips in the spectrum as can be seen in Figure 4.6. Here, a UV spectrum of the transition $|2,2,0\rangle \leftarrow |3,3,0\rangle$ (denominated B as in Figure 4.4) is shown. The electric field is approximately $46\,\frac{\mathrm{V}}{\mathrm{cm}}$ leading to a splitting of the various lines for the rotational M-sublevels. The two grey dashed lines indicate the theoretical position of the transitions from the $M=3$ and $M=2$ state in the electronic ground state. Without a Doppler-free measurement the lines are not resolved as can be seen from the main peak in the spectrum

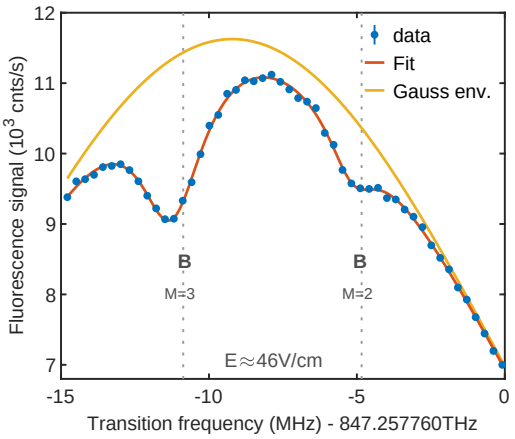

Figure 4.6: Doppler-free saturation spectrum of the transition $\tilde{A}^1A_2 \leftarrow \tilde{X}^1A_1\ 4_0^1\ |2,2,0\rangle \leftarrow |3,3,0\rangle$. Due to the applied electric field of approximately $46\,\mathrm{V\,cm^{-1}}$ the transitions between different M-sublevels are split up. The theoretical position of the transitions is indicated by the grey dashed lines. By retroreflecting the UV laser beam back into itself Doppler-free features appear in the Gaussian envelope allowing a precise determination of the line position by a Lorentzian fit.

displayed in Figure 4.4(b), which is even measured at a higher electric field, and therefore larger splitting between the lines. However, with the retroreflected laser beam two clear dips show up in the Doppler broadened profile allowing to resolve the individual transitions and precisely determining their position by fitting a Gaussian envelope overlaid with two Lorentzians. The main remaining broadening mechanism is power broadening which motivates the use of a Lorentzian lineshape for the fit.

The technique of Doppler-free saturation spectroscopy allows a much more precise determination of the line position than before, and therefore many of the transitions which could previously not be distinguished can be resolved. In Figure 4.7 the result of a measurement for many of the transitions between M-sublevels of the $\tilde{A}^1A_2 \leftarrow \tilde{X}^1A_1\ 4_0^1\ |2,2,0\rangle \leftarrow |3,3,0\rangle$ transition at different electric fields are summarised. The statistical error of the line position is quite small for most transitions with $\sigma_{\mathrm{stat}}{<}50\,\mathrm{kHz}$. More important are the systematic errors caused by an offset of the frequency stabilisation of the laser to the optical frequency comb due to spurious signals and small differences in the electric field due to realignment of the laser beam path through the vacuum chamber between measurements, which slightly affect the beam position. This amounts to a systematic error of about $\sigma_{\mathrm{syst}}{\approx}150\,\mathrm{kHz}$ in the line positions. The theory curves are fitted to the measured data with the dipole moment of the excited $\tilde{A}^1A_2\ 4^1$ state and the electric fields for each set of measurements as free parameters. This results in a value of

$$\mu = 1.4566 \pm 0.0003_{\mathrm{stat}} \pm 0.0043_{\mathrm{syst}}\,\mathrm{D} \tag{4.2}$$

for the electric dipole moment of the excited state. In the literature two values can be found for the dipole moment. In Ref. [Fre66] $\mu{=}(1.56 \pm 0.07)\,\mathrm{D}$ is stated which deviates by about $1.5\,\sigma$ from the result of this work. In Ref. [Vac89] values for individual rotational states with J=2 are determined. They are obtained by

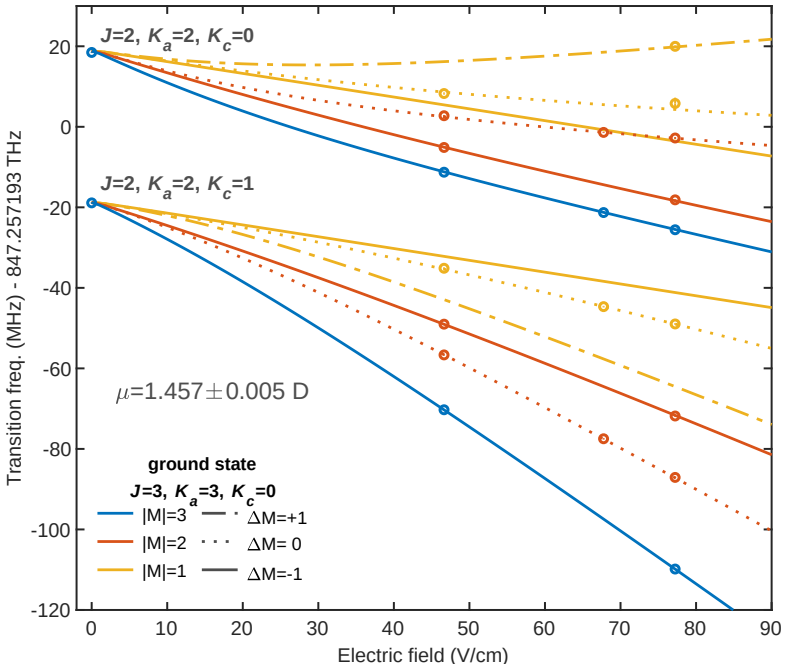

Figure 4.7: Stark map of the $\tilde{A}^1A_2 \leftarrow \tilde{X}^1A_1$ 4_0^1 $|2,2,0/1\rangle \leftarrow |3,3,0\rangle$ transition. The measured data points are obtained by Doppler free saturation spectroscopy. Each set of data points is measured with the same voltage configuration. The corresponding electric fields are fitted together with the dipole moment of the excited state as free parameters resulting in a value of $\mu = 1.4466 \pm 0.0003_{\text{stat}} \pm 0.0043_{\text{syst}}$ D.

quantum beat spectroscopy of the decay of excited states with different M quantum number which should make the measurement independent of the dipole moment of the ground state. For the $|2,2,0\rangle$ state a value of μ=(1.4526 ± 0.0004) D is given and for the $|2,2,1\rangle$ state a value of μ=(1.4538 ± 0.0004) D. This is consistent within the error bar with the value obtained here, where it is not possible to resolve any differences between the two rotational states with the current precision. For the dipole moment of the ground state a value of (2.3321 ± 0.0005) D is used in the calculation which is taken from Ref. [Fab77].

Power broadening As mentioned previously the main remaining broadening mechanism is power broadening. To investigate this fact the laser power used for a Doppler-free spectrum can simply be reduced. In Figure 4.8 the dependence of the width of the Doppler-free feature on the laser power is plotted. The spectra are taken at about zero electric field in the detection region on the $\tilde{A}^1A_2 \leftarrow \tilde{X}^1A_1$ 4_0^1 $|2,2,1\rangle \leftarrow |3,3,0\rangle$ transition. As the laser power is decreased the width of the transition decreases correspondingly. The curve can be fitted by a simple power broadening model of a two-level system [Sie86] which qualitatively shows good agreement and yields a linewidth of (1.00 ± 0.03) MHz at zero laser power. This value is still considerably broadened by residual Stark broadening due to the electric fields still present in the detection region even with symmetric voltages applied to the electric guide

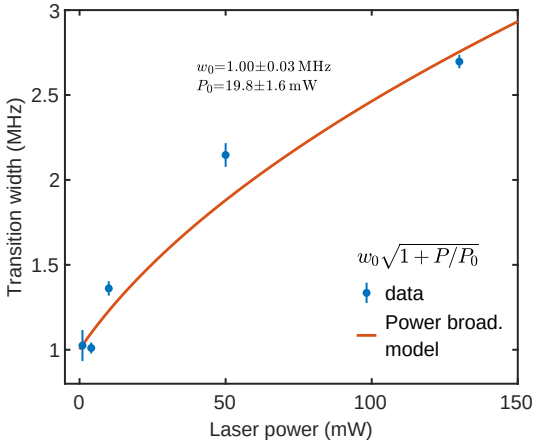

Figure 4.8: Power broadening of the $\tilde{A}^1A_2 \leftarrow \tilde{X}^1A_1$ 4_0^1 $|2,2,1\rangle \leftarrow |3,3,0\rangle$ transition. With approximately $0\,\mathrm{V\,cm^{-1}}$ in the detection region the UV laser power is varied. The result is fitted with a simple power broadening model of a two-level system [Sie86]. The remaining width of $(1.00 \pm 0.03)\,\mathrm{MHz}$ is a combination of the laser linewidth and residual Stark broadening.

and zero Volt at the guide cap. From simulations the remaining Stark broadening can be expected to be on the order of a few hundreds of kHz which is about the same size as the natural linewidth. Therefore, the measured value can only put an upper bound onto the laser linewidth which is specified to be <300 kHz but comes with the caveat that a detailed description regarding the definition is not provided with the specification.

4.3 Excited state lifetime and quantum yield

An important characteristic of the detection scheme directly affecting the detection efficiency is the quantum yield, i.e. the average number of photons emitted per excited molecule. As discussed in Section 3.1 the fluorescence lifetime of the excited state τ_{fl} is closely related to the quantum yield of the decay via $\Phi = \frac{\tau_{\mathrm{fl}}}{\tau_{\mathrm{rad}}}$ with the radiative lifetime τ_{rad}. In this section a measurement of the fluorescence lifetime for a selection of rotational states of the $\tilde{A}^1A_2$ 4^1 state is presented and the corresponding quantum yield deduced.

Laser switching setup and measurement principle To measure the spontaneous decay of the electronically excited state the UV laser has to be switched off on a time scale much shorter than the lifetime of the state. From previous measurements in the thesis of Erich Dobler it is known that the lifetime is on the order of 1 µs or less [Dob16]. For switching off the laser a rather simple setup is chosen: Before the beam cleaning setup (see Section 3.3.2) the laser is sent through an electro-optic modulator (EOM). By applying a voltage to the crystal of the EOM it becomes birefringent such that the laser polarisation is turned by 90°. By using a polariser in the appropriate orientation the laser can be turned off on a rather short time

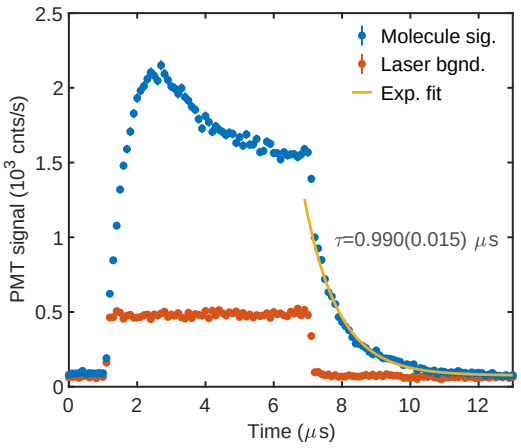

Figure 4.9: Fluorescence lifetime of the $\tilde{A}^1A_2$ 4^1 $|2,0,2\rangle$ state. In red the switching of the laser is visible via the change in background counts caused by the laser. Switching happens on a time scale of about 50 ns and with an extinction ratio of about 250 : 1 via an EOM. In blue the fluorescence signal is shown (including laser background) which after an initial peak caused by a surplus of unexcited molecules decays towards a steady state value. When the laser is turned off a fluorescence decay time of τ_{fl}=(0.990 ± 0.015) µs can be determined with an exponential fit.

scale of about 50 ns. The measurement sequence is rather similar to the one used for taking UV spectra in the last section. Electric guides and electric trap are operated in fly-through mode and the molecules continuously enter the detection region. The difference to previous measurements is that the UV laser is pulsed and the time dependence of the PMT signal is examined instead of the integrated signal. An exemplary measurement for the fluorescence lifetime of the $|2,0,2\rangle$ rotational state in the $\tilde{A}^1A_2$ 4^1 vibronic state is presented in Figure 4.9. Shown in red is the background signal caused by the UV laser, i.e. a measurement without molecules. The signal rises and drops steeply when the laser is turned on and off respectively. The remaining signal when the laser is turned off is mostly caused by the dark counts of the PMT. However, with the EOM only a finite on : off extinction ratio of about 250 : 1 is achieved meaning that also some laser background is contributing to the signal. The signal in blue shows the PMT signal when molecules are added. When the laser is turned on the signal quickly rises as the molecules in the detection region are excited and start to fluoresce. After an initial peak the signal approaches a lower steady-state value which is determined by the rate with which new molecules enter the detection region. The decay is governed by the fluorescence lifetime, however, a much cleaner measurement is possible after the laser is switched off. The fluorescence signal of the molecules persists but decays exponentially. This decay is given by the lifetime of the excited state and in this case yields a fluorescence lifetime of τ_{fl}=(0.990 ± 0.015) µs. The influence of the laser switching is negligible as long as the fluorescence decay is much longer than the switching time. It only becomes important for decay times on the same time scale, where thus only an upper limit can be found. Fluorescence decay times are measured for a variety of states. A summary of the measured decay times is provided in Table 4.3. In the first column

the rotational state of the electronically excited state $\tilde{A}^1A_2\ 4^1$ and in the second column the corresponding decay time is listed. The data is compared to values that can be found in the literature. In Ref. [Wei80] fluorescence lifetimes were measured in a gas cell at pressures of about $0.1\,\mathrm{mTorr} - 1\,\mathrm{mTorr}$, causing collisional perturbation on the order or 10 %. The values mostly agree within the error bar except for those values that are limited by the time resolution due to the laser switching time as mentioned before. In Ref. [Hen82] the lifetimes were measured in a jet experiment which is claimed to be nearly collision free even though pressures are still quoted as 0.1 mTorr. The values given here don't nearly agree as well, however, the experiment had a much lower resolution and no error bars are given. In Ref. [Vac88] polarisation transient gain spectroscopy was performed enabling the elimination of collisional effects. Only one state coincides with the states investigated in this work and the values disagree by only a bit more than $1\,\sigma$. The huge variations in lifetimes of different rotational states is attributed to the coupling of the excited state to a 'lumpy' continuum. That means that some states strongly couple to other rotational states in the electronic ground state leading to an increased non-radiative decay whereas others do not [Wei80, Moo83].

Resulting quantum yield In principle detailed knowledge about the interaction of the electronic ground and excited state is necessary to determine the quantum yield, in particular the non-radiative decay channels such as dissociation and internal conversion via conical potential energy surface intersections. This is a quite difficult task and still subject to research in recent times [Ara08, Ian13]. A more tractable approach is the assumption that the longest fluorescence decay time for states with low J and K quantum numbers are already the pure radiative lifetime and that there is no contribution from a non-radiative component. This is a commonly accepted approach in literature, that is considered reasonable as there is no experimental indication otherwise [Wei79, Wei80, Hen82] and it is also backed by theoretical considerations [vD78].

The longest fluorescence lifetime measured in this work is the one of the rotational states $|0,0,0\rangle$ and $|1,1,1\rangle$. They only differ by a few percent which is why for the radiative lifetime their average is taken. Knowing the radiative lifetime the quantum yield can easily be calculated with the relation $\Phi = \frac{\tau_{\mathrm{fl}}}{\tau_{\mathrm{rad}}}$. The result is summarised in the third column of Table 4.3. In the literature only one source for absolute pressure free quantum yields for the $\tilde{A}^1A_2\ 4^1$ state can be found in Ref. [Shi81] and the accompanying paper Ref. [Fai81]. Here, the molecule D_2CO which is not subject to such huge variations in the fluorescence lifetime was used as a reference. Furthermore, the number of absorbed and emitted photons is measured for varying pressures ranging from $120\,\mathrm{mTorr} - 5\,\mathrm{mTorr}$ which means that the quantum yield had to be extrapolated to obtain a zero pressure value. The results are shown in the last column of Table 4.3. The agreement with the values determined in this thesis work is poor, however: Due to the complicated process with several intermediate steps to determine the quantum yield at zero pressure in Ref. [Fai81] a systematic error of about 30 % is stated. The values obtained in this thesis work should not contain relevant systematic effects for lifetimes much longer than the laser switching time. Collisions don't influence the measurement because even for a pessimistic

	Data		Literature			
Rot. state $\tilde{A}^1A_2\ 4_0^1$	Lifetime	Quantum yield	Ref. [Wei80]	Ref. [Hen82]	Ref. [Vac88]	Ref. [Shi81]
$\lvert J, K_a, K_c\rangle$	τ (μs)	Φ (%)	τ (μs)	τ (μs)	τ (μs)	Φ (%)
$\lvert 0,0,0\rangle$	3.18 ± 0.04	97 ± 2	3.10 ± 0.16	4.67	-	-
$\lvert 1,1,1\rangle$	3.37 ± 0.03	103 ± 2	-	2.65	-	-
$\lvert 1,0,1\rangle$	2.76 ± 0.01	84 ± 1	2.76 ± 0.14	2.8	-	-
$\lvert 2,2,0\rangle$	0.615 ± 0.003	18.8 ± 0.3	0.69 ± 0.03	0.89	-	32.2 ± 2.1
$\lvert 2,2,1\rangle$	0.995 ± 0.003	30.4 ± 0.4	-		-	-
$\lvert 2,1,2\rangle$	0.573 ± 0.007	17.5 ± 0.3	-	0.63	-	-
$\lvert 2,0,2\rangle$	0.990 ± 0.015	30.2 ± 0.6	0.86 ± 0.04	0.88	0.85 ± 0.10	-
$\lvert 3,3,0/1\rangle$	0.188 ± 0.010	5.7 ± 0.3	-	-	-	-
$\lvert 3,2,2\rangle$	0.188 ± 0.002	5.8 ± 0.1	-	-	-	6.8 ± 0.6
$\lvert 4,4,0/1\rangle$	0.042 ± 0.002	1.3 ± 0.1	0.025 ± 0.001	-	-	0.75 ± 0.14
$\lvert 4,3,2\rangle$	0.16 ± 0.05	4.9 ± 1.6	-	-	-	-
$\lvert 4,2,3\rangle$	0.459 ± 0.006	14.0 ± 0.3	0.49 ± 0.02	0.86	-	20 ± 2
$\lvert 5,4,2\rangle$	0.132 ± 0.004	4.0 ± 0.1	0.113 ± 0.006	-	-	3.03 ± 0.57

Table 4.1: Summary of measured fluorescence lifetime in the $\tilde{A}^1A_2\ 4^1$ state and comparison with literature values. Lifetimes are measured by switching the excitation laser with an EOM on a time scale of 50 ns. The quantum yield is calculated by taking the longest lifetimes of the $|0,0,0\rangle$ and the $|1,1,1\rangle$ state as the radiative lifetime (see main text). Note that all values from literature except from Ref. [Vac88] are subject to considerable systematic errors due to collisional quenching. In particular for the quantum yield of Ref. [Shi81] an additional systematic error of about 30 % is stated.

estimate the peak pressure in the molecule beam is $<1 \times 10^{-8}$ mbar and thus many orders of magnitude lower than for the measurements given in the literature. The transition time through the detection area also only has a negligible contribution, as the detection efficiency of the LIF mirror does not significantly change over the distance the molecules can travel during the fluorescence decay.

Most relevant for this work is the quantum yield of the decay of the states $|2, 2, 0/1\rangle$ as those are the states used for the detection of molecules after completing the optoelectrical Sisyphus cooling cycle and the state $|1, 0, 1\rangle$ which is used for the detection of molecules in the experiments presented in Chapter 5 and Chapter 6. As can be seen from Table 4.3 the state $|2, 2, 1\rangle$ has a higher quantum yield with $(30.4 \pm 0.4)\,\%$ than the state $|2, 2, 0\rangle$ which only has a quantum yield of $(18.8 \pm 0.3)\,\%$. This means that it is favourable to detect the molecules via the lower state $|2, 2, 1\rangle$ of the doublet in combination with low electric fields due to the influence of the transition probability shown in Figure 4.3.

4.4 Detection of cold molecules

The LIF detection scheme has various advantages over the detection with a QMS as is already mentioned in Chapter 3. One advantage, that only applies to very cold molecules below a certain temperature threshold, is highlighted in this section. To reach these temperatures close to 1 mK optoelectrical Sisyphus cooling is employed. The cooling sequence for formaldehyde is presented in great detail in the thesis of Alexander Prehn [Pre18]. Here, only a short summary is given.

Formaldehyde molecules are continuously loaded into the electric trap for 18 s. During this time optoelectrical Sisyphus cooling is already being performed, meaning that RF is applied to induce transitions between strongly and more weakly trapped states, the IR laser is shone into the trap for vibrational excitation of the molecules, and MW are used for repumping, as described in Section 2.2.1. The RF is already cycled from higher to lower frequencies in order to cool initially hot molecules with a short trap lifetime to temperatures where they have a longer lifetime and can therefore participate in the following cooling steps. After the loading sequence, cooling continues without further loading of uncooled molecules for 12 s where the RF applied for cooling is lowered stepwise down to a frequency of $f_{\mathrm{RF}} - f_{\mathrm{offset}} = (308 - 184)\,\mathrm{MHz} = 124\,\mathrm{MHz}$. This results in a molecular sample of 17 mK and 13 mK in the case of a measurement with LIF detection and the previously employed QMS respectively. Naturally, the temperature of the molecules does not depend on the type of detection used. The difference between the two values is explained by the fact that many parameters of the cooling sequence changed as one was measured with the previously employed setup with a QMS and for the other many changes were implemented for the new LIF detection scheme requiring reoptimisation of the cooling sequence. After the cooling sequence the molecules are brought to a single rotational sublevel $|J, K_a, K_c, M\rangle = |3, 3, 0, 3\rangle$ via optical pumping. Details about the optical pumping scheme are provided in the thesis of Rosa Glöckner [Glö16]. After this single state preparation the molecules are unloaded from the trap for 12 s and guided to the detection area. In the case of detection via

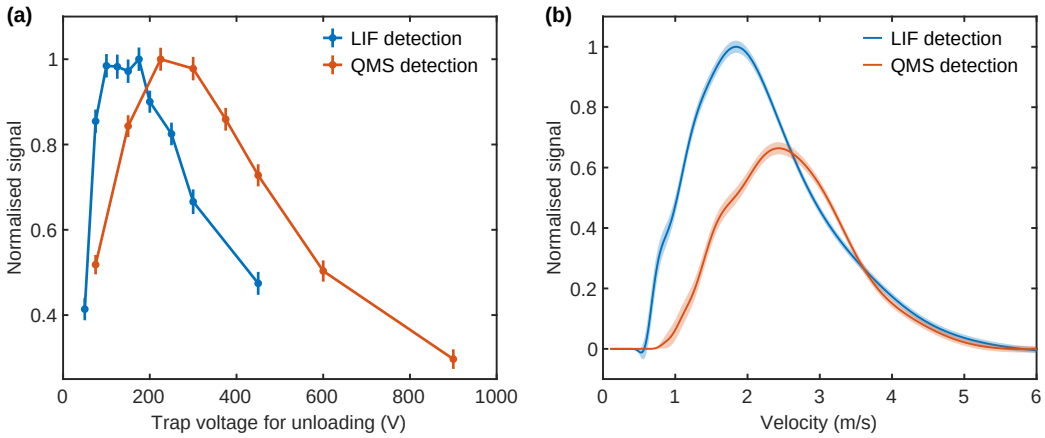

Figure 4.10: Comparison of detection properties for cold molecules with QMS and LIF detection. A sample of cold molecules, with a temperature of 13 mK and 17 mK for QMS and LIF detection respectively, is prepared by optoelectrical Sisyphus cooling. The signal is integrated over 12 s of unloading time. **(a)** The voltage applied at the trap and the quadrupole guide during unloading is varied. For a detection via LIF the maximum is shifted significantly towards lower voltages meaning that colder molecules are unloaded more efficiently. **(b)** Velocity distributions are reconstructed from the rising edge of a time-of-flight measurement. The curves are matched via the high velocity part with $>3\,\frac{\mathrm{m}}{\mathrm{s}}$. By detection via a QMS a significant part of the lower end of the velocity distribution is missing. The shaded areas indicate the statistical error.

LIF the UV laser is then set to the peak of the $\tilde{A}^1A_2 \leftarrow \tilde{X}^1A_1\ 4_0^1\ |2,2,1\rangle \leftarrow |3,3,0\rangle$ transition and the transition is broadened with electric fields in such a manner that all molecules in the Doppler broadened transition are addressed (for details see Section 4.5). For both detection methods, QMS and LIF, the signal is integrated over the unloading time.

The unloading efficiency of the molecules from the trap is sensitive to the voltage applied at the unloading guide. The electric fields inside the trap and the quadrupole guide have to be matched. Low voltages, i.e. weak electric fields, create high losses for faster molecules which aren't confined anymore whereas high voltages (strong electric fields) result in slow and inefficient unloading as the exit hole of the trap becomes smaller. The molecules decay exponentially out of the trap via the unloading guide with a time constant determined by the size of the exit hole[4]. For further details about the unloading process the reader is referred to Ref. [Pre18]. In Figure 4.10(a) a measurement is presented where the unloading voltage applied to the trap and the guide is varied for both cases, with the old detection scheme with a QMS and with the new detection scheme based on LIF. Both curves are normalised to their individual maxima. It can be seen that the optimal voltage for unloading is shifted considerably towards lower voltages. This is attributed to the fact that with the QMS the coldest molecules can not be detected due to the electric fields deflecting the molecules before they can enter the ionisation volume (see Ref. [Pre18] for details).

[4]The unloading time of 12 s is long enough so that the error due to integration up to different values in decay constant is negligible and all signal is captured.

For the new detection scheme no such limitation is to be expected because the electric fields are much smaller, so that already gravity would be sufficient to overcome any potential barrier. Therefore, colder molecules are detected meaning that a higher signal level is achieved for lower voltages where cold molecules are unloaded more efficiently.

A second measurement supporting the claim of a more efficient unloading of cold molecules is shown in Figure 4.10(b). Here, velocity distributions are depicted for the same molecule samples as described in the last paragraph, i.e. samples at a temperature of 17 mK and 13 mK for QMS and LIF detection respectively. The velocity distribution are reproduced from a rising edge measured with a time-of-flight measurement as is explained in detail in Ref. [Pre12]. Since signal levels are different in both measurements and less slow molecules are expected in the case of detection with the QMS, the curves are matched to each other using the high velocity end of the distribution with velocities $>3\,\frac{\mathrm{m}}{\mathrm{s}}$ which is roughly the point up to which both distributions have a similar shape. It is immediately apparent that the distribution measured with the QMS, despite its lower temperature of 13 mK, that has been measured by a RF knife edge filter measurement within the trap (see Ref. [Pre18]), is lacking the low velocity end of the distribution. Already between $2\,\frac{\mathrm{m}}{\mathrm{s}}$ and $1\,\frac{\mathrm{m}}{\mathrm{s}}$ there is a significantly smaller fraction of molecules in the distribution. Below $1\,\frac{\mathrm{m}}{\mathrm{s}}$ there are no molecules at all which is also true for samples cooled to much lower temperatures, where instead only the measured signal decreases, which required parametric heating of the molecules for detection in the past [Pre18].

Both measurements presented in this section show that the new detection scheme based on LIF liberates the experiment from the particular disadvantage of the QMS of not being able to directly detect cold molecules below a certain velocity threshold.

4.5 Detection efficiency

In this section the detection efficiency is determined which allows a calibration of the detection scheme in terms of absolute molecule numbers. To this end, at first laser power saturation measurements are presented in Section 4.5.1 to determine the maximum signal theoretically achievable with infinite laser power where all molecules would be excited. Afterwards, experimental losses caused by the detection setup are discussed in Section 4.5.2 before determining the overall detection efficiency and hence the number of molecules in Section 4.5.3.

4.5.1 Saturation with laser power

To investigate the increase of fluorescence signal with higher laser power and the saturation properties of the molecule signal a simple model is introduced. The molecule beam is modelled to have a number density n with a Gaussian profile in both real (one dimensional) space y and frequency space ν:

$$n\left(y,\nu\right) = n_0 \exp\left(-\frac{y^2}{w_{\mathrm{mol}}^2} - \frac{\nu^2}{\Delta\nu_{\mathrm{D}}^2}\right), \tag{4.3}$$

with the corresponding width parameters w_{mol} and $\Delta\nu_{\mathrm{D}}$ respectively and the maximum density n_0. The laser beam is described in a similar fashion, with the beam width w_{las} in real space and the linewidth $\Delta\nu_{\mathrm{las}}$ in frequency space such that the spectral and spatial power density p is given by:

$$p\left(y,\nu\right) \propto \exp\left(-2\frac{y^2}{w_{\mathrm{las}}^2}\right)\exp\left(-\frac{\nu^2}{\Delta\nu_{\mathrm{las}}^2\left(1+\frac{P}{P_{\mathrm{broad}}}\right)}\right). \tag{4.4}$$

In the second part of Equation (4.4) power broadening is considered with the total laser power P and a broadening factor P_{broad}. The saturation behaviour of the number of excited molecules with laser power N can then be modelled as follows [Sie86]:

$$N\left(P\right) = \iint n\left(y,\nu\right)\exp\left[-\frac{P}{P_{\mathrm{sat}}}p\left(y,\nu\right)\right]\mathrm{d}y\mathrm{d}\nu, \tag{4.5}$$

with the total number of molecules N_0 and the saturation power P_{sat}. Combining Equation (4.3), Equation (4.4), and Equation (4.5) this results in the following expression for the measured signal S in terms of the laser power P:

$$S = S_{\mathrm{max}}\cdot\left[1-\frac{\iint\exp\left(-\frac{y^2}{w_{\mathrm{mol}}^2}-\frac{\nu^2}{\Delta\nu_{\mathrm{D}}^2}\right)\exp\left[-\frac{P}{P_{\mathrm{sat}}}\exp\left(-2\frac{y^2}{w_{\mathrm{las}}^2}\right)\exp\left(-\frac{\nu^2}{\Delta\nu_{\mathrm{las}}^2\left(1+\frac{P}{P_{\mathrm{broad}}}\right)}\right)\right]\mathrm{d}y\mathrm{d}\nu}{\iint\exp\left(-\frac{y^2}{w_{\mathrm{mol}}^2}-\frac{\nu^2}{\Delta\nu_{\mathrm{D}}^2}\right)\mathrm{d}y\mathrm{d}\nu}\right], \tag{4.6}$$

with the maximum signal for infinite laser power S_{max}. The spatial dimension y is chosen perpendicular to the direction of beam propagation for laser and molecule beam. The first term in the integral of the numerator corresponds to Equation (4.3) and describes the molecule beam in real and frequency space as Gaussian distributions. The second term corresponds to Equation (4.4) and accounts for spatial and spectral hole burning. The integral in the denominator provides normalisation.

In order to apply the model, the parameters describing the molecule beam and the laser beam have to be determined. The laser beam width is easily measured outside of the vacuum chamber and by fitting the envelope of a Gaussian laser beam, a beam width in the horizontal direction of w_{las}=2.3 mm is deduced. The spectral width of the laser, or rather the spectral width of the molecule transition addressed by the laser without additional broadening is determined in Section 4.2.2 with Doppler free saturation spectroscopy to be $\Delta\nu_{\mathrm{L}}=(1.00\pm0.03)$ MHz.

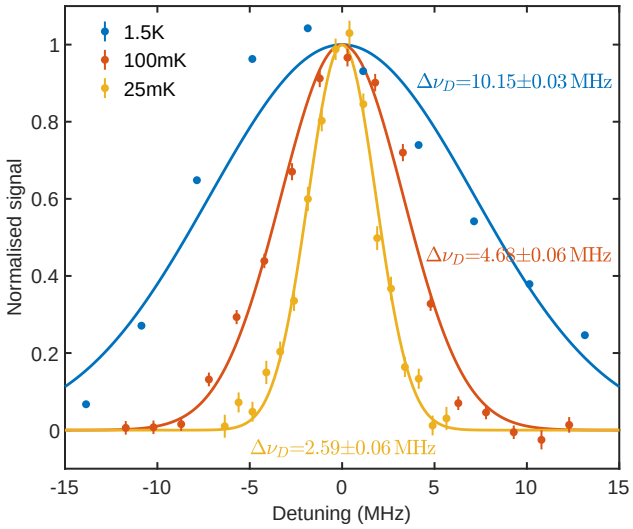

Figure 4.11: Doppler width of the $\tilde{A}^1A_2 \leftarrow \tilde{X}^1A_1$ 4_0^1 $|2,2,1\rangle \leftarrow |3,3,0\rangle$ transition for three different temperatures. Solid lines are fits of Gaussian profiles to the individual data sets. The resulting $1/e$ width $\Delta\nu_\mathrm{D}$ is plotted for each curve. Error bars are the 1σ statistical error. The curve at 1.5 K is measured in a fly-through measurement. The asymmetric voltages cause non-negligible Stark broadening resulting in an asymmetric lineshape. The molecules for the curves at 100 mK and 25 mK are cooled to a final cooling frequency of $f_\mathrm{RF}-f_\mathrm{offset}=(1258-184)$ MHz and $f_\mathrm{RF}-f_\mathrm{offset}=(375-184)$ MHz respectively.

Spectral width of the transition and laser broadening techniques The spectral width of the transition depends on the temperature of the molecules due to Doppler broadening being the dominating broadening mechanism. The width can easily be determined by UV spectroscopy as described previously in Section 4.2.2. In Figure 4.11(a) measurements of the Doppler width of the detection transition for three different molecule temperatures is presented. The first sample are uncooled molecules in a fly-through measurements (see Section 4.2.1) with a temperature of 1.5 K. The lineshape is rather asymmetric and does not have a nice Gaussian profile due to asymmetric quadrupole guide voltages of 4 kV/0 V which create an electric field in the detection region. This field is compensated by applying a negative voltage at the guide cap resulting in inhomogeneous residual electric fields in the detection region leading to further Stark broadening causing the asymmetric lineshape. Fitting of a Gaussian profile is of course accompanied by a considerable systematic error due to the deviation of the lineshape, nonetheless a width of about $\Delta\nu_\mathrm{D}$=10 MHz is determined. The remaining two curves shown in Figure 4.11 are measured with cold molecules cooled to a final cooling frequency of $f_\mathrm{RF}-f_\mathrm{offset}=(1258-184)$ MHz and $f_\mathrm{RF}-f_\mathrm{offset}=(375-184)$ MHz resulting in temperatures of about 100 mK and 25 mK respectively. Stark broadening is not an issue anymore as the unloading voltages are much lower for colder molecules. The Doppler width decreases as expected resulting in widths of $\Delta\nu_\mathrm{D}=(4.68\pm0.06)$ MHz for the hotter and $\Delta\nu_\mathrm{D}=(2.59\pm0.06)$ MHz for the colder sample.

For all three different temperatures investigated, the spectral width is much larger

than the laser linewidth. In order to address all molecules two different techniques are employed in the course of this thesis work. A simple method is to shift the centre frequency of the transition by applying an electric field such that the laser can address molecules of different velocity classes. If this shift happens on a timescale faster than the transit time of the molecules through the laser beam and covers the full spectral width of the transition, the whole molecule beam can be addressed. For uncooled molecules with a velocity of 15 $\frac{\mathrm{m}}{\mathrm{s}}$ this corresponds to a frequency of at least 75 kHz due to the laser focus in the direction of molecules propagation of about 200 µm. The amplitude of the applied voltage ramp needed to cover the full spectral width of the transition varies for different temperatures and rotational states. For uncooled molecules with a Doppler width of about 10 MHz as shown in Figure 4.11, when there is no offset electric field present, voltages as high as ±30 V are necessary. For colder molecules this value is smaller depending on the Stark shift and the frequency width to be covered. Of course, this technique heavily relies on a sizeable Stark shift of the molecules and has to be adjusted for each individual state. In order to avoid this problem the laser itself can also be frequency broadened. To do so, the laser is sent through an EOM acting on the phase of the laser beam creating sidebands. By choosing the right modulation frequency and voltage the laser linewidth can be broadened to cover the full spectral width of the molecule transition. This technique is independent of the molecular state and its Stark shift. However, the modulation still has to be adjusted for every temperature due to the different Doppler widths.

Width of the molecule beam The spatial size of the molecule beam in the detection area after leaving the electric quadrupole guide can easily be measured by adjusting the focus of the laser beam. Instead of using a laser beam only focussed in the vertical direction and collimated in the horizontal direction the beam is focussed in both dimensions with a focus of size w_0=200 µm at the position of the molecule beam. Translating the laser in the horizontal direction allows probing the spatial dimension of the molecule beam. The result of such a measurement for molecules in fly-through configuration is presented in Figure 4.12. As expected the signal decreases when moving the focused laser from the centre position and a Gaussian shape with width $w_{\mathrm{mol}} = (2.21 \pm 0.03)$ mm can be fitted quite well. The measurement is performed with molecules with a mean velocity of $(12.8 \pm 0.2)\,\frac{\mathrm{m}}{\mathrm{s}}$ corresponding to a temperature of about 590 mK. For the limiting case of molecules with zero initial velocity the downward bend of the guide into the detection area increases the velocity by about 1.7 $\frac{\mathrm{m}}{\mathrm{s}}$. Therefore, the influence of gravity can be neglected for the investigated velocities. Since the guide voltage is roughly proportional to the energy of the molecules the change of the molecule beam size due to spreading out after leaving the guide [Mie10] with temperature is estimated to be small and introduces a systematic error <10 %.

Saturation With the knowledge about the spectral width of the molecule transition and spatial width of the molecule beam, the model from Equation (4.6) can be applied. A measurement of saturation curves for three different temperatures is presented in Figure 4.13(a)-(c). For each temperature a measurement without

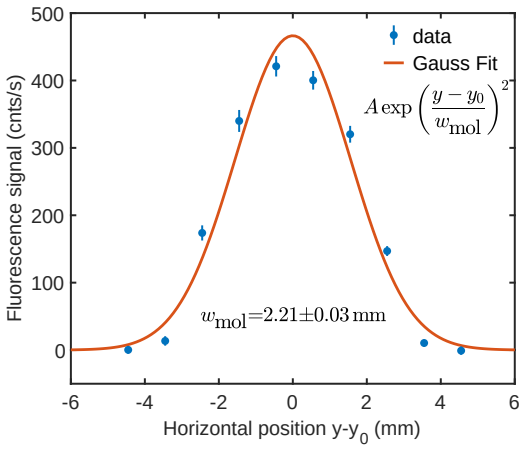

Figure 4.12: Measurement of the shape of the molecule beam. The UV laser is focused into the detection area with a waist of w_0=200 µm and its horizontal position varied. The fluorescence signal of molecules in fly-through configuration is recorded revealing a roughly Gaussian shape of the molecule beam.

a broadened laser and one with a broadened laser or shifting of the transition is shown. For 1.5 K and 100 mK an EOM is used, for the measurements at 25 mK the transition is shifted via a voltage ramp. The solid curves are fitted to the data using the model in Equation (4.6) with the constants as given in the last paragraphs, the molecules beam width w_{mol}=(2.21 ± 0.03) mm, the Doppler width for the three different temperatures $\Delta\nu_{\mathrm{D1}}$=(10.15 ± 0.03) MHz, $\Delta\nu_{\mathrm{D2}}$=(4.68 ± 0.06) MHz and $\Delta\nu_{\mathrm{D2}}$=(2.59 ± 0.06) MHz, the laser beam width w_{las}=2.3 mm, and the laser linewidth $\Delta\nu_{\mathrm{las}}$=(1.00 ± 0.03) MHz for the unbroadened case. For the broadened laser complete coverage of the spectral line is assumed. The free parameters of the fit are P_{sat}, P_{broad} and S_{max}. The resulting extrapolated signal S_{max} and the saturation laser power P_{sat} are given in each panel for both curves. The maximum signal decreases for lower temperature as is to be expected due to losses during cooling. It is important to note that only molecules in the rotational state $|3,3,0\rangle$ are detected. Hence for uncooled molecules only a subset of molecules of about 15 % of all molecules is detected [Pre18]. For the measurements at 100 mK about half of the molecules are detected because only molecules in the states $|3,3,0\rangle$ and $|4,3,1\rangle$ are addressed by the optoelectrical cooling cycle and have a lifetime long enough to survive until unloading starts. In principle the same applies to the molecules at a temperature of 25 mK but here single state pumping is applied before unloading of the molecules from the trap, transferring the molecules with high efficiency into the M=3 sublevel of $|3,3,0\rangle$ so that >95 % percent of the molecules are in this single state [Glö16, Pre18]. The value for the saturation intensity resulting from the fit decreases for lower temperatures because it becomes easier to saturate the transition as the molecules spend more time in the excitation volume due to their lower velocity. The values for a frequency broadened laser beam are considerably higher than without broadening as the power spectral density is lower due to the larger spread in frequency space. Note that the saturation power marks where the first subset of molecules gets saturated and till which laser power the signal increase is linear, the

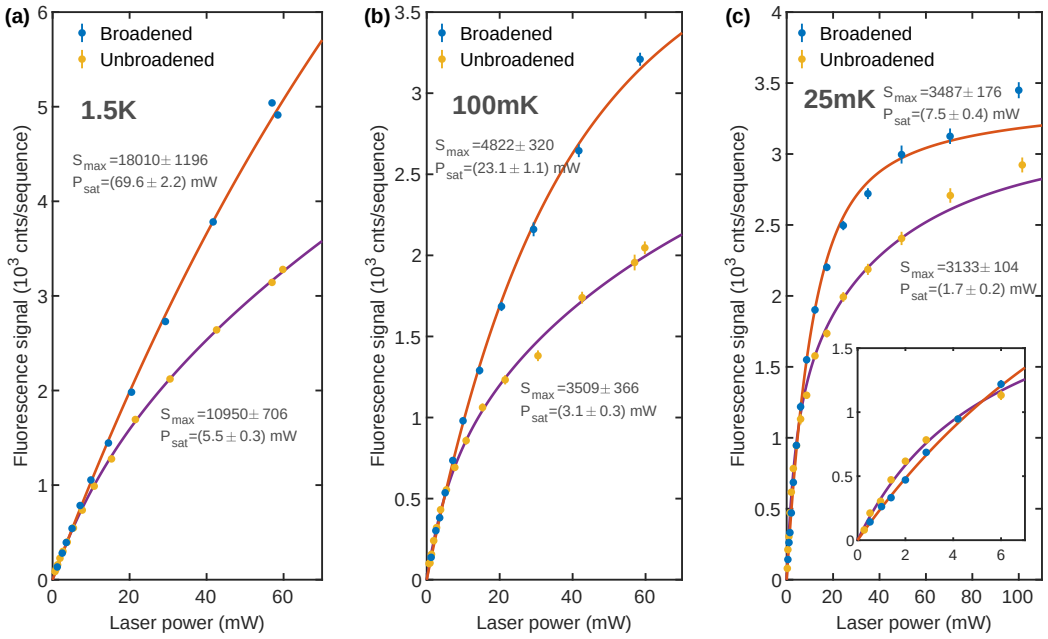

Figure 4.13: Laser power saturation measurements. The laser power is varied for three different temperatures with and without frequency broadening of the laser (see main text for broadening techniques). The curves are fitted with the saturation model described in Equation (4.6). The constants common to all fits are the molecule beam width w_{mol}=(2.21 ± 0.03) mm and the laser beam width w_{las}=2.3 mm. The laser linewidth is assumed to be $\Delta\nu_{\mathrm{las}}$=(1.00 ± 0.03) MHz in the unbroadened cases and to cover the whole frequency span of the transition in the broadened cases. The free parameters of the model are P_{sat}, P_{broad} and S_{max}. The given error bars only include statistical errors. **(a)** Measurement with uncooled molecules in a fly-through configuration. Only about 15 % of the molecules are in the state $|3,3,0\rangle$ and are detected. The Doppler width is $\Delta\nu_{\mathrm{D}}$=(10.15 ± 0.03) MHz. Due to the considerable extrapolation S_{max} is assumed to be only correct within a factor of 2. **(b)** Measurement with cooled molecules at a temperature of 100 mK with a Doppler width of $\Delta\nu_{\mathrm{D}}$=(4.68 ± 0.06) MHz. Half of the molecules are detected as they are equally distributed between $|3,3,0\rangle$ and $|4,3,1\rangle$ after optoelectrical Sisyphus cooling. The systematic error is estimated to be about 20 %. **(c)**. Measurement at a temperature of 25 mK with a Doppler width of $\Delta\nu_{\mathrm{D}}$=(2.59 ± 0.06) MHz. All molecules are detected due to optical pumping into $|3,3,0\rangle$ after the cooling sequence. The inset shows a magnification of the low laser power range. The systematic error is estimated to be <10 %.

total signal itself still rises by about at least a factor of 3 more.

In particular for the measurements with warmer molecules the value of S_{max} is based on considerable extrapolation making the value very sensitive to systematic effects. The given errors are only based on a propagation of the statistical errors of the measured saturation curves and the constant values entering Equation (4.6). Not included is the fact that the size of the molecule beam could vary for colder molecules even though this effect is estimated to be small as explained in the previous paragraph. Furthermore, in principle it is possible that the applied voltage ramp or the EOM does not lead to an excitation of the whole Doppler broadened line. However, for both techniques, broadening with an EOM and shifting the transition

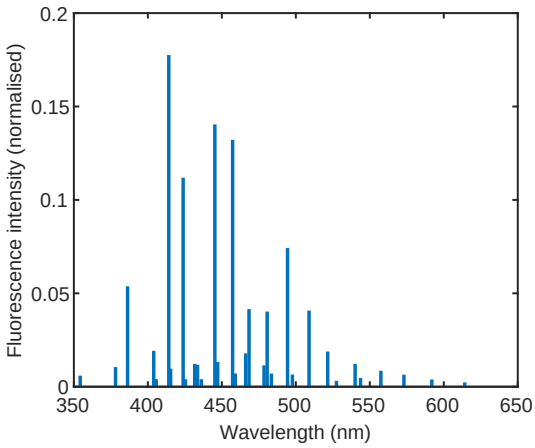

Figure 4.14: Fluorescence spectrum of the $\tilde{X}^1A_1$ 4^1 excited state of formaldehyde. The main intensity is emitted from 415 nm to 460 nm. Only about 0.5 % of the molecules decay back to the vibronic ground state. Figure taken from Ref. [Bou96].

with a frequency ramp, very similar results are achieved, making this systematic error unlikely. The values for $S_{\max}$ are consistently lower for the unbroadened case which is probably due to the uncertainty in the spectral width of the laser or rather the spectral width addressed by the laser without any broadening mechanism applied. For these reasons, the values obtained from the frequency broadened measurements are the most trustworthy. Nevertheless, due to the strong extrapolation the measurement for uncooled molecules at 1.5 K are estimated to only be correct within about a factor of 2. For the broadened curve this is due to the strong extrapolation and without broadening to the uncertainty of the laser linewidth. The distorted spectrum in Figure 4.11 shows that due to Stark broadening the assumed value of 1 MHz, which was determined under a different voltage configuration at the quadrupole guide, is probably not precisely correct. For the measurements at colder temperatures the values without broadening are estimated to be correct within 20 % for the same reason, namely the lack of knowledge about the exact frequency span the laser addresses without additional broadening. The curves for cooled molecules and including frequency broadening are the most trustworthy with an estimated systematic error of <10 %.

4.5.2 Experimental losses

In this section the losses in the detection setup caused by experimental constraints and imperfections are discussed. Since most effects are wavelength dependent it is useful to first have a closer look at the fluorescence spectrum of formaldehyde.

Fluorescence spectrum of the $\tilde{A}^1A_2$ 4^1 state As already mentioned in Chapter 2 the Franck-Condon overlap for the $\tilde{A}^1A_2 \leftarrow \tilde{X}^1A_1$ 4^1 transition of formaldehyde is very small, making laser cooling impossible. This is also represented in the broad fluorescence spectrum shown in Figure 4.14 which is taken from Ref. [Bou96]. Only a negligible amount of about 0.5 % of the fluorescence intensity comes from a decay

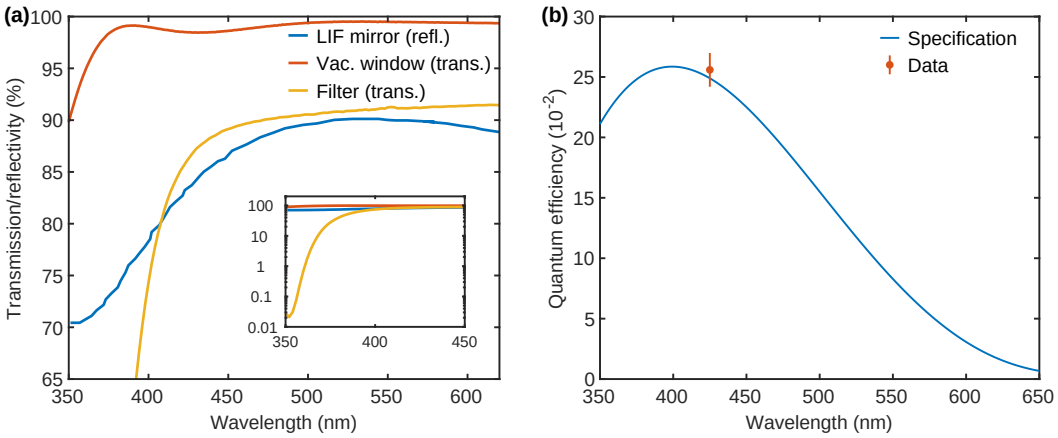

Figure 4.15: Experimental losses. (a) Plotted are transmissions and reflectivity of the optical elements used for light collection in the LIF detection scheme. The reflectivity of the LIF mirror is provided by the manufacturer Kugler. The transmission of the re-entry vacuum window is measured with a spectrophotometer. The transmission of the Schott GG385 colour filter is provided by a measurement from the distributing company Itos. **(b)** Quantum efficiency of photomultiplier tube (PMT) R6094P from Hamamatsu as it is specified in the datasheet. The measured data point for validation is obtained by exposing the PMT to an attenuated light-emitting diode.

back into the v=0 vibrational mode of the electronic ground sate. Most of the fluorescence is spread out from 385 nm to 510 nm with some weaker bands reaching up to almost 620 nm. The discrete spectrum is caused by decays to individual excited vibrational modes in the electronic ground state $\tilde{X}^1A_1$. The most intense bands are located around 415 nm to 460 nm.

Transmissions and reflectivities of optical elements After excitation of the molecules there are three optical elements the fluorescence light interacts with before detection by the PMT. First, the light is reflected by the surface of the LIF mirror coated with protected aluminium[5]. The reflectivity as specified by the manufacturer Kugler is shown in Figure 4.15(a). It rises from about 80 % at a wavelength of 400 nm to almost 90 % at 600 nm. At the excitation wavelength it still has a sizeable reflectivity of about 70 %. The coating of the spherical half of the LIF mirror is bad in the very steep parts close to the edge (see Section 3.2). In this region the mirror is assumed to have the reflectivity of copper which is about 45 % for the fluorescence wavelengths and 35 % for the excitation laser wavelength.

The next optical element is the re-entry vacuum window incorporating the PMT. The glass of the window is broadband anti-reflex coated and has a high transmission of >98 % over the full width of the fluorescence spectrum. A measurement of the transmission is also shown in Figure 4.15(a). The transmission for the excitation wavelength of 354 nm is a bit lower with about 92 %.

The last optical element is a colour filter GG385 from Schott. As can be seen

[5]Protected aluminium consists of a layer of aluminium coated with an additional dielectric protective layer to prevent oxidisation of the aluminium on air.

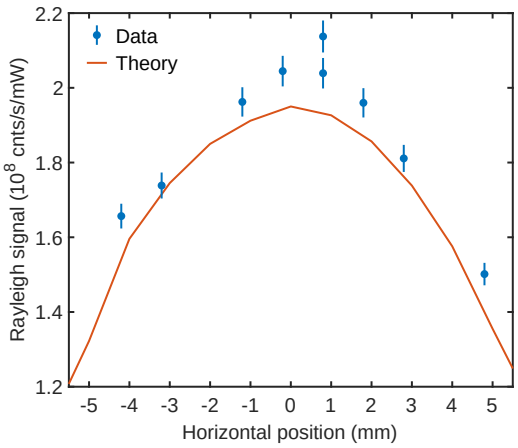

Figure 4.16: Imaging efficiency of the LIF setup for Rayleigh scattering. Signal caused by Rayleigh scattering of the UV laser at 354 nm by nitrogen at room pressure. The simulated curve is calculated with Zemax based on the Rayleigh scattering cross-section of nitrogen in Ref. [Tha14] and includes all known experimental losses.

from the curve in Figure 4.15(a) it has a transmission of about 90 % for wavelengths >400 nm. Its purpose is to filter out stray light from the excitation laser as explained in Section 3.3.4 which is achieved with a suppression of 3×10^{-4} as shown in the inset of Figure 4.15(a).

Quantum efficiency of PMT For detection a photomultiplier tube (PMT) is used as described in Section 3.2. It has a maximum quantum efficiency of 25 % at a wavelength of about 400 nm which slowly decreases towards longer wavelengths. The specified curve is shown in Figure 4.15. The quantum efficiency is experimentally validated at 425 nm which results in a value of (25.6 ± 1.4) % confirming the specification. The value is obtained by exposing the PMT to the attenuated emission of a light-emitting diode.

Validation of imaging efficiency of the LIF mirror In order to verify the calculation of the imaging efficiency of the LIF mirror presented in Section 3.2 and the experimental losses, a validation measurement is performed. To this end the vacuum chamber is flooded with nitrogen at room pressure and the signal caused by Rayleigh scattering of the UV laser beam at 354 nm recorded. The laser is focussed with a waist of about 200 µm in the centre of the LIF mirror and the position of the laser is varied along the horizontal direction, i.e. the larger dimension of the elongated hole of the entrance aperture of the LIF mirror. By moving the laser from the centre position the measured signal decreases due to a lower imaging efficiency as can be seen from the result of the measurement plotted in Figure 4.16. For comparison the amount of theoretically expected signal is also shown. It is based on a ray tracing simulation with the software Zemax. The amount of scattered photons is calculated using the Rayleigh scattering cross-section of nitrogen given in Ref. [Tha14]. The angle distribution is weighted according to the common Rayleigh scattering angle

	Temperature	Extr. signal $S_{\max}$	No. molecules in $\|3,3,0\rangle$
Fly-through measurement	1.5 K	$(1.80 \pm 0.12) \times 10^4$	$(5.63 \pm 0.24) \times 10^5$
$f_{\mathrm{RF}} - f_{\mathrm{off}}$=1074 MHz	100 mK	$(4.82 \pm 0.10) \times 10^3$	$(1.51 \pm 0.11) \times 10^5$
$f_{\mathrm{RF}} - f_{\mathrm{off}}$=191 MHz	25 mK	$(3.49 \pm 0.18) \times 10^3$	$(1.09 \pm 0.06) \times 10^5$
Maximum detection efficiency $\|3,3,0\rangle$		(3.2 ± 0.1) %	
Maximum detection efficiency $\|1,1,0\rangle$		(8.8 ± 0.2) %	

Table 4.2: Calibration of the absolute number of molecules and detection efficiency of the LIF detection scheme. The extrapolated maximum signal $S_{\max}$ is taken from the saturation measurements presented in Sec. 4.5.1. Only molecules in the state $|3,3,0\rangle$ are detected which means that for the fly-through measurement at 1.5 K only about 15 % of all molecules are detected. For 100 mK half of the molecules are in the state $|3,3,0\rangle$ and for 25 mK more than 95 % due to optical pumping. The overall detection efficiency depends on the state to be detected due to the varying quantum yield of the detection transitions available.

distribution with $(1 + \cos\theta^2)$ [Bor99]. The light is then propagated through the LIF setup including the experimental losses given in this section. The result shown in Figure 4.16 agrees very well with the measured values. On average the theory curve deviates by only about 3 % from the experimental values. Therefore, it can be assumed that the simulation of the imaging efficiency of the system is valid within a few percent.

4.5.3 Number of molecules

To determine the detection efficiency and the number of molecules the experimental losses in the system discussed in the previous section have to be combined with the results from the saturation measurements. The molecules are excited by the UV laser where the fraction of excited molecules is given by the model presented in Section 4.5.1. Subsequently, the molecules emit fluorescence light with the spectrum shown in Figure 4.14 and the quantum yield determined in Section 4.3. The light is then collected and imaged onto the PMT by the LIF mirror with an efficiency of about 58 %, a value which already includes the reflectivity of the LIF mirror. The losses introduced by the vacuum window and the colour filter lead to a cumulated transmission of about 88 %. The detection with the PMT happens with an average efficiency of about 21 %. Combining these values allows to give an absolute number of molecules based on the extrapolation of the signal in Section 4.5.1. The result is summarised in Table 4.2. The molecule numbers are based on the extrapolation from the saturation measurements with a frequency broadened laser. Error bars include only statistical errors and the most significant systematic error by far comes from the extrapolation of $S_{\max}$ as is argued in the previous section. Therefore, the same estimation of systematic errors applies as already discussed in Section 4.5.1, namely an error of 50 % for uncooled molecules at 1.5 K, about 20 % for the inter-

mediate cooling sequence at 100 mK and <10 % for the coldest molecules at 25 mK. Furthermore, an overall detection efficiency is given in Table 4.2 which of course depends on the rotational state to be detected due to the quantum yield of the involved transition. For this efficiency perfect saturation of the transition is assumed and the systematic error is on the order of a few percent.

The molecule numbers given in this section are considerably lower than what has been measured previously with a QMS where 3×10^5 molecules at temperatures <1 mK were given [Pre18]. The cooling steps applied to bring the molecules down to 25 mK introduce losses of about 20 % per cooling step, each reducing the temperature by a factor of $\sqrt{2}$. This is in good agreement with what has been observed previously. Assuming that following cooling steps produce about the same amount of relative molecule loss only about 3×10^4 molecules would be left at 400 µK. This is about a factor of 10 lower than what was previously assumed. The reasons for this discrepancy are not entirely clear. As was discussed already in this section, the values obtained with LIF should not have an error big enough to explain the difference. The number calibration performed with the QMS was claimed to be accurate within a factor of 2 which consequently cannot account for the difference either. One conclusion is that the calibration with either the QMS or the one presented here with LIF have a considerable flaw that has been overlooked. Another possibility is that for some undetected technical reason there are less molecules now than there were in the past. However, no indication is found supporting this speculation.

Theoretically, the detection efficiency has been increased drastically by the new detection scheme based on LIF. For the detection of the rotational state $|3, 3, 0\rangle$ the increase by detection with the scheme based on LIF is about two order of magnitude compared to the detection with a QMS where the detection efficiency ranged between 1×10^{-4} and 4×10^{-4}, depending on the velocity of the molecules [Pre18]. However, the issue of disagreeing molecule number remains unresolved for the time being leaving a final conclusion still open.

Due to a higher background the increased detection efficiency does not automatically translate into a similar decrease in measurement time. However, for colder molecules the UV laser power necessary to saturate the detection transition decreases leading to higher signal to noise values for lower temperatures. Also, the state selectivity of the method removes the need to perform difference measurements to determine the number of molecules in a particular subset of rotational states [Glö15a] halving the measurement time in many cases. Furthermore, the state selectivity of the method enables a number of novel experiments previously impossible. Two of these applications of the new detection scheme are presented in the remaining chapters of this thesis.

5 Ortho ground state preparation

In this chapter the preparation of cold, Sisyphus cooled formaldehyde molecules in the rotational ortho ground state is presented. The technique relies on the capability to distinguish between different rotational quantum states of the formaldehyde molecules making it an ideal application of the LIF detection scheme due to its state selectivity.

Formaldehyde exists in the form of two different spin isomers, just as e.g. the hydrogen or the water molecule. These isomers are labelled *para* and *ortho*. *Para* means that both spins of the hydrogen nuclei are aligned antiparallel resulting in an antisymmetric spin wavefunction. Therefore, the rotational wavefunction has to be symmetric in order to fulfil the Pauli exclusion principle which requires the total wavefunction to be antisymmetric (see Equation (2.11)). This results in para-formaldehyde with antiparallel spins only being allowed in states with even K_a quantum numbers (see Section 2.1.3). *Ortho* on the other hand stands for parallel aligned hydrogen spins which in the case of formaldehyde requires odd K_a quantum numbers to comply with the symmetry constraints of the Pauli principle. The conversion between ortho and para states requires a nuclear spin flip, and therefore is strongly spin forbidden. Not even collisions seem to give relevant conversion rates as has been investigated in the context of astrochemistry [Tud06]. For astrophysical sources the understanding of the ortho-para ratio of formaldehyde is crucial [Tro09] as it can be used to e.g. determine the temperature of interstellar clouds [Dic99]. Due to the extremely low interconversion rate, ortho- and para-molecules can almost be treated as two distinct molecule species. For this reason, it can also be argued that there are two ground states. The para ground state is the energetically absolute ground state with J=0. The ortho ground state with J=1, K_a=1 is actually a doublet of parity states split up by K-type doubling (see Section 2.1.2) as is the case for most states of an asymmetric rotor. Naturally, in a static electric trap such as it is employed in this experiment only trapping of states with a positive Stark shift is possible, limiting trapping to the $|1, 1, 0\rangle$ state.

Trapped molecules in the $|1, 1, 0\rangle$ state can be obtained by simply working with molecules not previously Sisyphus cooled. The molecules entering the electric trap have a Boltzmann internal state distribution at 150 K and are velocity filtered by the electric quadrupole guide. This results in the $|1, 1, 0\rangle$ state being one of the more abundantly populated states of the initial molecule sample in the trap with a population of about 5 % [Pre18]. However, the trapped molecules have a temperature of about 600 mK and cannot be cooled due to a missing second trapped M-sublevel required for optoelectrical Sisyphus cooling (see Section 2.2.1). Also, the standard cooling scheme is only accessible to symmetric rotor molecules or, as is the case for formaldehyde, slightly asymmetric rotors where the states split up by K-type doubling are strongly coupled by the electric field such that they behave like a

symmetric rotor. To overcome this problem and provide molecules in the ortho ground state at lower temperatures, in this chapter a technique is presented which allows to first cool the molecules in the states $|3,3,0\rangle$ and $|4,3,1\rangle$, as is routinely done with the standard optoelectrical Sisyphus cooling scheme [Pre18], and then transfer those cold molecules to the state $|1,1,0\rangle$.

Ground state pumping is of considerable importance because in these states molecules are stable against inelastic collisions. This is an important requirement for evaporative cooling as it relies on a favourable ratio between elastic and inelastic collisions. To achieve the goal of bringing formaldehyde into the quantum degenerate regime the envisioned course is to first cool the molecules with optoelectrical Sisyphus cooling to ultracold temperatures and then transfer them into a microwave trap. Here, also molecules in low field seeking states such as $|1,1,1\rangle$ can be trapped. This will allow further cooling via an adapted Sisyphus cooling scheme as outlined in Chapter 7 and also bring evaporative cooling within reach. A further application of optical pumping to the $|1,1,0\rangle$ state is the measurement of coherence times between its rotational sublevels. This experiment is presented in detail in Chapter 6 of this thesis.

In Section 5.1 the transfer scheme based on optical pumping and the involved level structure is explained and an estimate for the efficiency is given. In Section 5.2 the experimental results are presented.

5.1 Optical pumping scheme

For formaldehyde optoelectrical Sisyphus cooling typically takes place in the rotational states $|3,3,0\rangle$ and $|4,3,1\rangle$ of the vibronic ground state. The choice is mainly motivated by the high population of these two states which contain about 20 % of the molecules loaded initially into the electric trap [Pre18]. After cooling the molecules are distributed equally between the highest M-sublevels of the two cooling states due to coupling via MW (see Section 2.2.1). As a transfer technique to the ortho ground state $|1,1,0\rangle$ an obvious choice is optical pumping via a vibrational excitation, because of the strict rotational selection rules. However, the v_1 vibrational mode used for the cooling cycle is not suitable for this transfer. Due to the A_1 symmetry of the mode, the rotational selection rules of Equation (2.10a) (ΔK_a=$0, \pm 2, \ldots$ and ΔK_c= $\pm\, 1, \pm 3, \ldots$) apply. This means that for the two-fold transition involved in optical pumping, first the excitation by a laser and then a subsequent spontaneous decay, one of the two transitions would have to rely on a ΔK=2 transition, which is strongly suppressed for slightly asymmetric rotors such as formaldehyde.

More suitable is the vibrational antisymmetric C-H stretch mode v_5 which has the symmetry type B_2 (see Table 2.1) meaning that b-type selection rules ΔK_a= $\pm\, 1$ and ΔK_c= $\pm\, 1$ (refer to Equation (2.10b)) apply. The full pumping scheme based on an excitation to this mode including all involved states is presented in Figure 5.1. Shown are the different rotational states in the vibronic ground state $\tilde{X}^1A_1$ and the two excited vibrational modes v_5=1 and v_1=1 involved in the pumping scheme as well as the vibronic excited state $\tilde{A}^1A_2\ 4^1$ used for detection. Starting from the M=3 sublevel of the rotational state $|3,3,0\rangle$ an IR laser excites the molecules to the $|2,2,0\rangle$

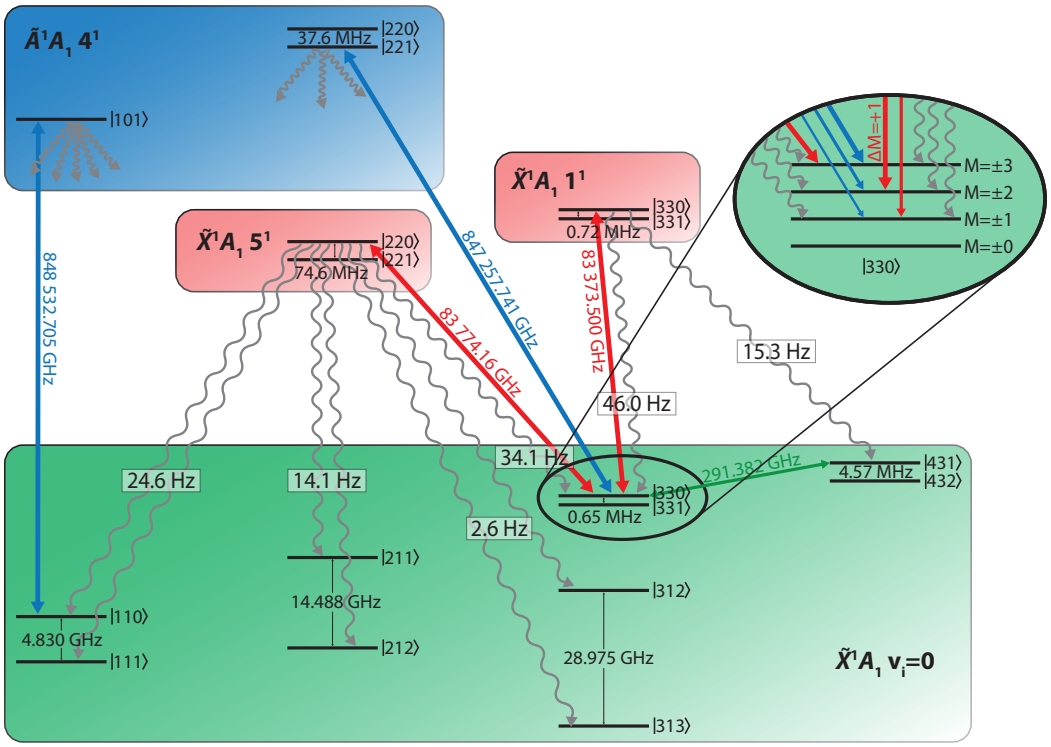

Figure 5.1: Detailed level scheme for optical pumping into the ortho ground state $|1,1,0\rangle$. After Sisyphus cooling the molecules end up in the highest M-sublevels of the states $|3,3,0\rangle$ and $|4,3,1\rangle$. Red solid lines indicate IR lasers for vibrational excitation of the molecules. Wavy grey arrows represent spontaneous decays. The optical pumping takes place inside the electric trap with a typical electric field strength of 628 $\frac{\mathrm{V}}{\mathrm{cm}}$ coupling the states with small K-type doubling. The J=4 state is incorporated by MW radiation in combination with the IR laser coupling to the v_1=1 mode, which transfers the molecules into the highest M-sublevels and thus serves as repumper. For completeness also the detection transitions driven by the UV laser are shown by the solid blue lines. This excitation takes place in the LIF detection area with a much lower electric field. IR and UV frequencies are experimentally determined values. The rotational constants used for the calculation of the splitting caused by K-type doubling in the vibrational excited states and also the vibronic excited state are taken from Ref. [Clo83]. The rotational constants of the vibronic ground state are taken from Ref. [Brü03]. The vibrational decay rates are given in the HITRAN database [Gor17]

rotational state of the $\tilde{X}^1A_1$ 5^1 vibrational state. Since the molecules are trapped in an electric trap (see description in Section 2.2.2) the optical pumping happens in the presence of an electric field. For the standard setting used for cooling of the molecules the electric field strength is 628 $\frac{\mathrm{V}}{\mathrm{cm}}$ which easily couples the parity doublet in the excited state which has a splitting of 74.6 MHz and makes this transition possible. This is confirmed by a calculation of the transition matrix elements shown in Figure 5.2.

From the rotational $|2,2,0\rangle$ state in the vibrationally excited state the molecules decay according to the selection rules into the rotational states $|J$=1, K_a=1$\rangle$, $|J$=2, K_a=1$\rangle$, $|J$=3, K_a=1$\rangle$ and $|J$=3, K_a=3$\rangle$ of the vibronic ground state $\tilde{X}^1A_1$ as

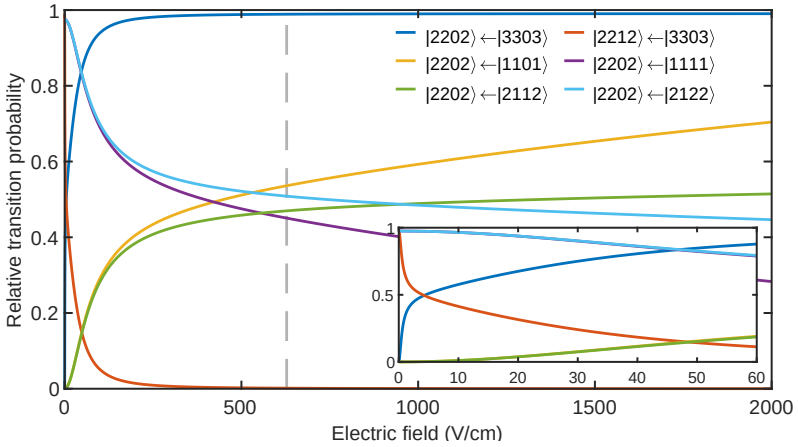

Figure 5.2: Electric field dependence of transition probabilities for the states involved in the ortho ground state preparation. The dashed line at 628 $\frac{\mathrm{V}}{\mathrm{cm}}$ marks the electric field strength of the electric trap operated with standard voltage configuration. The target state $|J{=}2, K_a{=}2, K_c{=}0, M{=}2\rangle$ is located in the vibrationally excited state $\tilde{X}^1A_1\ 5^1$ whereas the other states are in the vibronic ground state $\tilde{X}^1A_1$. Depending on the splitting caused by K-type doubling the electric field couples corresponding states with different rates resulting in a characteristic shape of the curves with a steeper rise to about 0.5 followed by a slower rise up to 1. The inset shows a close up of the graphs for low electric field values.

indicated in Figure 5.1. The molecules decaying into each particular manifold distribute approximately equally between the two states of the parity doublets because the electric field is not strong enough to couple both states for the large K-type doubling splittings of several GHz. This fact also becomes apparent from the transition probabilities in Figure 5.2. The only exception is of course the decay into $|J{=}3, K_a{=}3\rangle$ which happens with about 99 % probability into the upper state of the doublet $|3, 3, 0\rangle$. The decay rates into the various rotational states vary by more than an order of magnitude. The strongest decay is the one back into the state of origin $|3, 3, 0\rangle$ with 34.1 Hz. The molecules decaying via this channel can be repumped with high efficiency as is explained in the next paragraph. The second strongest decay with 24.6 Hz is the desired decay into the states $|J{=}1, K_a{=}1\rangle$, i.e. the ortho ground state of the molecule. The two weaker decays with 14.1 Hz and 2.6 Hz lead into the $|J{=}2, K_a{=}1\rangle$ and the $|J{=}3, K_a{=}1\rangle$ manifolds respectively. The part of the molecules decaying into the upper state of these doublets with positive Stark shift could in principle be repumped, however, due to a lack of appropriate radiation sources these molecules are lost.

For completeness in Figure 5.1 also the vibronic states used for detection are shown. For the detection of molecules in the state $|3, 3, 0\rangle$ the transition into the state $\tilde{A}^1A_2\ 4^1\ |2, 2, 1\rangle$ is used as is explained in great detail in Chapter 4. For the detection of molecules in the upper state of the ortho ground state doublet $|1, 1, 0\rangle$ the transition into the state $\tilde{A}^1A_2\ 4^1\ |1, 0, 1\rangle$ is the most convenient choice, as it offers a high quantum yield of the excited state of (84 ± 1) % as determined in Section 4.3. Both of these detection excitations of course do not happen in the electric trap but in the LIF detection region within the LIF mirror, meaning that

the electric field is typically much weaker here than in the electric trap.

Accumulation[1] for increased efficiency As already mentioned, after Sisyphus cooling the molecules end up equally distributed between the highest M sublevels of the states $|3,3,0\rangle$ and $|4,3,1\rangle$. Therefore, by only exciting the molecules via the transition $\tilde{X}^1A_1 \leftarrow \tilde{X}^1A_1\ 5^1_0\ |2,2,0\rangle \leftarrow |3,3,0\rangle$ half of the molecules are not addressed. Another source of loss is the spontaneous decay back to the rotational state $|3,3,0\rangle$. The selection rule $\Delta M = 0, \pm 1$ on the one hand ensures that molecules are only driven to the M=2 sublevel of the excited $|2,2,0\rangle$ state, and therefore can only decay to the M=1 state of the ortho ground state $|1,1,0\rangle$ and not to the untrapped M=0 state. On the other hand, this selection rule allows decay back into lower, more weakly trapped M- sublevels of the $|3,3,0\rangle$ state. The optical pumping transitions from these states are blue-detuned from the transition originating in M=3. Due to a negative differential Stark shift between ground and excited state the transitions from these lower M sublevels are still driven, however much less efficiently because they only take place in high electric field parts of the trap. Furthermore, lower M-sublevels of the excited state can be populated by this process leading to loss via spontaneous decay into the M=0 sublevel of the target state $|1,1,0\rangle$.

In order to avoid these two loss mechanisms and increase the efficiency, the molecules can be accumulated into higher M-sublevels of the $|3,3,0\rangle$ state as is also done during optoelectrical Sisyphus cooling. To this end, the molecules in $|J$=3, K_a=3$\rangle$ are excited with another IR laser to the $|3,3,0\rangle$ state of the v_1=1 vibrational mode via a $\Delta M = +1$ transition as shown in Figure 5.1. This way the molecules preferentially decay back into the M=3 sublevel which is dark to this second IR laser. The decay channel to $|4,3,1\rangle$ is easily closed with millimetre wave radiation as it is commonly applied during cooling. This automatically includes the molecules in J=4 into the pumping scheme, doubling the number of addressed molecules. Its addition to the optical pumping sequence substantially increases the efficiency of the state preparation into the ortho ground state as can be seen from the experimental results in the next section.

Since accumulation happens with a very high efficiency and close to zero losses, the efficiency of the transfer into the ortho ground state $|1,1,0\rangle$ in theory amounts to $> 30\,\%$ when taking into account the losses into the states $|2,1,1/2\rangle$ and $|3,1,2/3\rangle$ as well as into the untrapped state of the ground state doublet.

Experimental setup The experimental setup for the ground state preparation is rather straightforward. A second IR laser of the same type as the one already in use for Sisyphus cooling is installed. Details about this laser can be found in e.g. Ref. [Eng13]. The laser is not referenced onto the optical frequency comb but instead frequency stabilised onto a wavemeter which is sufficiently precise for the present application. The laser beam for optical pumping is superimposed on the IR laser used for cooling, using a non-polarising beamsplitter, ensuring that the molecules

[1] Strictly speaking the process of accumulation into higher M-sublevels is of course also optical pumping. However, for the sake of discriminability, in this work only the transfer of molecules into the ortho ground state is referred to as optical pumping while the transfer of molecules into higher M-sublevels of the same rotational state is referred to as accumulation.

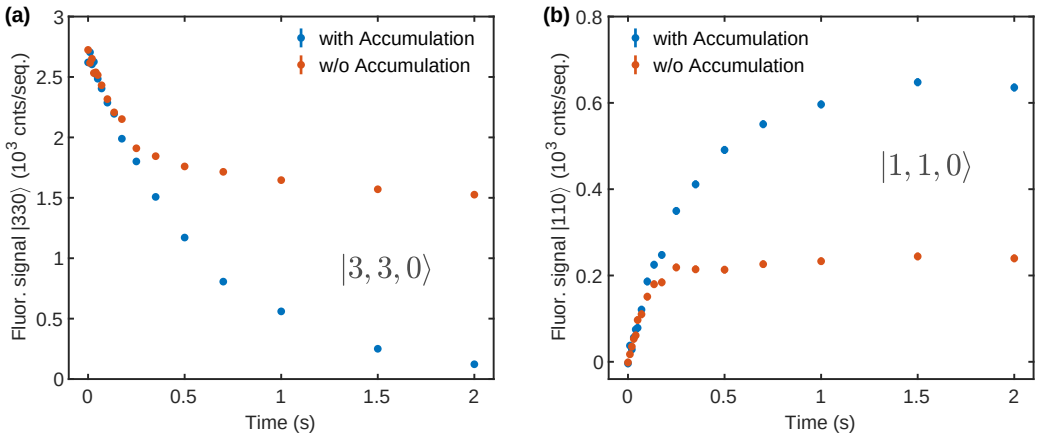

Figure 5.3: Saturation curves for optical pumping to the $|1,1,0\rangle$ state. The time dependence of the state preparation in the $|1,1,0\rangle$ state is measured with and without accumulation into the higher M-sublevels of $|3,3,0\rangle$ and $|4,3,1\rangle$. **(a)** Signal measured in the state $|3,3,0\rangle$. After the optical pumping sequence an additional 0.5 s of accumulation is added to make the molecules that decayed during optical pumping into lower M-sublevels visible. This also mixes the states with J=3 and J=4. **(b)** Measurement of the signal in the ortho ground state $|1,1,0\rangle$. With longer optical pumping time the signal increases as it decreases in the initial state $|3,3,0\rangle$

are illuminated efficiently. To avoid losses during cooling or unloading the beam path can be blocked by a remotely controlled mechanical shutter.

5.2 Experimental results

For an experimental demonstration of ortho ground state preparation, formaldehyde molecules cooled with a standard sequence as already described e.g. in Section 4.4 are used. The molecules are cooled down to a final cooling frequency of $f_{\mathrm{RF}} - f_{\mathrm{offset}} = (909-184)\,\mathrm{MHz} = 725\,\mathrm{MHz}$, corresponding to a temperature of about 60 mK, and detected after unloading via the transition $\tilde{A}^1A_2 \leftarrow \tilde{X}^1A_1\ 4_0^1\ |2,2,1\rangle \leftarrow |3,3,0\rangle$. For the ground state preparation an additional 2 s of storage time is added to the sequence after cooling. By shining in the infrared laser for optical pumping for varying times during this additional storage time, the fluorescence signal, and therefore the number of molecules, in the detected state $|3,3,0\rangle$ decreases. This behaviour can be seen in the measurement without accumulation during optical pumping in Figure 5.3(a). Before unloading the molecules after the 2 s of optical pumping, an additional 0.5 s of accumulation into the highest M-sublevels of the states $|3,3,0\rangle$ and $|4,3,1\rangle$ is added. This is necessary to make the molecules that decayed into lower M-sublevels of the $|3,3,0\rangle$ state visible again[2] without changing the detection

[2]Due to a lower Stark shift lower M-sublevels experience a different size of the exit hole of the electric trap requiring different voltages applied to the electric guide an the ring electrode for optimal unloading [Pre18]. Furthermore, the UV laser frequency as well as the voltage ramp applied to the guide cap of the LIF detection have to adjusted for an efficient detection of lower M-sublevels.

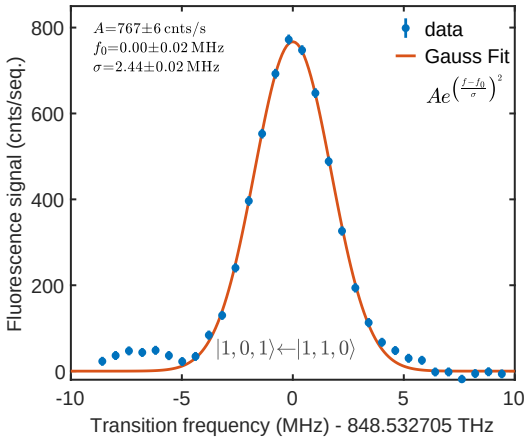

Figure 5.4: UV spectrum of the $\tilde{A}^1A_2 \leftarrow \tilde{X}^1A_1$ 4_0^1 $|1,0,1\rangle \leftarrow |1,1,0\rangle$ transition. This transition is used to detect molecules in the ortho ground state $|1,1,0\rangle$. The experimental sequence is the same as the one used for the time dependence of the state preparation with the only difference being that optical pumping is only applied for 0.75 s.

and unloading parameters. As a side effect the molecules in the state $|4,3,1\rangle$, which were unaffected by the optical pumping, are redistributed between J=3 and J=4 by the millimetre wave radiation of the accumulation scheme. Therefore, the measured signal for the curve without accumulation during the optical pumping in Figure 5.3 can only drop down to half of the initial value with no optical pumping. However, the signal is only depleted to about 60 % which can be attributed to the molecules that decay to the lower M-sublevels.

Adding accumulation also during the optical pumping sequence includes the molecules in the state $|4,3,1\rangle$ and repumps those decaying into M=2 or lower M-sublevels of the state $|3,3,0\rangle$. A measurement of this sequence is also shown in Figure 5.3(a). With accumulation the pumping process depletes the signal to almost zero, effectively removing the molecules from the state $|3,3,0\rangle$, and therefore also the state $|4,3,1\rangle$ which is coupled to the $|3,3,0\rangle$ state by MWs.

Molecules in the ortho ground state $|1,1,0\rangle$ To detect molecules in the ortho ground state $|1,1,0\rangle$ the UV detection laser is tuned to the transition $\tilde{A}^1A_2 \leftarrow \tilde{X}^1A_1$ 4_0^1 $|1,0,1\rangle \leftarrow |1,1,0\rangle$. A spectrum of this transition for cold molecules with a temperature of about 60 mK in the $|1,1,0\rangle$ state is shown in Figure 5.4 and the transition frequency is determined to be 848.532 705 THz. As expected for a Doppler broadened transition the lineshape is nicely Gaussian but there is a small side peak red-detuned from the transition whose origin is not clear. It cannot stem from the splitting of the M=1 and M=0 sublevels in the excited state $\tilde{A}^1A_2$ 4^1 $|1,0,1\rangle$ as this splitting is only about 10 kHz for the electric fields in the detection region due to the quadratic Stark shift of the excited state. Therefore, it is not clear if the feature has a physical origin or if it is just an experimental artefact. The amount of fluorescence signal at zero detuning from the transition frequency in Figure 5.4 is the amount of signal in the ortho ground state $|1,1,0\rangle$.

In Figure 5.3(b) the time dependence of signal in the state $|1,1,0\rangle$ with increasing optical pumping time can be seen. The curves are measured for the same experimental sequence as described for the measurement in the state $|3,3,0\rangle$ in Figure 5.3(a) with the only difference that molecules in the ortho ground state are detected instead of the state $|3,3,0\rangle$. It can nicely be seen how the molecules appear in the state $|1,1,0\rangle$ while they disappear in the state of origin $|3,3,0\rangle$. Without accumulation during the optical pumping sequence the signal is much lower than with accumulation applied. The saturation level is more than twice as high due to the processes explained before: Twice as many molecules are addressed due to coupling of the states $|3,3,0\rangle$ and $|4,3,1\rangle$ by millimetre waves and molecules from lower M-sublevels are repumped.

The number of molecules pumped into the ortho ground state cannot directly be determined from the presented measurement. To do so laser power saturation measurement such as the ones discussed in Section 4.5.1 would have to be performed. Nevertheless, it is immediately clear that the amount of signal in the the state $|1,1,0\rangle$ does not comply with the state transfer efficiency of $> 30\,\%$ claimed in Section 5.1 and a detection efficiency which is higher by a factor of 2.7 due to the higher quantum yield of the vibronically excited state than the detection efficiency in $|3,3,0\rangle$ as determined in Section 4.5. There are several reasons for this discrepancy, two of them lying within the detection. First, the UV laser power at the transition for the detection of the state $|1,1,0\rangle$ is lower than for the detection of $|3,3,0\rangle$. How much this affects the signal could only be determined with a saturation measurement. The second reason is that laser broadening is not applied for the detection, and therefore only a subset of all velocities in the Doppler broadened line is excited. A shifting of the transition by using alternating electric fields is not possible for the state $|1,1,0\rangle$ due to the weak quadratic Stark shift. Finally, the trap lifetime of the molecules in the ortho ground state is much shorter than in the $|3,3,0\rangle$ state as is shown later in this section.

Infrared spectrum The optical pumping efficiency is quite sensitive to the infrared frequency applied. A spectrum of the strongly saturated transition is presented in Figure 5.5. Plotted is the signal in the state $|1,1,0\rangle$ depending on the exact IR frequency. The curve is asymmetric due to the electric field distribution in the trap which is presented in the context of another experiment in Figure 6.7. The homogeneous electric field in the centre of the trap at $628\,\frac{\mathrm{V}}{\mathrm{cm}}$ is the most prevalent value with the electric field distribution centred around it. For confinement there are much stronger electric fields towards the edges of the trap leading to a distribution with a very long tail towards high electric fields. There are also lower electric fields due to the presence of electric field zeros in the trap. A detailed description of the geometry and probability distribution of the electric fields in the trap is given in Refs. [Zep13, Pre18]. The transition for optical pumping $\tilde{X}^1A_1 \leftarrow \tilde{X}^1A_1\ 5_0^1\ |2,2,0\rangle \leftarrow |3,3,0\rangle$ has a negative differential Stark shift, meaning that the Stark shift in the ground state is higher than in the excited state so that the transition frequencies are red-detuned for higher electric fields. This explains the shape of the infrared spectrum in Figure 5.5. The centre frequency for the homogeneous electric field is marked by the grey dashed line. For blue-detuned laser

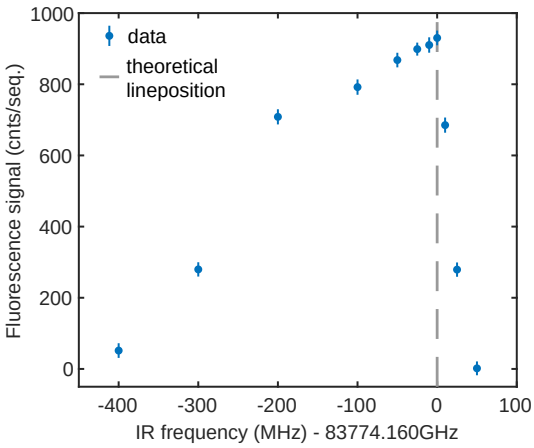

Figure 5.5: IR spectrum of the $\tilde{X}^1A_1 \leftarrow \tilde{X}^1A_1$ 5^1_0 $|2,2,0\rangle \leftarrow |3,3,0\rangle$ transition used for optical pumping to the $|1,1,0\rangle$ state. The dashed line indicates the transition frequency for the homogeneous electric field value in the trap of 628 $\frac{\mathrm{V}}{\mathrm{cm}}$. The asymmetric shape of the transition is determined by the electric field distribution in the electric trap and the negative differential Stark shift between initial and final state.

frequencies the signal quickly drops because due to the electric field distribution in the trap there is only limited possibility to drive the transition in lower electric fields. For red-detuned frequencies the transition can still be driven due to the existence of higher electric fields in the trap, however, with decreasing strength as the probability for molecules to be in these fields also decreases.

MW coupling between the $|1,1,0\rangle$ and $|1,1,1\rangle$ doublet The state $|1,1,0\rangle$ is only one of the two states that form the ortho ground state doublet. The second state $|1,1,1\rangle$ has a negative Stark shift and is not trapped. Therefore, the molecules transferred into this state, which are about half of the molecules decaying towards J=1 as can be seen from Figure 5.2, are quickly lost from the trap and cannot be detected. A way to visualise the state $|1,1,1\rangle$ is by coupling the molecules prepared via optical pumping in the $|1,1,0\rangle$ state to the $|1,1,1\rangle$ state with microwaves. The result of this measurement is shown in Figure 5.6. The amount of signal measured in the $|1,1,0\rangle$ state without applying microwaves is indicated by the red baseline. When applying microwaves two pronounced dips appear as the molecules are transferred to the two M-sublevels of the $|1,1,1\rangle$ state. Both states are untrapped so that the molecules are quickly lost from the trap resulting in a decrease of the LIF detection signal. The splitting between the two lines is determined by the electric field in the trap and the theoretical line positions for an electric field of 628 $\frac{\mathrm{V}}{\mathrm{cm}}$ are indicated. The width of the two transitions is again determined by Stark broadening, and therefore the electric field distribution in the trap. The difference in depth between the two lines is most likely caused by different coupling efficiencies of the microwaves into the electric trap resulting in different effective power levels. This effect can also distort the lineshape of the transitions.

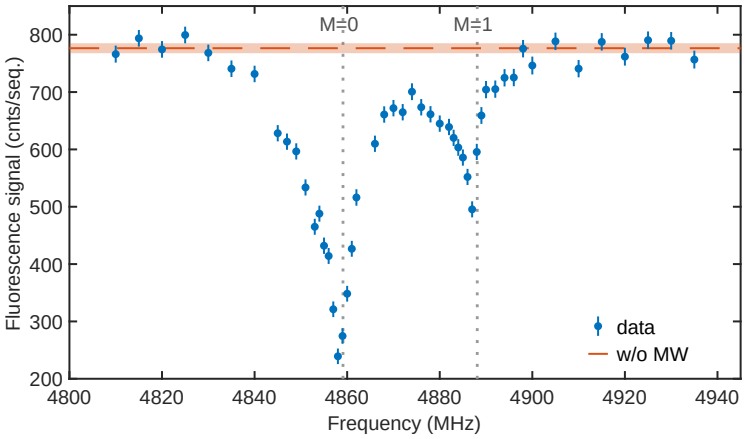

Figure 5.6: MW spectrum of the $|1,1,1\rangle \leftarrow |1,1,0\rangle$ transition. Molecules transferred from the initial state $|1,1,0\rangle$ into the untrapped M-sublevels of the $|1,1,1\rangle$ state are quickly lost from the trap resulting in a decrease in signal. The theoretical line positions for an electric field of 628 $\frac{\mathrm{V}}{\mathrm{cm}}$ are marked.

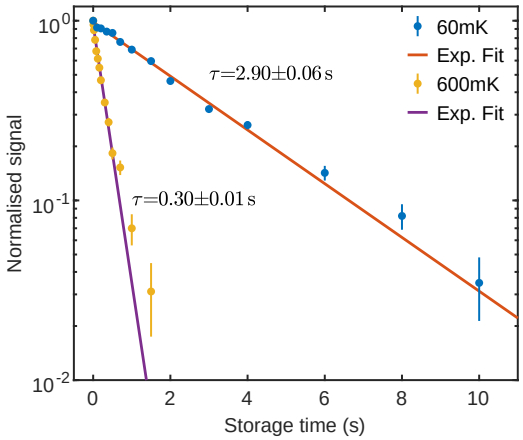

Figure 5.7: Trap lifetime of molecules in the $|1,1,0\rangle$ state. The sample at 600 mK is loaded directly into the trap without cooling applied. The colder sample at 60 mK enters the trap in the states $|3,3,0\rangle$ and $|4,3,1\rangle$ where the molecules are Sisyphus cooled and then transferred to the $|1,1,0\rangle$ state by optical pumping.

Trap lifetime increase from cooling As a final measurement the trap lifetime of warm and cold molecules is compared. Warm refers to a molecule sample loaded into the trap without applying any cooling which is not possible for molecules in the $|1,1,0\rangle$ state with the standard cooling scheme at hand due to the lack of a second trapped M-sublevel. As mentioned before, these molecules have a temperature of about 600 mK. Cold molecules are prepared in the $|1,1,0\rangle$ state by the optical pumping technique presented here after cooling them by optoelectrical Sisyphus cooling down to a temperature of about 60 mK. A measurement of the trap lifetime for these two molecule samples is shown in Figure 5.7. The measurement is performed by storing the molecules for a certain amount of time without applying

any radiation and then unloading and detecting them. The amount of molecules left in the trap decays exponentially with time. The colder molecules have the clear advantage that the trap lifetime is considerably longer with (2.90 ± 0.06) s compared to a lifetime of (0.30 ± 0.01) s for the uncooled sample. This lifetime is much shorter than for the state $|3, 3, 0\rangle$ due to the much larger K-type doubling and the involved quadratic Stark shift which facilitates losses via Majorana flips.

The optimal duration for an efficient preparation of molecules in the ortho ground state $|1, 1, 0\rangle$ depends on the saturation time of the optical pumping and the trap lifetime. The value giving the highest number of ground state molecules lies around 0.75 s. For longer times the signal starts to decrease again due to the trap lifetime.

6 Observation of coherence on rotational states

For almost any applications of molecules in quantum information technology and also high precision spectroscopy (see Sec. 1.1) it is indispensable to have long coherence times between different states. However, the Stark and Zeeman shift of molecules can lead to temporal and spatial variation of transition frequencies and hence destroy coherence. Many times, in particular for atoms, this problem is addressed by using clock transitions for which at certain 'magic' electric or magnetic field values the Stark or Zeeman shift has equal slopes in the involved states, making the transition frequency independent of the applied external field. A caveat of these transitions typically is, that a specific field value has to be applied leading to broadening for field distributions of finite width.

In this chapter rotational states in molecules are discussed which represent a hidden degree of freedom in the molecule. The states are completely degenerate for arbitrary electric field values and can in this regard be seen as ideal clock states to each other. First measurements are presented that allow to experimentally distinguish the two states and a coherence time of $>130\,\mu s$ between these states is determined for cold formaldehyde molecules. The results rely on both of the main results given in the previous chapters, i.e. the state selectivity of the detection method and the ability to prepare cold Sisyphus cooled molecules in their rotational ortho ground state. The chapter is structured as follows. First, the theoretical properties of the states are presented in Section 6.1 together with a means to distinguish them, and the main sources of decoherence that are to be expected are discussed. In Section 6.2 follows a description of the experimental sequence together with fundamental measurements necessary for the interpretations of the coherence measurements which are presented in Section 6.3 for uncooled as well as cooled molecule samples. Finally, the chapter concludes with an outlook on how the coherence time can be further increased in Section 6.4.

6.1 Theoretical background

All rotational sublevels of formaldehyde with $M \neq 0$ are doubly degenerate in $\pm M$ as is already mentioned in Section 2.1.4. Both states correspond to molecules with the same orientation with respect to the external electric field, defining the quantisation axis, but rotating in opposite directions as illustrated in Figure 6.1. They show identical behaviour as long as the total quantum system, consisting of molecule and environment, is invariant under time reversal symmetry. Electric fields are even under time reversal which is why the states are degenerate for arbitrary electric fields. Hence they can be seen as ideal clock states with respect to each other

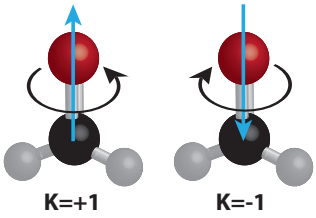

Figure 6.1: Illustration of formaldehyde molecules rotating in opposite directions. These two rotational states are exactly degenerate in electric fields and the degeneracy is only lifted by e.g. magnetic fields.

in this regard. Magnetic fields however, are odd under time reversal and lift the degeneracy via the Zeeman shift which is proportional to the quantum number M (see Equation (2.19)). But as explained previously, for closed shell molecules the Zeeman interaction is generally very weak and suppressed by about a factor of 10^3 compared to typical atoms (see Section 2.1.4). This results in a sensitivity on the order of $\frac{\text{kHz}}{\text{G}}$. However, compared to atomic clock states where magic transitions are used to cancel the first order Zeeman shift, molecular states are still about 10^4 to 10^5 times more sensitive [Sár14, Bot19]. Nonetheless, the molecular states under investigation here are ideal candidates for quantum information processing experiments with molecules as they require no electric field control and strongly reduced effort to suppress external magnetic fields.

In order to distinguish both states a straightforward approach would be using σ^+ and σ^- light to selectively drive transitions. However, due to the existence of electric fields in the trap pointing in all three dimensions and insufficient optical access this is not possible. Therefore, this section first provides a theoretical description of the physical effect allowing to distinguish the individual states of the typically degenerate states via the occurrence of dark states in Section 6.1.1. This also enables the coherence time measurements presented later on in this chapter. Furthermore, the anticipated decoherence mechanisms of the system are described in Section 6.1.2.

6.1.1 Emergence of dark states

In a three level system, where two excited states are coupled to a third ground state by an external radiation field, the eigenstates of the Hamiltonian including the coupling field are superpositions of the excited states [Scu97, Mar01]. If the excited states are degenerate the resulting superpositions are symmetric and antisymmetric combinations of the two bare excited states in the absence of a coupling field. The ground state does not contribute to these superposition states. This gives rise to a decoupling of one of the superposition states such that this states becomes a *dark* state whereas the other superposition states is coupled to the ground state and thus is a *bright* state. This behaviour is well known in the atomic community in particular in the context of coherent population trapping [Ari76].

In formaldehyde molecules such a system can be implemented in the form of three M-sublevels of rotational states with M=0, ±1. Here, an obvious choice is the ortho ground state $|1,1,0\rangle$ due to a lack of other interfering sublevels with

higher M. According to Equation (2.8) asymmetric rotor states are a combination of symmetric rotor states, however, the composition depends on the applied electric field:

$$M = 1 \quad : \qquad |\Psi^{\text{asym}}_{1,1,0,1}\rangle = \frac{1}{\sqrt{2\,(1+\epsilon^2)}} \left[(1-\epsilon)\,|\Psi^{\text{sym}}_{1,1,1}\rangle - (1+\epsilon)\,|\Psi^{\text{sym}}_{1,-1,1}\rangle\right], \quad (6.1a)$$

$$M = 0 \quad : \qquad |\Psi^{\text{asym}}_{1,1,0,0}\rangle = \frac{1}{\sqrt{2}} \left[|\Psi^{\text{sym}}_{1,1,0}\rangle - |\Psi^{\text{sym}}_{1,-1,0}\rangle\right], \quad (6.1b)$$

$$M = -1 : \qquad |\Psi^{\text{asym}}_{1,1,0,-1}\rangle = \frac{1}{\sqrt{2\,(1+\epsilon^2)}} \left[(1+\epsilon)\,|\Psi^{\text{sym}}_{1,1,-1}\rangle - (1-\epsilon)\,|\Psi^{\text{sym}}_{1,-1,-1}\rangle\right] \quad (6.1c)$$

with the asymmetric rotor states $|\Psi^{\text{asym}}_{J,K_a,K_c,M}\rangle$, the symmetric rotor states $|\Psi^{\text{sym}}_{J,K,M}\rangle$ and an electric field dependent parameter $0 \leq \epsilon \leq 1$. In the presence of an external RF-field coupling the sublevels with $M = \pm 1$ to the sublevel with M=0, the eigenstates of the Hamiltonian describing the system are:

$$|\Psi^{\text{sup}}_{\pm}\rangle = \frac{1}{\sqrt{2}} \left[|\Psi^{\text{asym}}_{1,1,0,1}\rangle \pm e^{-\mathrm{i}2\phi}\,|\Psi^{\text{asym}}_{1,1,0,-1}\rangle\right], \quad (6.2)$$

with the phase ϕ determined by the polarisation of the coupling RF-field[1]. The M=0 sublevel $|\Psi^{\text{asym}}_{1,1,0,0}\rangle$ is not affected by the coupling RF-field and is still an eigenstate. The transition matrix elements between the superposition states $|\Psi^{\text{sup}}_{\pm}\rangle$ and the state $|\Psi^{\text{asym}}_{1,1,0,0}\rangle$ can easily be determined via the direction cosine matrix elements [Tow75]. It becomes apparent that the superposition state $|\Psi^{\text{sup}}_{+}\rangle$ is a bright state and no transition occurs for state $|\Psi^{\text{sup}}_{-}\rangle$ which therefore is dark:

$$\langle\Psi^{\text{sup}}_{\pm}|\mu|\Psi^{\text{asym}}_{1,1,0,0}\rangle = 1/0. \quad (6.3)$$

The wavefunctions of the M=0 sublevels of an asymmetric rotor themselves are symmetric and antisymmetric superpositions of the two M=0 sublevels of the corresponding symmetric rotor with $K = \pm K_a$ as can be seen in Equation (6.1b). Therefore, for the lower state of the doublet the wavefunction can be expressed as:

$$|\Psi^{\text{asym}}_{1,1,1,0}\rangle = \frac{1}{\sqrt{2}} \left[|\Psi^{\text{sym}}_{1,1,0}\rangle + |\Psi^{\text{sym}}_{1,-1,0}\rangle\right]. \quad (6.4)$$

This expression implies that for a transition from the superposition states in Equation (6.2) to this M=0 sublevel of the lower state of the doublet, $|J{=}1, K_a{=}1, K_c{=}1\rangle$, the opposite applies than for the transition into the M=0 sublevel of the upper state investigated in Equation (6.3), meaning that the transition from the antisymmetric superposition is possible whereas the state is dark for the symmetric superposition.

This behaviour gives a very convenient experimental handle on how to distinguish the rotational sublevels. It also motivates the choice of the $|1,1,0\rangle$ state for the experiments presented in this chapter. In principle, the same behaviour is found for the three level systems formed by the M=0 and $M = \pm 1$ states for any other choice

[1] Assuming an arbitrary polarisation $E_x\hat{x} + E_y e^{\mathrm{i}2\theta}\hat{y}$ perpendicular to the direction of the electric field z, the phase ϕ is given by $\phi = \pi - \mathrm{i}\frac{1}{2}\log\left(-\frac{E_x + \mathrm{i}E_y\exp(\mathrm{i}2\theta)}{E_x - \mathrm{i}E_y\exp(\mathrm{i}2\theta)}\right)$

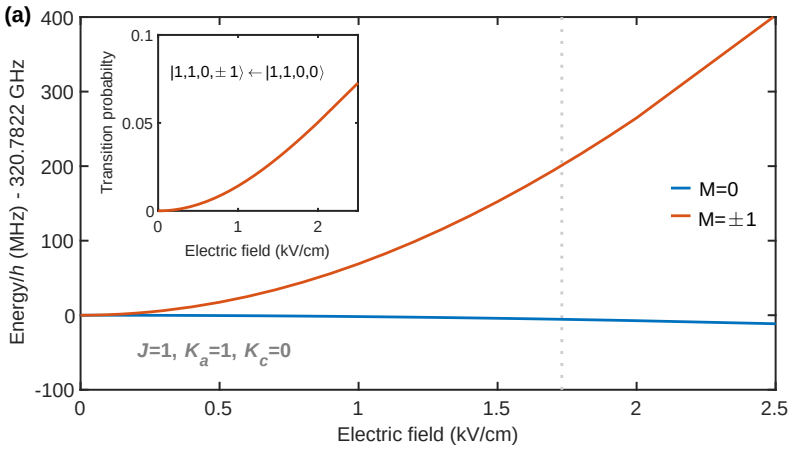

Figure 6.2: Stark shift of the $|1,1,0\rangle$ state. The inset shows the relative transition probability for transition between M=1 and M=0. The dashed line indicates an electric field value of 1731 $\frac{\mathrm{V}}{\mathrm{cm}}$ which is where the electric trap is operated for the experiments in this chapter (see Section 6.2.1). An overview over the Stark shift and the transition probabilities of the $|1,1,0\rangle$ state which also includes the $|1,1,1\rangle$ state is given in Figure 2.3.

of J and K. However, only for J=1 it is ensured that all molecules in the trap with J=1 populate the correct sublevels with M=±1, due to these levels being the only trapped states with a positive Stark shift. This allows neglecting any higher M-sublevels for which the method presented here to produce bright and dark states does not work. Furthermore, uncooled and also cooled molecules are readily available due to the technique developed in the last chapter.

Properties of the $|1,1,0\rangle$ state The Stark shift and transition probabilities for the $|1,1,0\rangle$ and $|1,1,1\rangle$ doublet are already shown in Figure 2.3. In Figure 6.2 the low electric field part of the figure is reproduced for the upper state of the doublet. Due to the large K-type doubling splitting of 4.830 GHz the Stark shift is quadratic in this electric field regime. This fact is also represented in the transition probability shown in the inset of Figure 6.2 for a transition between the M-sublevels of the $|1,1,0\rangle$ state, which is is very small for low electric fields. Therefore, a high offset field has to be applied to the electric trap to increase this transition probability. However, for higher electric fields also the transition frequency between the M-sublevels is larger, resulting in less effective RF power to drive the molecules (see Section 2.2.2). Furthermore, it has to be kept in mind that the transition from $|1,1,0\rangle$ to $|1,1,1\rangle$ is also affected. Here, the transition probability decreases with higher electric field. However, more importantly the effective radiation power in the trap is much lower due to the large frequency caused by the K-type doubling splitting and becomes even lower for higher frequencies, i.e. higher electric fields. For these reasons, a compromise has to be found when choosing the electric field of the trap in which the transitions between the various sublevels of $|1,1,0\rangle$ and $|1,1,1\rangle$ are driven. The electric field value chosen for the experiments in this chapter is 1731 $\frac{\mathrm{V}}{\mathrm{cm}}$ (see Section 6.2.1) which results in a frequency for the transition from the $M=\pm 1$ to the M=0 sublevel of the state $|1,1,0\rangle$ of 211.3 MHz and a frequency of

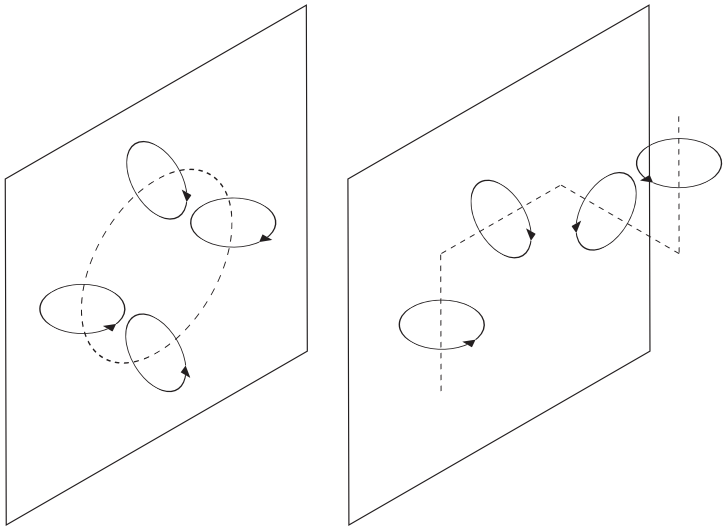

Figure 6.3: Illustration of dephasing caused by geometric phases. In the left panel the situation for molecules moving in an electric field only varying within a single plane is illustrated. The point of constant phase symbolised by the arrowhead is not affected. In the right panel the electric field also varies in the third dimension which can lead to dephasing.

5041.9 MHz for the transition to the M=0 sublevel of the lower state of the doublet $|1,1,1\rangle$.

6.1.2 Sources of decoherence

In this section the major anticipated sources of decoherence between the two $M=\pm 1$ sublevels of the ortho ground state $|1,1,0\rangle$ are discussed.

Geometric phases The quantisation axis of the molecules is provided by the electric field in the trap. The direction of the axis is therefore quite uniform for the homogeneous field in the centre of the trap. However, for the trapping fields in the border region there are also strong electric fields along the remaining two dimensions as can be seen from the sketch of the trap in Figure 2.6. This leads to dephasing of the rotation of different molecules due to the collection of geometric phase while the molecules move through electric fields of different orientation. An illustration of this process is provided in Figure 6.3. In the left panel the case for an electric field only changing within a single plane is shown. The dashed circle indicates how the direction of the quantisation axis changes within the plane and the solid circles represent the rotation of the molecules. A point of constant phase is marked by an arrowhead. As can be seen, the rotation stays in phase independent of the change of direction of the electric field within the plane, once the molecule is again in a field of the initial orientation. This situation changes for an electric fields also exploring the third dimension and pointing out of the plane as is illustrated in the right panel of Figure 6.3. Here, the point of constant phase does not coincide with the original orientation after a molecule has passed through all three possible orientations of the electric field. As a consequence, molecules that probe the border region of the

$\|J{=}1, K_a{=}1, K_c{=}0, M_J{=}0\rangle$		$\|J{=}1, K_a{=}1, K_c{=}0, M_J{=}\pm 1\rangle$	
$F = 1,\ M_F = \pm 1$	4.9 kHz	$F = 1,\ M_F = 0$	8.5 kHz
$F = 2,\ M_F = 0$	−0.4 kHz	$F = 2,\ M_F = \pm 1$	4.5 kHz
		$F = 2,\ M_F = \pm 2$	1.2 kHz
		$F = 0,\ M_F = 0$	−2.5 kHz

Table 6.1: Hyperfine splitting of the $|1, 1, 0\rangle$ state. The deviations of the hyperfine sublevels of $|1, 1, 0\rangle$ from the centre frequency of the corresponding M_J-sublevels are given for an electric field strength of 1731 $\frac{\mathrm{V}}{\mathrm{cm}}$. The states are described using the quantum number $F{=}J{+}I$ consisting of the coupling of the angular momentum of rotation J and the total spin of the proton I. However, it is important to note that for sufficiently strong electric fields F is not a good quantum number any more as the coupling of J and I is broken. The splittings are calculated using the free software package PGOPHER [Wes17].

electric trap, where electric fields pointing in directions perpendicular to the one of the homogeneous electric field in the centre of the trap are much more prevalent, are likely to have lost all coherence after reflection at the trap wall. A possible circumvention of this problem in the presently at the experiment employed trap is outlined in Section 6.4. For the experiments presented in this work the consequence is that the maximum coherence time achievable is limited by the time the molecules need to cross from one side of the trap to the other. This time depends on the velocity of the molecules, and therefore their temperature. There are two different molecule samples used for the experiments presented here, one consists of molecules which are already in the state $|1, 1, 0\rangle$ during loading of the trap, the other one is first Sisyphus cooled in the states $|3, 3, 0\rangle$ and $|4, 3, 1\rangle$ to a final cooling frequency of $f_{\mathrm{RF}} - f_{\mathrm{offset}} = 725\,\mathrm{MHz}$ and then transferred to the $|1, 1, 0\rangle$ state via optical pumping as laid out in Chapter 5. The velocities of these samples are determined by time of flight measurements to be about 13 $\frac{\mathrm{m}}{\mathrm{s}}$ and 4.3 $\frac{\mathrm{m}}{\mathrm{s}}$ respectively. Taking into account the size of approximately 1.5 mm of the homogeneous field region of the electric trap along the direction perpendicular to the microstructured capacitor plates forming the trap, this results in a maximum coherence time due to the velocity of the molecules of about 100 µs for the warmer sample and 350 µs for the cooled sample.

Hyperfine structure The state $|1, 1, 0\rangle$ exhibits hyperfine structure as explained in Section 2.1.3 which means that instead of only three sublevels with $M{=}0, \pm 1$ the state $|1, 1, 0\rangle$ actually consists of a total of nine sublevels with $F = 0, 1, 2$ and their corresponding M_F substates. In Table 6.1 the hyperfine splittings, i.e. the deviation from the centre frequencies of the states without hyperfine structure, are listed for the M-sublevels of the $|1, 1, 0\rangle$ state in an electric field of 1731 $\frac{\mathrm{V}}{\mathrm{cm}}$. The choice of the electric field is motivated by the experimental parameter as explained in Section 6.1.1. The hyperfine energies are calculated with the free software package PGOPHER [Wes17] which employs the treatment given in Section 2.1. Due to the hyperfine structure there are various transition frequencies involved resulting

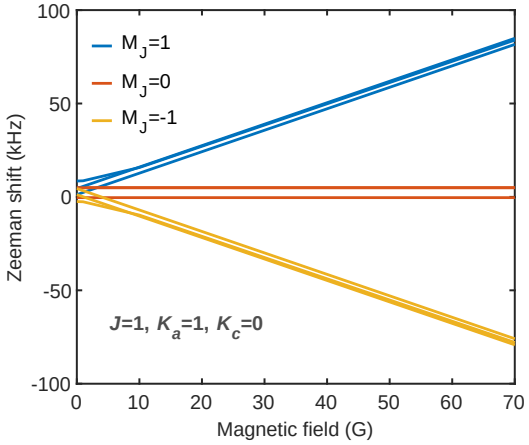

Figure 6.4: Zeeman shift of the M-sublevels of the $|1,1,0\rangle$ state including hyperfine sublevels. The states with M_J=±1 shift with a rate of $\pm 1.15\,\frac{\mathrm{kHz}}{\mathrm{G}}$ with the magnetic field. The curves are calculated using the molecular g-factor given in Ref. [Hüt68] using the treatment in Section 2.1.4. The electric field is assumed to be zero or oriented in parallel to the magnetic field.

in dephasing, and therefore decoherence. The mean deviation of the transition frequencies weighted with the individual transition moments which are also taken from the software PGOPHER is 2.6 kHz, which in turn signifies that the states get a unity phase shift on a time scale of 61 µs and therefore decohere. However, this situation changes in the presence of magnetic fields which also affect the size of the hyperfine splitting.

Magnetic fields As already mentioned, pairs of sublevels with the same absolute value of M are only degenerate in electric fields. Their energy separation is still sensitive to magnetic fields, even though about a factor of 10^3 less than for typical atoms. An expression for the Zeeman interaction is provided in Section 2.1.4 in Equation (2.19). The effect on the M-sublevels of the $|1,1,0\rangle$ state is plotted in Figure 6.4. The M=0 sublevel is not affected by the magnetic field whereas the M=1 and M=−1 sublevels are shifted to higher and lower energies respectively with a rate of $1.15\,\frac{\mathrm{kHz}}{\mathrm{G}}$. The hyperfine components of the individual sublevels are also shown in the plot. However, already for very small magnetic fields the coupling between J and I is broken and the Paschen-Back regime is entered. The hyperfine splitting is reduced and also the transition moments are altered in this regime giving only a mean deviation of about 1.9 kHz[2] increasing the limit for the expected coherence time due to hyperfine structure to about 85 µs. When an additional electric field is applied the resulting Stark shift can be added to the Zeeman shift as long as both fields are oriented in parallel. If the fields are not parallel the situation is more complex as is already mentioned in Section 2.1.4 and the shift in Figure 6.4 can only be a rough approximation. The Zeeman shift of the molecules does not per se introduce decoherence it rather leads to Larmor precession between the M-sublevels

[2]Weighted by the individual transition moments calculated with PGOPHER [Wes17]

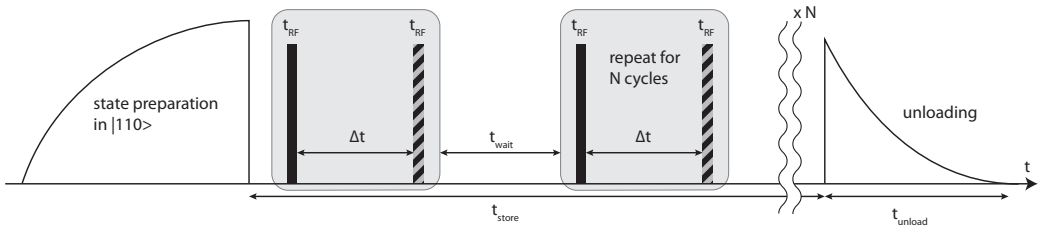

Figure 6.5: Sketch of the experimental sequence. Molecules are prepared in the $|1,1,0\rangle$ state by either directly using molecules loaded in this state or transferring previously Sisyphus cooled molecules via optical pumping. During the storage time t_{store} a pair of RF pulses of length t_{RF} and time separation Δt can be applied to the molecules where the second pulse is optional. This pulse sequence is repeated for a number of N cycles during the storage time with an appropriate waiting time t_{wait} between the cycles to allow for reshuffling of the molecules within the trap. Finally the molecules are unloaded for an unloading time t_{unload}. The signal is integrated over the unloading curve.

split up by the magnetic field. This way the two M-sublevels are converting into each other. However, this process does not necessarily affect the coherence as long as the magnetic field is homogeneous over the trap volume. Due to the large size of the electric trap and a lack of any measures for magnetic shielding it is likely that there is an inhomogeneous magnetic field background. Assuming a rather high inhomogeneity of about the size of the earth magnetic field of 0.3 G, this results in a maximum shift of 0.7 kHz corresponding to a coherence time of about 220 µs for a unity phase shift.

6.2 Experimental fundamentals

In this section the experimental foundation for the coherence measurements between rotational states of formaldehyde presented in this chapter is set. First, the experimental sequence is introduced in Section 6.2.1 followed by a discussion of the influence of the electric field distribution in Section 6.2.2. In Section 6.2.3 a fundamental requirement for a coherence measurement is proven, namely the possibility to address individual molecules twice in the trap within the expected coherence time.

6.2.1 Experimental sequence

The experimental sequence for the experiments presented in this chapter is illustrated in Figure 6.5. First, a molecules sample in the ortho ground state $|1,1,0\rangle$ is prepared for which there are two different options. The first alternative are uncooled molecules for which the trap is loaded for 1.5 s and only the molecules that already occupy the $|1,1,0\rangle$ state are detected. This results in a molecule sample with a temperature of about 600 mK with a mean velocity of $(12.9 \pm 0.2)\,\frac{\mathrm{m}}{\mathrm{s}}$. The second alternative are Sisyphus cooled molecules. Here, first the standard optoelectrical Sisyphus cooling sequence (see Section 2.2.1) is applied to a final frequency of in this case $f_{\mathrm{RF}} - f_{\mathrm{offset}} = 725$ MHz. Since the cooling only incorporates molecules occupying the states $|3,3,0\rangle$ and $|4,3,1\rangle$ subsequently those are transferred to the

ortho ground state $|1,1,0\rangle$ with the sequence described in Chapter 5. The resulting molecule sample has a temperature of 60 mK and a mean velocity of $(4.3 \pm 0.3)\,\frac{\mathrm{m}}{\mathrm{s}}$. The molecules are stored for the time t_{store} which ranges from 45 ms to 100 ms for the different measurements performed. During the storage time a sequence of RF or MW pulses is applied to drive the transition from the trapped $M{=}\pm1$ sublevels of the $|1,1,0\rangle$ state to the untrapped $M{=}0$ sublevels of the $|1,1,0\rangle$ and $|1,1,1\rangle$ state. The typical pulse length t_{RF} varies between 5 µs and 500 µs. For some measurements a second pulse is applied a time Δt after the first pulse (see Section 6.2.3). To improve statistics, an experiment, i.e. an RF pulse or a pair of RF pulses, can be applied several times for the same molecules sample without unloading the trap and refreshing the molecules sample. To do so an appropriate storage time t_{wait} is incorporated to allow reshuffling of the molecules within the trap before the next set of pulses is applied. This process is repeated for a number of N cycles. The reason for this is that not all molecules in the trap can be addressed at the same time by a single pulse due to the inhomogeneous fields in the trap (refer to Section 6.2.2). The time t_{wait} necessary for sufficient reshuffling is dependent on the velocity of the molecules and for measurements with uncooled molecules a minimum waiting time of 2 ms is chosen whereas for cold molecules the time is increased to at least 3 ms. Finally, the molecules are unloaded for a time t_{unload} of 1 s for uncooled molecules and 4 s for cooled molecules and detected by the LIF detection setup with the UV laser tuned to the detection transition for the $|1,1,0\rangle$ state. The total signal extracted consists of the integrated fluorescence signal over the unloading time.

During the storage time the offset electric field is increased to an electric field strength of 1731 $\frac{\mathrm{V}}{\mathrm{cm}}$. The reason for this lies in the transition probability and the effective available RF power as previously mentioned and a good compromise resulting in the largest effective power for the involved transitions is achieved for the chosen field strength. The precise value of the field strength is only determined by theory according to the applied voltage configuration. The actual value probably deviates by about 1 to 2 % due to experimental imperfections. However, the precise value is of no importance as the resulting transition frequencies can be determined by depletion spectroscopy. To do so, uncooled molecules are prepared in the trap and stored for 50 ms. During the storage time single RF pulses of length $t_{\mathrm{RF}}{=}10$ µs are applied driving the transition to the untrapped $M{=}0$ sublevels of the $|1,1,0\rangle$ and $|1,1,1\rangle$ states which are quickly lost from the trap. This cycle is repeated for a number of $N{=}100$ times within a sequence for increased statistics. Varying the frequency of the RF pulse results in a clear loss in signal for the transition frequency allowing its precise determination. The measurement is shown in Figure 6.6 and allows the extraction of the transition frequencies 211.3 MHz and 5041.9 MHz for the transitions to $|1,1,0\rangle$ and $|1,1,1\rangle$ respectively. The depletion signal far detuned from the transition line is still significant as can be seen from comparison with the data point taken without the application of RF. The reason for this behaviour is not entirely clear. Partly, it can be caused by the electric field distribution in the trap, discussed in more detail in the next section, which broadens the transition. The frequency spectrum of the applied RF pulses is rather clean, and therefore should not cause the off-resonant driving of the transition. However, for the measurements presented here no significant problem is to be expected by the fact that the baseline

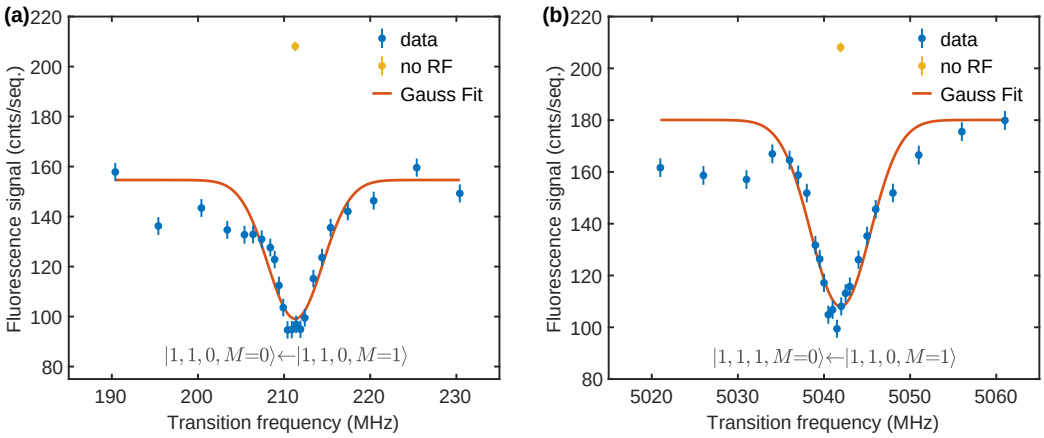

Figure 6.6: Depletion spectrum for the $|1,1,0\rangle$ state. Uncooled molecules are stored in the $|1,1,0\rangle$ state in the trap at an electric offset field of 1731 $\frac{\mathrm{V}}{\mathrm{cm}}$. A sequence of RF pulses is applied driving the transitions to the untrapped $M{=}0$ sublevels of the states $|1,1,0/1\rangle$. **(a)** The transition frequency to the $M{=}0$ sublevel of the state $|1,1,0\rangle$ can be determined to be 211.3 MHz by a Gaussian fit. **(a)** The transition frequency to the $M{=}0$ sublevel of the $|1,1,1\rangle$ state is 5041.9 MHz.

of the spectrum is shifted downwards.

6.2.2 Influence of the trap electric field distribution

Understanding the distribution of electric fields in the electric trap is crucial for an understanding of the measurements presented in this chapter. As already described in Section 2.2.2 the trap consists of a microstructured plate capacitor. An offset voltage applied to the capacitor plates creates a homogeneous electric field. Trapping voltages applied to neighbouring electrodes of the microstructure create a high electric field close to the surface of the plates confining the molecules. This trapping electric field decays exponentially towards the centre of the trap making the homogeneous offset field the only relevant contribution in the centre [Zep12]. The electric field probability distribution is shown in Figure 6.7. It shows a very narrow peak at an electric field of 1731 $\frac{\mathrm{V}}{\mathrm{cm}}$ which slowly decays towards higher and lower fields. The distribution is very asymmetric with higher fields being much more probable than lower fields due to the trapping electric fields confining the molecules. The curve is based on a numerical simulation, however, the shape of the field distribution has been experimentally confirmed numerous times [Glö16, Pre18].

Saturation with pulse length A first measurement to help understand the influence of the electric field distribution in the trap is the dependence of the amount of molecules removed from the trap on the length of the applied RF pulses. To this end, the experimental sequence described in a Section 6.2.1 is employed with a single pulse applied in each cycle whose length is varied. The maximum available RF power is chosen to achieve saturation of the molecule transition on a short time scale. The pulse is repeated for a number of $N{=}15$ cycles during each experimental sequence.

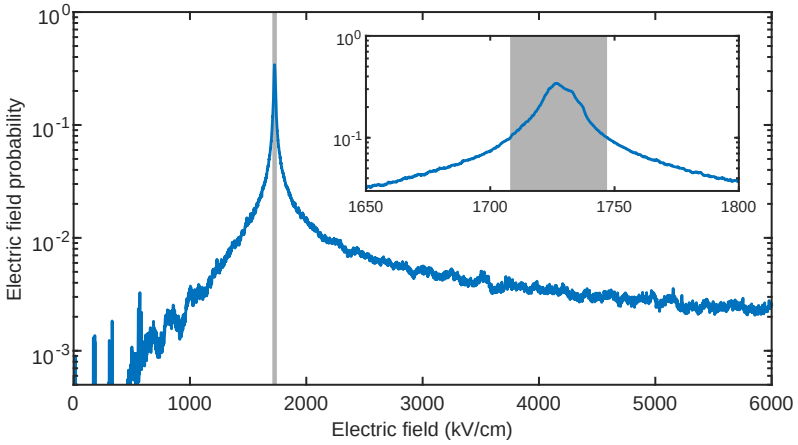

Figure 6.7: Electric field distribution. Probability distribution for the electric field in the trap simulated for an offset electric field of 1731 $\frac{\mathrm{V}}{\mathrm{cm}}$. The grey area indicates the electric fields addressed by a RF pulse frequency broadened to 10 MHz and corresponds to a trap volume of about 10 %. The inset shows a zoom onto the homogeneous electric field in the centre of the trap.

The measurement is performed for both transitions, i.e. driving the transition from the trapped $M=\pm 1$ sublevels of the $|1,1,0\rangle$ state to the untrappped M=0 sublevels of the $|1,1,0\rangle$ and $|1,1,1\rangle$ states with a transition frequency of 211.3 MHz and 5041.9 MHz respectively. The result of these measurements is plotted in Figure 6.8. For a transition frequency of 211 MHz the amount of molecules depleted from the trap follows a clear double exponential decay. This behaviour can be interpreted in the following way. At first, the molecules which are in the homogeneous electric field where the transition is resonant to the applied RF, are coupled to the untrapped M=0 state from where they are quickly lost. This process saturates on a time scale of about (4.3 ± 0.4) µs. The amplitude of this decay is $(77 \pm 2)\ \frac{\mathrm{cnts}}{\mathrm{seq.}}$ which is about 53 % of the total signal. With a number of N=15 cycles this corresponds to a depletion of about 4 % per pulse. This value can be understood when looking at the electric field distribution. The RF pulses are broadened to a width of about 10 MHz. This way they address most of the homogeneous electric field as indicated by the grey area in Figure 6.7. However, this area only corresponds to about 10 % of the total volume of the trap as can be determined by integrating over the full electric field distribution. These numbers are only rough estimates but are plausible when taking into account that only one fourth of the molecules located in an electric field addressed by the RF pulse can be depleted from the trap. A factor of $\frac{1}{2}$ arises from the fact that the molecules can only be equally distributed between the sublevels M=1 and M=0 because losses from the trap happen on a time scale much longer than the saturation time of the RF pulse. Another factor of $\frac{1}{2}$ stems from the consideration in Section 6.1 stating that each M=0 state of the doublet $|1,1,0/1\rangle$ is dark to half of the trapped molecules in the sublevels $M=\pm 1$ of the state $|1,1,0\rangle$.

The second and slower decay in Figure 6.8, after the immediate saturation of the molecule transition is caused by the movement of the molecules in the trap. While the RF radiation is applied the molecules keep moving within the trap so that mo-

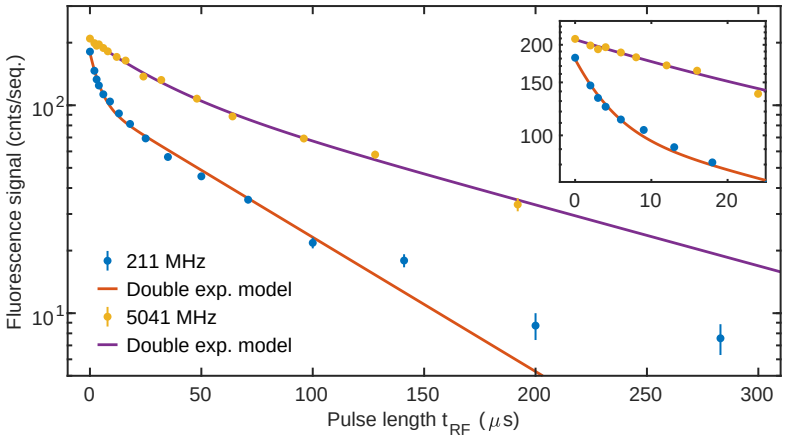

Figure 6.8: Saturation measurements for increasing pulse lengths. Uncooled molecules are prepared in the $M=\pm 1$ sublevel of the $|1,1,0\rangle$ state. RF pulses with a frequency of either 211 MHz or 5 GHz are applied for a number of N=15 times with varying pulse length t_{RF} driving the transitions in to the M=0 sublevels of the states $|1,1,0\rangle$ and $|1,1,1\rangle$ respectively. The initial fast decay results from a depletion caused by saturation of the transition of the molecules located in the homogeneous electric field of the trap addressed by the pulse. The slow decay results from movement of the molecules in the trap refreshing the molecules in the addressed fields. The inset shows a close up for short time scales.

lecules in the resonant homogeneous electric field volume are replaced. This means that more molecules can be addressed and transferred to the untrapped M=0 sublevel of the $|1,1,0\rangle$ state from where they eventually are lost. The decay happens on a time scale of (67 ± 3) µs microseconds which corresponds to a distance of 0.86 mm at the velocity of 12.9 $\frac{\mathrm{m}}{\mathrm{s}}$ of the molecules. Given the dimension of the homogeneous electric field of the trap this seems to be a reasonable result.

The transition into the M=0 sublevel of the state $|1,1,1\rangle$ at a transition frequency of about 5 GHz qualitatively shows a similar behaviour as can be seen from the second curve in Figure 6.8. However, the decay is much slower which is due to the amount of power available at this frequency or rather the low incoupling efficiency at high frequencies as has been mentioned earlier. Due to the slow saturation of the depletion signal in the homogeneous field, the movement of the molecules and the saturation can barely be separated. As a consequence, the measurements presented in the remaining part of the chapter can unfortunately not be performed on the transition between the $M=\pm 1$ sublevels of the $|1,1,0\rangle$ state to the M=0 sublevel of the $|1,1,1\rangle$ state.

The difference in signal between the two curves in Figure 6.8 which can be seen for zero pulse length is due to changing experimental conditions on different days and mainly caused by the molecule source and the available UV laser power for detection.

Saturation with RF power In order to further investigate the claims made in the previous paragraph, in particular about the movement of the molecules in the trap and the fraction of molecules addressed by the RF pulses, the power of the applied

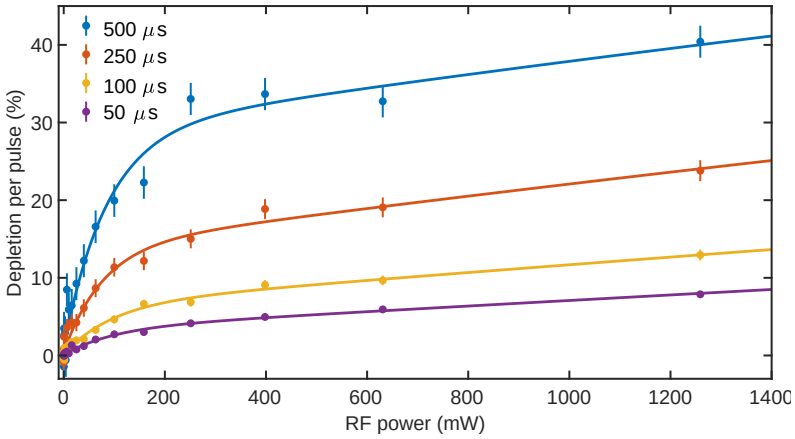

Figure 6.9: Power saturation measurement. Uncooled molecules are stored in the trap and RF pulses with a frequency of 211 MHz are applied leading to depletion of the molecules from the trap by driving the transition to the untrapped M=0 sublevel of the $|1,1,0\rangle$ state. With increasing RF power the depletion signal quickly saturates as the transition for the molecules in the homogeneous electric field region addressed by the pulse is saturated. The saturation level depends on the pulse length as for longer pulses the molecules move out of the centre part of the trap and are replaced by previously unaffected molecules.

RF pulses is varied. This measurement is performed under similar experimental conditions as the last measurement where the pulse length is varied. The transition at 211 MHz is driven for different pulse lengths and the result plotted in Figure 6.9. The pulse lengths are chosen such that for sufficient RF power the molecules in the homogeneous field of the trap can easily be saturated during the available time. The experiment is only performed with one cycle N=1 and instead of the measured fluorescence signal the depletion caused by every pulse is plotted. Again, a double exponential behaviour can be observed. The first initial fast increase in depletion signal, and hence decrease in the number of molecules in the trap, is again explained by the saturation of the transition of the molecules located in the homogeneous electric field part of the trap. The saturation value depends on the length of the applied pulse due to the movement of the molecules in the trap. For longer pulses the molecules in the addressed homogeneous electric field region are replaced by previously unaffected molecules so that a greater number of molecules can be depleted in total.

The length of the applied RF pulses is much longer than the time necessary to saturate the transition at higher power. Therefore, the saturation power does not depend on the pulse length because it can be assumed that the transition can be saturated for all molecules that enter the homogeneous field region during the time of the pulse. As a consequence, the power for saturation is not affected, only the number of molecules addressed, i.e. the amount of depletion.

The slow increase for higher power is most likely due to power broadening and off-resonant depletion of molecules in electric fields where they are not on resonance.

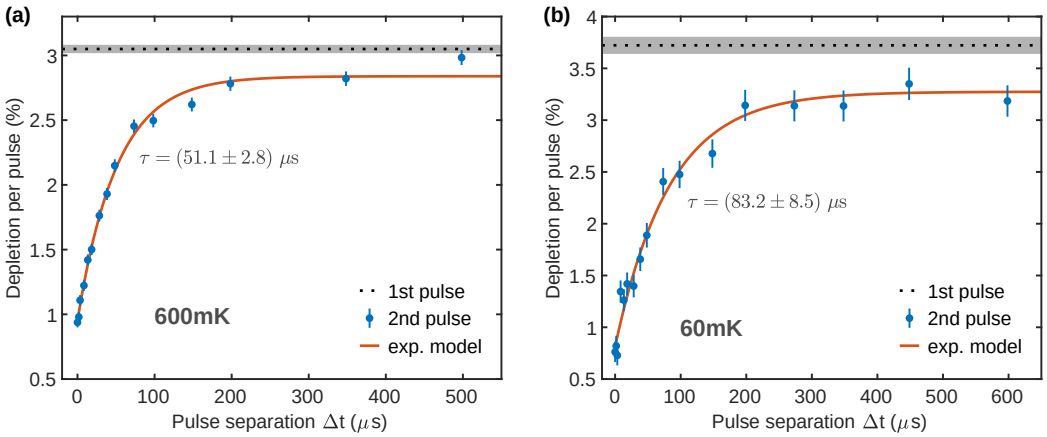

Figure 6.10: Effect of a second RF pulse on the molecules. Molecules are prepared in the $M{=}\pm1$ sublevels of the $|1,1,0\rangle$ state at a temperature of 600 mK **(a)** or 60 mK **(b)**. A first RF pulse with a frequency of 211 MHz is applied coupling the molecules to the $M{=}0$ sublevel, hence causing depletion as indicated by the dashed line. After the first pulse a second RF pulse is applied causing significantly less molecule depletion than the first pulse for short time scales. The amount of depletion rises due to the molecules moving in and out of the homogeneous electric field region addressed by the RF pulses.

6.2.3 Addressing the same molecule twice

For any coherence time measurement it is fundamental to be able to address a single molecule at least twice within the coherence time. The capability of the system and the measurement sequence to perform this task can already be deduced from the saturation behaviour of the pulse length variation measurement shown in Figure 6.8 and the power variation measurement in Figure 6.9. However, it is also possible to show this in a much more direct way. To this end pulses with the maximum available power and with a length of 5 µs are applied which according to the measurement in Figure 6.8 allows to saturate the transition for the molecules in the homogeneous field region. In contrast to previous measurements a second pulse is applied shortly after the first one as indicated in the description of the measurement sequence illustrated in Figure 6.5. The time separation Δt of the two pulses is varied and the amount of depletion of molecules from the trap caused by the second pulse is determined. The result is shown in Figure 6.10. The dashed line indicates the amount of depletion caused by the first pulse applied to a molecule sample that did not interact with a RF pulse shortly before. When the second pulse is applied, for very short time separations of only a few microseconds much less molecules are depleted by this second pulse than are depleted by the first pulse. The reason for this is that the first pulse already distributes the molecules equally between the upper trapped sublevel $M{=}\pm1$ and the lower untrapped sublevel $M{=}0$, meaning that applying another pulse does not affect this distribution anymore. For longer time separations Δt of the pair of pulses, the molecules that were addressed by the first pulse start to move out of the homogeneous field region and are replaced by molecules still unaffected by the RF. These molecules are all in the $M{=}\pm1$ sublevels and can again be transferred into the lower $M{=}0$ sublevel increasing the depletion caused by the second pulse.

This behaviour directly shows that molecules are addressed twice due to the different effect a second RF pulse applied shortly after the first one has on the number of molecules.

This effect is shown for uncooled molecules at a temperature 600 mK in Figure 6.10(a) and a cooled molecule sample at 60 mK in Figure 6.10(b). The rise constant extracted from an exponential saturation model fitted to the data is only about 60 % bigger for the colder molecules even though a factor of three is to be expected due to the three times larger velocity of the warmer sample. The reason for this behaviour is not clear. A possible influence of magnetic fields is discussed in the next section.

Another possible source of the rise in the depletion signal is decoherence. As explained in Section 6.1 the application of radiation creates superposition states so that only for half of the molecules the transition to the M=0 sublevel of the $|1,1,0\rangle$ state can be driven. The other half of the molecules can in turn only be transferred into the M=0 sublevel of the $|1,1,1\rangle$ state. The superposition state depleted by the first pulse can thus not only be repopulated by the movement of the molecules coming from other areas of the trap but also by decoherence, causing that molecules from the two distinct superposition states start to mix. However, from the present measurement it is impossible to distinguish this effect from the simple movement of the molecules within the trap.

For zero time separation of the pulses there is still a finite depletion signal caused by the second pulse. This is mainly caused by the finite length of the applied pulses. During the 10 µs for both pulses the curves are already expected to rise to about 0.5 % and 0.3 % for the cooled and uncooled molecule sample respectively. The remaining part of the depletion signal is most likely caused by the same experimental imperfections that cause the significant background to be seen in the spectra of Figure 6.6.

For long pulse separation times the signal does not rise to the same value of depletion as caused by the first pulse but instead to a slightly lower value. This could be caused by an insufficient time separation between the various cycles, which means that the individual pairs of pulses are not entirely independent from each other.

6.3 Observation of coherence

In order to see coherence between the two sublevels M=±1 the emergence of dark states when the three involved states are coupled by radiation is exploited (see Sec. 6.1). To this end, the degeneracy of the sublevels is lifted by applying a magnetic field leading to Zeeman splitting. The magnetic field is created by placing a coil on top of the vacuum chamber containing the electric trap. The coil has 224 windings with a diameter of about 23 cm. It is oriented in a plane parallel to the capacitor plates of the trap with a distance from the centre of the coil to the centre of the trap of 134 mm. This way, according to theory, an on-axis magnetic field of 3.48 $\frac{\mathrm{G}}{\mathrm{A}}$ is created at the position of the trap with a direction parallel to the homogeneous offset electric field in the trap. As mentioned before, a homogeneous magnetic field

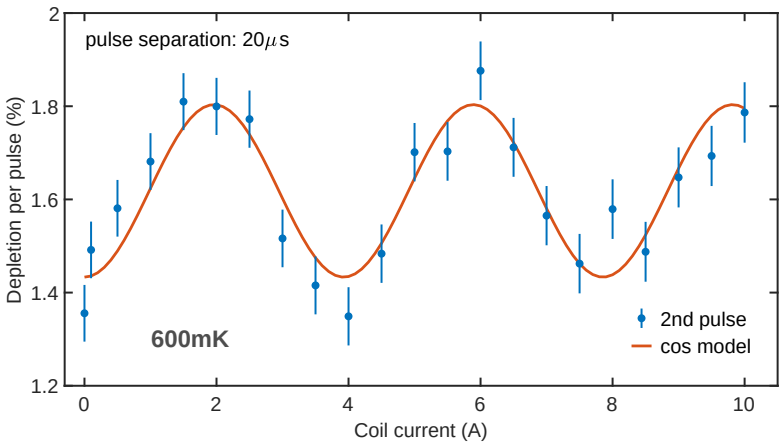

Figure 6.11: Magnetic field dependence of RF pulse pair measurement. Molecules at a temperature of 600 mK in the $|1,1,0\rangle$ state are depleted by a first RF pulse. A second RF pulse is applied after a time of 20 µs. Depending on the magnetic field given by the current through a coil the molecules Larmor precess during this time separation between the superposition states of the $M{=}\pm1$ sublevels of the $|1,1,0\rangle$ state so that the second pulse addresses more or less molecules accordingly. The data is fitted by a simple cosine model as guide to the eye.

does not lead to decoherence but rather produces an energy splitting between the $M{=}\pm1$ sublevels, i.e. the Zeeman splitting. This means that if there is an imbalance in the population of the two superposition states of the $M{=}\pm1$ sublevels and the population of the states becomes time and magnetic field dependent.

For a first investigation of this behaviour a measurement similar to the one presented in the last section is performed. Pairs of RF pulses with a length of 5 µs are applied with the difference that the time separation Δt is set to a fixed value of 20 µs and that a magnetic field is created by the coil. The measurement is performed for molecules without previous Sisyphus cooling, i.e. at a temperature of about 600 mK. The first pulse couples the molecules in one of the two superposition states to the $M{=}0$ sublevel of the $|1,1,0\rangle$ state and creates an equal distribution of the population between both states. In the time before the second pulse is applied the molecules Larmor precess depending on the applied magnetic field between both sublevels and the number of molecules that can be addressed with the second pulse changes. This behaviour and its dependence on the applied magnetic field, i.e. the current through the coil, is shown in Figure 6.11. The number of molecules addressed by the second pulse oscillates with the magnetic field as the molecules precess between the addressed superposition state and the dark state. This effect gives clear experimental evidence for the existence of both states and also shows that coherence persists between both states for a time larger than the pulse separation of 20 µs. Note that the measurement presented in Figure 6.11 was performed with a not yet final version of the coil creating the magnetic field. Therefore, the result cannot be quantitatively compared to the remaining measurements involving a magnetic field in the following part of this section.

For the determination of a coherence time, measurements for varying time sepa-

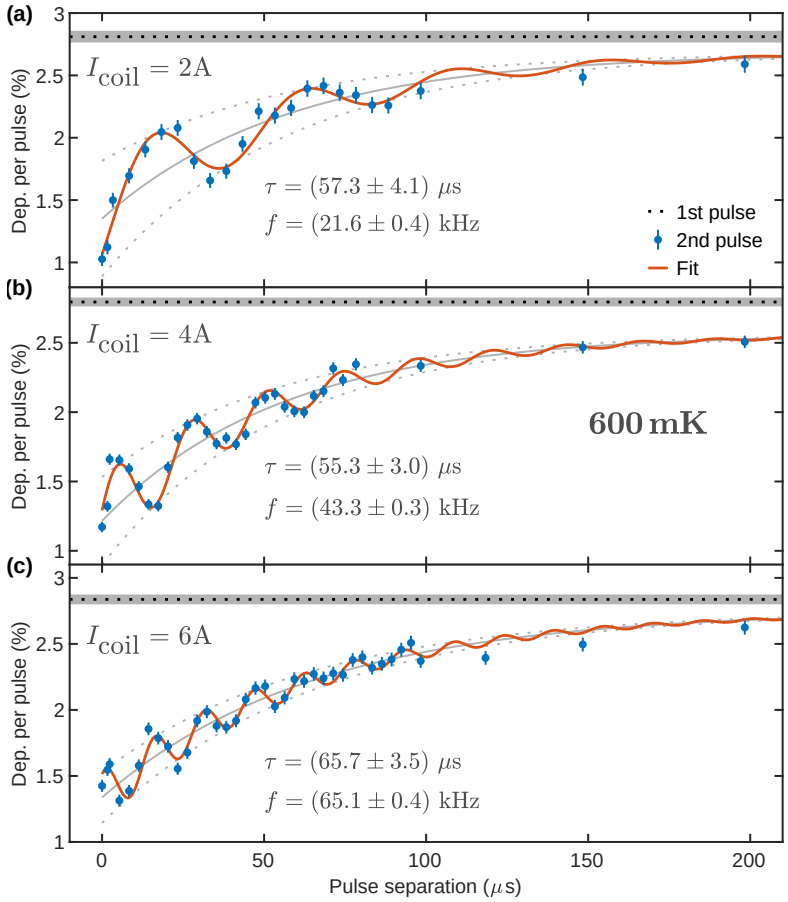

Figure 6.12: Observation of coherence between superposition states of the $M{=}\pm1$ sublevels of the $|1,1,0\rangle$ state at 600 mK. Molecules are prepared in the $|1,1,0\rangle$ state without Sisyphus cooling resulting in a temperature of 600 mK of the molecule sample. A first RF pulse of length 5 µs and frequency 211 MHz is applied and equally distributes the molecules between the arising superposition state $|\Psi_+^{\mathrm{sup}}\rangle$ and the $M{=}0$ sublevel of the $|1,1,0\rangle$ state. The second superposition state $|\Psi_-^{\mathrm{sup}}\rangle$ is left unaffected. The amount of depletion caused by the first pulse is indicated by the black dashed line. Subsequently a second RF pulse is applied with varying time separations between both pulses leading to further depletion. The measurements are performed for three different magnetic fields created by currents of **(a)** 2 A, **(b)** 4 A, and **(c)** 6 A through a coil on top of the vacuum chamber. The magnetic field causes the molecules to precess between the superposition states of the $M{=}\pm1$ substates resulting in oscillations in the depletion signal caused by the second pulse. An observed coherence time can be extracted from the oscillation as shown in the individual panels. This value includes the motion of the molecules in the trap.

rations Δt with applied magnetic fields are performed. Such a measurement for an uncooled ensemble of molecules at a temperature of 600 mK is shown in Figure 6.12 for different magnetic field strengths. The measurement sequence is the same as the one discussed in the last section. Again pairs of RF pulses of length 5 µs are applied for varying separation times Δt. The first pulse distributes the molecules between one superposition state and the $M{=}0$ sublevel of the $|1,1,0\rangle$ state. The

depletion in molecule signal by this first pulse is indicated by the black dashed lines. The second superposition state is the dark state and no population is driven to the M=0 sublevel by the RF pulse according to the arguments given in Section 6.1 as only a transition into the M=0 sublevel of the $|1,1,1\rangle$ state would be possible. With a magnetic field applied the molecules Larmor precess between both superposition states in the time between the first and second pulse. This way the number of molecules that can be addressed with the second pulse varies with time leading to oscillations in the depletion signal. This process is overlaid with the thermal movement of the molecules in the trap leading to an exponential saturation in the same way as without the presence of magnetic fields (see Figure 6.10). The data is again fitted by an exponential saturation model, however, overlaid by a damped oscillation. This allows to extract the oscillation frequencies given in the individual panels of Figure 6.12. The frequency rises linearly with the applied magnetic field as expected, but deviates by about 35 % from the calculated value when taking into account the Zeeman shift of the molecules as shown in Figure 6.4 and the magnetic field of the coil. The molecular g-factor is known much more precisely [Hüt68] making the magnetic field the most likely source of this discrepancy. It can only be measured in free space where it nicely agrees with the theoretical values for the given coil geometry. However, the magnetic properties of the vacuum chamber and other materials surrounding the trap can have an influence on the magnetic field at the position of the trap resulting in different values for the calculated and measured oscillations frequencies.

The time scale of the exponential saturation of the signal caused by the movement of the molecules and the time scale of the damping of the oscillation are not different with statistical significance. This behaviour is reasonable because the oscillations should disappear as the molecules addressed by the first pulse move out of the homogeneous field region. For this reason both time scales are described by a single free parameter in the fitted model. The extracted time scales agree quite well for the different magnetic fields, with the only value not overlapping within the $1\,\sigma$ error bars being the measurement at 6 A where the time scale deviates by about $2\,\sigma$. By combining the time scales to determine a coherence time a value of (59.4 ± 2.1) µs is extracted. The values are also consistent with the time scale of the measurement without magnetic field shown in Figure 6.10(a) with the measurement at 6 A again deviating the most by about $3\,\sigma$. The cause for the discrepancy might be that time constants for movement and decoherence, i.e. damping of the oscillation, are in fact not exactly the same as assumed in the model. It is important to emphasise that the measured time constants are not necessarily the coherence times between the different states. Since the damping of the oscillation is also caused by the movement of the molecules in the trap and both time constants cannot be separated, the obtained values can only be seen as a lower limit for the actual coherence time. The amplitude of the oscillation gets smaller for higher oscillation frequencies due to an averaging effect caused by the finite pulse length of 5 µs per pulse.

Similar measurements can be performed for a cold molecule sample at a temperature of 60 mK. The results for two different magnetic fields are plotted in Figure 6.13. As is to be expected the oscillation frequencies are in excellent agreement with the ones measured with uncooled molecule samples. The only difference lies in the decay

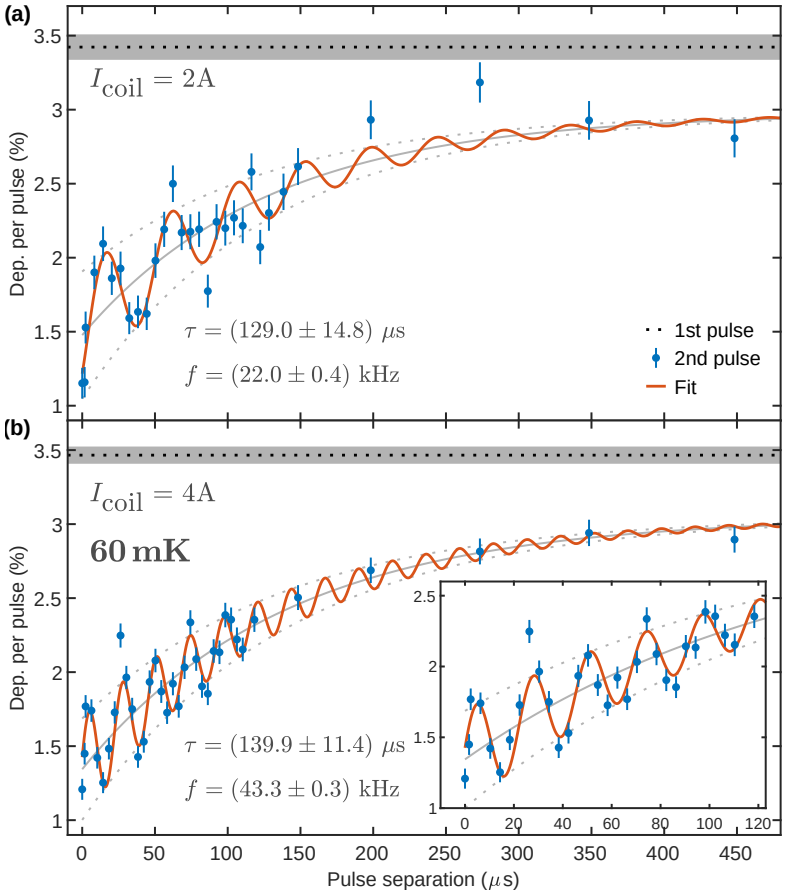

Figure 6.13: Observation of coherence between superposition state of the $M{=}\pm1$ sublevels of the $|1,1,0\rangle$ state at 60 mK. Molecules are prepared in the 110 state via optical pumping after being Sisyphus cooled as presented in Chapter 5. The coherence measurement is the same as in Figure 6.12. The measurement is performed in the presence of a magnetic field created by a current of **(a)** 2 A or **(b)** 4 A resulting in lower limits for the coherence time of (129.0 ± 14.8) µs and (139.9 ± 11.4) µs respectively. The inset shows a close up of the oscillations for short pulse separations.

time constant. Just like for the warmer sample the damping of the oscillation and the exponential rise in depletion signal caused by the movement of the molecules in the trap cannot be separated. The extracted coherence time from a combination of both curves is (134 ± 9) µs. This value is considerably larger than the value obtained for the measurement of movement of the molecules without magnetic fields in Figure 6.10(b). The unexpected fast decay in this measurement could potentially be explained by a background magnetic field causing a slow oscillations of the depletion signal. However, to explain the effect an oscillation frequency of about 3 kHz would be necessary requiring a magnetic field of magnitude 1.3 G. The presence of such a strong magnetic offset field seems unlikely and is also ruled out experimentally with $> 3\,\sigma$ confidence.

The way the magnetic field is created, by placing a coil on top of the vacuum

chamber, is also a source of decoherence since the magnetic field is not perfectly homogeneous at the position of the trap. The size of the homogeneous field region of the trap of about 1.5 mm leads to a gradient of about 0.08 $\frac{\mathrm{G}}{\mathrm{A}}$ over its thickness. The finite size of the trap in the direction perpendicular to the coil axis also leads to inhomogeneities in the magnetic field. At the position of the trap, the field 20 mm removed from the coil axis differs by about 0.62 $\frac{\mathrm{G}}{\mathrm{A}}$ from the centre value. This results in a total gradient in the oscillation frequency induced by the precession in the magnetic field of about 0.7 $\frac{\mathrm{kHz}}{\mathrm{A}}$ over the trap volume. For high currents this puts a significant limit onto the coherence time. For the measurement in Figure 6.12(c) at a current of 6 A the limit is about 40 µs for a unity phase shift whereas for the measurements at 2 A in Figure 6.12(a) and Figure 6.13(a) consequently the value is three times higher with about 110 µs. However, only molecules in the border regions of the trap experience the worst case difference in Zeeman shift so that only a subset of molecules is affected. This can also be seen from the measurements presented in this section which are not limited by the inhomogeneity of the magnetic field but rather by the movement of the molecules in the trap.

6.4 Prospects for longer coherence times

Due to the insensitivity to electric fields much longer coherence times than the ones measured here should be achievable for the $M{=}\pm1$ states of the molecules. The problem of decoherence caused by hyperfine structure can easily be solved by using states with even K_a which do not exhibit hyperfine structure. For uncooled molecules this can be implemented rather quickly as the only change required is the frequency of the UV laser for detection. For cold molecules there is no direct way to transfer the molecules after Sisyphus cooling in the states $|3,3,0\rangle$ and $|4,3,1\rangle$ to a state with even K_a. To do so the molecules can be cooled in e.g. the states $|4,4,0\rangle$ and $|5,4,1\rangle$ from where they can then be transferred to the $|2,2,0\rangle$ state by a very similar scheme as the one presented in Chapter 5. Adjusting the cooling scheme to this new set of states is in principle an easy task also benefiting from the state selectivity of the LIF detection.

A further advantage of using the state $|2,2,0\rangle$ for measuring the coherence time is the K-type doubling of the states. For the $|2,2,0/1\rangle$ states the splitting is only 71 MHz instead of 4.830 GHz as for the $|1,1,0/1\rangle$ states. This means that not only transitions within the upper state of the doublet can be driven with the current equipment, but also transitions into the lower state are possible due to the much smaller frequency difference. Nonetheless, the frequency difference is still large enough to be able to spectroscopically differentiate between the individual transitions in the trap. This way, oscillations of opposite phase should be measurable by first driving the transition from one of the two superposition states of the $M{=}\pm1$ sublevels into one of the two $M{=}0$ sublevel with the first pulse and then coupling molecules to the second $M{=}0$ sublevel. Due to the fact that each transition is dark for one of the two superpositions, for short pulse separations molecules can be depleted by the second pulse and the depletion signal decreases as the molecules precess into the other superposition. This behaviour is exactly the opposite as the one seen in

Figure 6.12 and Figure 6.13. Since coherence measurements of this type are only possible between $M = \pm 1$ and $M=0$ the molecules first have to be transferred into these states from the $M=2$ sublevel which initially is most likely the sublevel with the largest population. Due to the possibility of the LIF detection scheme to detect individual M-sublevels this task should not pose a major problem.

Decoherence due to the collection of geometric phase in the high electric fields in the border region of the trap can potentially be suppressed by applying special voltage configurations at the trap. Typically the offset electric field in the centre of the trap and the longitudinal fields created by the wedge structure of the microstructure electrodes of the trap[3] are of the same order of magnitude. However, it is possible to apply voltage configurations where the offset field is bigger by e.g. a factor of 50 than the longitudinal fields which would greatly suppress the influence of geometric phases and hopefully allow to retain coherence after reflection of the molecules from the border of the trap. A caveat of this method is that the trapping potential is greatly reduced and the method is therefore only available to the coldest molecules.

A further source of decoherence discussed previously in Section 6.1.2 are magnetic fields. A potential offset could easily be zeroed by Helmholtz compensation coils which would at the same time solve the problem of inhomogeneous fields created by the coil used for the experiments presented here. However, inhomogeneous background magnetic fields cannot easily be removed. As the vacuum chamber and other parts were not chosen with focus on their magnetic properties, it is unlikely that very low magnetic fields can be achieved. Fortunately, the states are to some degree protected by their insensitivity to magnetic fields as mentioned before in Section 6.1. Even for the quite pessimistic estimate that the inhomogeneities over the trap volume are on the order of the magnitude of the earth magnetic field, a coherence time of >1 ms is achievable. Since the inhomogeneities are most likely considerably smaller, coherence times of several ms seem realistic.

A challenge still remaining is the search for a measurement sequence which will allow to measure such long coherence times. In the measurements presented here, the molecules leave the addressed homogeneous electric field region on a time scale on the order of 100 µs, not allowing to observe coherence times much longer than this value. However, if a larger fraction of the molecules in the trap can be distributed between $M=\pm 1$ and $M=0$ and the coherence time is sufficiently long, potentially oscillations could reappear after the molecules are reflected by the trap wall and re-enter the homogeneous field region. Of course cooling the molecules into the ultracold regime can also be part of the solution, unfortunately the scaling is unfavourable as the velocity, and therefore the time the molecules spend in the homogeneous electric field region, scales with $\sqrt{T}$. However, for temperatures <1 mK coherence times on the order of 1 ms would be measurable.

[3] In order to avoid large volumes in the trap where the homogeneous electric field and the confining trap field cancel, which would increases molecule losses via Majorana flips, a wedge structure is implemented for the electrodes leading to longitudinal fields parallel to the microstructure [Zep13].

7 Outlook

In this thesis the design and experimental implementation of an optical detection scheme based on laser induced fluorescence for cold formaldehyde molecules is presented. The new detection scheme is then characterised and its state selectivity demonstrated. As a first measurement performed with the LIF detection scheme, optical pumping into the ortho-ground state is demonstrated. Finally, a coherence time is measured on rotational states and a path is outlined on how this time could potentially be increased to over >1 ms. Both experiments heavily rely on the state selectivity of the detection scheme and would be significantly hindered if not impossible by using a QMS for detection. In this section an overview over future prospects for the cooling experiment is provided together with future experiments enabled by the work presented in this thesis.

Improving optoelectrical Sisyphus cooling The main advantage of the detection of formaldehyde molecules via laser induced fluorescence over the previously employed quadrupole mass spectrometer is its state selectivity which even allows to detect single M-sublevels in isolation. This is a particularly powerful tool for the characterisation of the cooling scheme. It greatly facilitates the investigation of IR excitation rates and the rate of the RF cooling transition. It also enables the investigation of trap unloading rates for different states. These capabilities will allow an in-depth analysis of the cooling process and together with a comparison with detailed simulations hopefully lead to further improvements of the optoelectrical Sisyphus cooling scheme. Furthermore, the M-state selectivity of the detection will also allow a comprehensive investigation of molecule dynamics in the electric trap. Currently, the dominating loss mechanism for cooled molecules are most likely non-adiabatic transitions into more weakly or untrapped states in electric field zeroes, i.e. the equivalent to Majorana spin flips. With the possibility to directly measure individual M-sublevels, the influence of the size of the K-type doubling splitting of the rotational states, which determines the linearity of the Stark shift, on Majorana flip rates can be investigated. Another point to be addressed is the enclosure of the molecules at the entrance and exit holes of the trap. With suitable voltage configurations it should be possible to create a potential barrier confining the molecules already during the loading process. Increasing the trap lifetime of the initially loaded uncooled molecules would allow to better incorporate those into the cooling scheme and greatly increase the number of cooled molecules.

Trapping with microwaves In the long run the goal of the experiment is to reach the quantum degenerate regime. To achieve this goal the molecules have to be transferred into another type of trap with a better defined potential landscape. For this there are mainly two options, an optical dipole trap or a MW trap, which both

rely on the same principle of trapping the molecules in a strong electromagnetic field, red-detuned to a transition, creating a confining potential. The main difference lies in the wavelength of the trapping field. An optical dipole trap typically employs an IR laser, which due to its large frequency results in a rather small trap volume. This makes direct loading from the currently employed electrostatic quadrupole guides difficult due to their comparably large size. Therefore, the choice is a MW trap as has been proposed [Dem04] and is also under development in other groups [Dun15].

The design and implementation is currently under investigation in the doctoral thesis of Maximilian Löw. The plan is to build an open resonator to facilitate loading from a quadrupole guide and allow for sufficient optical access. The trap will be operated at 50 GHz which is red-detuned by 90 GHz from the transition $|2,1,2\rangle \leftarrow |1,1,1\rangle$. This creates a trap depth of >1 mK requiring only 20 W pumping power if optimal incoupling and a Finesse of 2500 are assumed. Therefore, the molecules can first be brought into the ultracold temperature regime by conventional optoelectrical Sisyphus cooling in the present electric trap as demonstrated in the past [Pre16]. Subsequently, the molecules will be unloaded and brought into the microwave trap. By applying the ground state preparation technique demonstrated in Chapter 5 the molecules can then be trapped in their ortho ground state in the nodes of the microwave standing wave within the resonator. For further cooling the molecules can be excited via the v_5 vibrational mode to the rotational para ground state $|0,0,0\rangle$. In this state the 50 GHz of the trap are only 25 GHz red-detuned from the $|1,1,1\rangle \leftarrow |0,0,0\rangle$ transition giving a much stronger confinement potential. The cooling transition is driven in the centre of the trap where the MW intensity, and therefore the AC Stark shift is maximal. Therefore, the molecules can only move to lower intensities of the trapping beam and since the confining potential is stronger in the excited state than in the ground state a Sisyphus cooling process can be driven. Eventually after further cooling is applied it is imaginable that the MW trap could be overlapped with an optical dipole trap to decrease the trapping volume and further increase the number density of the molecules.

Cooling towards quantum degeneracy For further cooling there are mainly two options under consideration. The first is sympathetic cooling where the molecules in the MW trap are overlapped with an ultracold atomic cloud at even lower temperatures. Due to collisions molecules and atoms can thermalise decreasing the temperature of the molecules. The second option is evaporative cooling where by lowering the trap depth the hottest molecules are allowed to escape and the remaining molecules re-thermalise at a lower temperature. This is an inherently lossy procedure, which is why a sufficiently high number of molecules would be necessary. Both techniques rely on favourable collision properties of the molecules with elastic collisions dominating over inelastic ones. Collisions between polar molecules are currently under investigation at a second experiment in the Rempe group where Buffer gas cooled molecules are decelerated with a centrifuge decelerator [Che14] and then stored in an electrostatic trap of the same design as the one employed for this work (see Section 2.2.2). For fluoromethane first collisional results have already been obtained [Wu17] and recent investigations in this direction are promising. In principle the system also allows to investigate collisions between cold formaldehyde molecules,

especially if combined with Sisyphus cooling which can readily be implemented at the setup.

Molecule detection in the MW trap For detection of the molecules in the MW trap LIF is not an ideal option. Due to the challenges involved with stray light reduction its seems impossible to implement an in-situ detection covering a large solid angle and at the same time allow for plenty of optical access. A more suitable option is probably resonance-enhanced multiphoton ionisation (REMPI) where molecules are ionized with an intensive UV laser pulse via a multiphoton excitation and the ionization electrons are detected. In the past it has already been shown to be possible to achieve rotational state selectivity with this technique [Par16] and relaxing the condition of a continuous wave detection, high intensity pulsed UV lasers can be employed. With a suitable electrode configuration it seems realistic to efficiently guide the ionisation electrons out of the MW trap region in order to detect them without significantly obstructing optical access.

In the future a promising alternative detection scheme is to use Rydberg atoms due to their large electric dipole moments of thousands of Debye. Förster resonant energy transfer in collisions between the trapped molecules with Rydberg atoms potentially can provide a non-destructive and highly efficient detection method which by repeatedly colliding individual molecules with Rydberg atoms could even approach unity [Zep17, Jar18].

Quantum information processing with molecules A final outlook concerns the coherence measurements presented in the last chapter of this thesis. Immediate steps to increase the coherence time with the present setup are already presented in Section 6.4. In the long run such measurements could be performed in the future MW trap which will provide a much cleaner environment for these experiments. Since the used rotational states are completely insensitive to electric fields and also protected from magnetic fields due to the weak magnetic interaction of closed shell molecules, coherence times well over 1 s seem feasible provided that magnetic fields are compensated in the setup.

By trapping single molecules in an optical lattice and employing the rotational states under investigation here as qubit states, a promising quantum computing platform could be realised [Yu19]. Via their strong permanent dipole moment the molecules can interact and universal quantum gates between neighbouring lattice sites could be realised. First experiments towards this direction could already be performed with the envisioned MW trap even though in this setup the approach is not scalable due to the large wavelength of the 50 GHz radiation. A different approach involves coupling the molecules to a superconducting microwave stripline resonator as has been proposed before [And06, Rab06, Rab07]. These schemes would also greatly benefit from the extreme robustness of the $\pm M$ sublevels of symmetric and slightly asymmetric rotor states shown in this work.

Bibliography

[ACM18] ACME Collaboration. Improved limit on the electric dipole moment of the electron. *Nature* **562**, 355 (2018).

[Aik10] K. Aikawa, D. Akamatsu, M. Hayashi, K. Oasa, J. Kobayashi, P. Naidon, T. Kishimoto, M. Ueda, and S. Inouye. Coherent Transfer of Photoassociated Molecules into the Rovibrational Ground State. *Phys. Rev. Lett.* **105**, 203001 (2010).

[Ake17] N. Akerman, M. Karpov, Y. Segev, N. Bibelnik, J. Narevicius, and E. Narevicius. Trapping of Molecular Oxygen together with Lithium Atoms. *Phys. Rev. Lett.* **119**, 073204 (2017).

[Alb20] R. Albrecht, M. Scharwaechter, T. Sixt, L. Hofer, and T. Langen. Buffer-gas cooling, high-resolution spectroscopy, and optical cycling of barium monofluoride molecules. *Phys. Rev. A* **101**, 013413 (2020).

[And06] A. Andre, D. Demille, J. M. Doyle, M. D. Lukin, S. E. Maxwell, P. Rabl, A. E. Andr, R. J. Schoelkopf, and P. Zoller. A coherent all-electrical interface between polar molecules and mesoscopic superconducting resonators. *Nat. Phys.* **2**, 636 (2006).

[And18] L. Anderegg, B. L. Augenbraun, Y. Bao, S. Burchesky, L. W. Cheuk, W. Ketterle, and J. M. Doyle. Laser cooling of optically trapped molecules. *Nat. Phys.* **14**, 890 (2018).

[And19] L. Anderegg, L. W. Cheuk, Y. Bao, S. Burchesky, W. Ketterle, K.-K. Ni, and J. M. Doyle. An optical tweezer array of ultracold molecules. *Science* **365**, 1156 (2019).

[Ara08] M. Araujo, B. Lasorne, M. J. Bearpark, and M. A. Robb. The Photochemistry of Formaldehyde: Internal Conversion and Molecular Dissociation in a Single Step? *J. Phys. Chem. A* **112**, 7489 (2008).

[Ari76] E. Arimondo and G. Orriols. Nonabsorblng Atomic Coherences by Coherent Two-Photon Transitions in a Three-Level Optical Pumping. *Lett. al Nuovo Cim.* **17**, 333 (1976).

[Aug20] B. L. Augenbraun, Z. D. Lasner, A. Frenett, H. Sawaoka, C. Miller, T. C. Steimle, and J. M. Doyle. Laser-cooled polyatomic molecules for improved electron electric dipole moment searches. *New J. Phys.* **22**, 022003 (2020).

[Bal16] N. Balakrishnan. Perspective: Ultracold molecules and the dawn of cold controlled chemistry. *J. Chem. Phys.* **145**, 150901 (2016).

[Bar12] J. F. Barry, E. S. Shuman, E. B. Norrgard, and D. Demille. Laser Radiation Pressure Slowing of a Molecular Beam. *Phys. Rev. Lett.* **108**, 103002 (2012).

[Bar14] J. F. Barry, D. J. Mccarron, E. B. Norrgard, M. H. Steinecker, and D. Demille. Magneto-optical trapping of a diatomic molecule. *Nature* **512**, 286 (2014).

[Bar18] V. Barbé, A. Ciamei, B. Pasquiou, L. Reichsöllner, F. Schreck, P. S. Zuchowski, and J. M. Hutson. Observation of Feshbach resonances between alkali and closed-shell atoms. *Nat. Phys.* **14**, 881 (2018).

[Bau21] L. Baum, N. B. Vilas, C. Hallas, B. L. Augenbraun, S. Raval, D. Mitra, and J. M. Doyle. Establishing a nearly closed cycling transition in a polyatomic molecule. *Phys. Rev. A* **103**, 043111 (2021).

[Bel09] M. T. Bell and T. P. Softley. Ultracold molecules and ultracold chemistry. *Mol. Phys.* **107**, 99 (2009).

[Bet99] H. Bethlem, G. Berden, and G. Meijer. Decelerating Neutral Dipolar Molecules. *Phys. Rev. Lett.* **83**, 1558 (1999).

[Bet00] H. L. Bethlem, G. Berden, F. M. H. Crompvoets, R. T. Jongma, A. J. A. van Roij, and G. Meijer. Electrostatic trapping of ammonia molecules. *Nature* **406**, 491 (2000).

[Bie16] J. Biesheuvel, J.-P. Karr, L. Hilico, K. S. E. Eikema, W. Ubachs, and J. C. J. Koelemeij. Probing QED and fundamental constants through laser spectroscopy of vibrational transitions in HD^+. *Nat. Comm.* **7**, 10385 (2016).

[Bla19] J. A. Blackmore, L. Caldwell, P. D. Gregory, E. M. Bridge, R. Sawant, J. Aldegunde, J. Mur-Petit, D. Jaksch, J. M. Hutson, B. E. Sauer, M. R. Tarbutt, and S. L. Cornish. Ultracold molecules for quantum simulation: rotational coherences in CaF and RbCs. *Quantum Sci. Technol.* **4**, 014010 (2019).

[Boh17] J. L. Bohn, A. M. Rey, and J. Ye. Cold molecules: Progress in quantum engineering of chemistry and quantum matter. *Science* **357**, 1002 (2017).

[Bor99] M. Born and E. Wolf. Principles of optics: Electromagnetic theory of propagation, interference and diffraction of light. Cambridge University Press, Cambridge, 7th edition (1999).

[Bot19] T. Bothwell, D. Kedar, E. Oelker, J. M. Robinson, S. L. Bromley, W. L. Tew, J. Ye, and C. J. Kennedy. JILA SrI optical lattice clock with uncertainty of 2.0×10^{-18}. *Metrologia* **56**, 065004 (2019).

[Bou96] R. J. Bouwens, J. A. Hammerschmidt, M. M. Grzeskowiak, T. A. Stegink, P. M. Yorba, and W. F. Polik. Pure vibrational spectroscopy of S_0 formaldehyde by dispersed fluorescence. *J. Chem. Phys.* **104**, 460 (1996).

[Brü03] S. Brünken, H. S. P. Müller, F. Lewen, and G. Winnewisser. High accuracy measurements on the ground state rotational spectrum of formaldehyde (H_2CO) up to 2 THz. *Phys. Chem. Chem. Phys.* **5**, 1515 (2003).

[Brü15] R. Brüning, Y. Zhang, M. McLaren, M. Duparré, and A. Forbes. Overlap relation between free-space Laguerre Gaussian modes and step-index fiber modes. *J. Opt Soc. Am. A* **32**, 1678 (2015).

[Bun06] P. R. Bunker and P. Jensen. Molecular Symmetry and Spectroscopy. NRC Research Press, Ottawa, 2nd edition (2006).

[Bur53] B. F. Burke and M. W. P. Strandberg. Zeeman Effect in Rotational Spectra of Asymmetric-Rotor Molecules. *Phys. Rep.* **90**, 303 (1953).

[Bur99] J. P. Burrows, M. Weber, M. Buchwitz, V. Rozanov, A. Ladstätter-Weissenmayer, A. Richter, R. DeBeek, R. Hoogen, K. Bramstedt, K. Eichmann, and M. Eisinger. The Global Ozone Monitoring Experiment (GOME): Mission Concept and First Scientific Results. *J. Atmos. Sci.* **56**, 151 (1999).

[Cai17] W. B. Cairncross, D. N. Gresh, M. Grau, K. C. Cossel, T. S. Roussy, Y. Ni, Y. Zhou, J. Ye, and E. A. Cornell. Precision Measurement of the Electron's Electric Dipole Moment Using Trapped Molecular Ions. *Phys. Rev. Lett.* **119**, 153001 (2017).

[Cai19] W. B. Cairncross and J. Ye. Atoms and molecules in the search for time-reversal symmetry violation. *Nat. Rev. Phys.* **1**, 510 (2019).

[Cal19] L. Caldwell, J. A. Devlin, H. J. Williams, N. J. Fitch, E. A. Hinds, B. E. Sauer, and M. R. Tarbutt. Deep Laser Cooling and Efficient Magnetic Compression of Molecules. *Phys. Rev. Lett.* **123**, 033202 (2019).

[Cal20] L. Caldwell, H. J. Williams, N. J. Fitch, J. Aldegunde, J. M. Hutson, B. E. Sauer, and M. R. Tarbutt. Long Rotational Coherence Times of Molecules in a Magnetic Trap. *Phys. Rev. Lett.* **124**, 063001 (2020).

[Car09] L. D. Carr, D. DeMille, R. V. Krems, and J. Ye. Cold and ultracold molecules: science, technology and applications. *New J. Phys.* **11**, 055049 (2009).

[Che14] S. Chervenkov, X. Wu, J. Bayerl, A. Rohlfes, T. Gantner, M. Zeppenfeld, and G. Rempe. Continuous Centrifuge Decelerator for Polar Molecules. *Phys. Rev. Lett.* **112**, 013001 (2014).

[Che17] T. Chen, W. Bu, and B. Yan. Radiative deflection of a BaF molecular beam via optical cycling. *Phys. Rev. A* **96**, 053401 (2017).

[Che18] L. W. Cheuk, L. Anderegg, B. L. Augenbraun, Y. Bao, S. Burchesky, W. Ketterle, and J. M. Doyle. Λ-Enhanced Imaging of Molecules in an Optical Trap. *Phys. Rev. Lett.* **121**, 083201 (2018).

[Che20] L. W. Cheuk, L. Anderegg, Y. Bao, S. Burchesky, S. S. Yu, W. Ketterle, K.-k. Ni, and J. M. Doyle. Observation of Collisions between Two Ultracold Ground-State CaF Molecules. *Phys. Rev. Lett.* **125**, 043401 (2020).

[Chr19] A. Christianen, M. W. Zwierlein, G. C. Groenenboom, and T. Karman. Photoinduced Two-Body Loss of Ultracold Molecules. *Phys. Rev. Lett.* **123**, 123402 (2019).

[Chu98] S. Chu. The manipulation of neutral particles. *Rev. Mod. Phys.* **70**, 685 (1998).

[Clo83] D. J. Clouthier and D. A. Ramsay. The Spectroscopy of Formaldehyde and Thioformaldehyde. *Ann. Rev. Phys. Chem.* **34**, 31 (1983).

[Cor02] E. A. Cornell and C. E. Wieman. Nobel Lecture: Bose-Einstein condensation in a dilute gas, the first 70 years and some recent experiments. *Rev. Mod. Phys.* **74**, 875 (2002).

[Cro20] J. F. E. Croft, J. L. Bohn, and G. Quéméner. A unified model of ultracold molecular collisions. *Phys. Rev. A* **102**, 033306 (2020).

[CT98] C. N. Cohen-Tannoudji. Manipulating atoms with photons. *Rev. Mod. Phys.* **70**, 707 (1998).

[De 19] L. De Marco, G. Valtolina, K. Matsuda, W. G. Tobias, J. P. Covey, and J. Ye. A degenerate Fermi gas of polar molecules. *Science* **363**, 853 (2019).

[Dei08] J. Deiglmayr, A. Grochola, M. Repp, K. Mörtlbauer, C. Glück, J. Lange, O. Dulieu, R. Wester, and M. Weidemüller. Formation of Ultracold Polar Molecules in the Rovibrational Ground State. *Phys. Rev. Lett.* **101**, 133004 (2008).

[Dem02] D. Demille. Quantum Computation with Trapped Polar Molecules. *Phys. Rev. Lett.* **88**, 067901 (2002).

[Dem03] W. Demtröder. Molekülphysik: Theoretische Grundlagen und experimentelle Methoden. Oldenburg Verlag, München (2003).

[Dem04] D. Demille, D. R. Glenn, and J. Petricka. Microwave traps for cold polar molecules. *Eur. Phys. J. D* **31**, 375 (2004).

[Dic99] J. E. Dickens and W. M. Irrvine. The formaldehyde ortho/para ratio as a probe of dark cloud chemistry and evolution. *ApJ* **518**, 733 (1999).

[Din20] S. Ding, Y. Wu, I. A. Finneran, J. J. Burau, and J. Ye. Sub-Doppler Cooling and Compressed Trapping of YO Molecules at μK Temperatures. *Phys. Rev. X* **10**, 021049 (2020).

[Dob16] E. Dobler, Untersuchungen zur Laser-induzierten Fluoreszenz als Detektionsmethode für ultrakalte Formaldehyd Moleküle, Master's thesis, Max-Planck-Institut für Quantenoptik, Garching, und Fakultät für Physik, Technische Universität München (2016).

[Doy16] J. M. Doyle, B. Friedrich, and E. Narevicius. Physics and Chemistry with Cold Molecules. *ChemPhysChem* **17**, 3581 (2016).

[Dul11] O. Dulieu, R. Krems, M. Weidemüller, and S. Willitsch. Physics and Chemistry of Cold Molecules. *Phys. Chem. Chem. Phys.* **13**, 18703 (2011).

[Dun15] D. P. Dunseith, S. Truppe, R. J. Hendricks, B. E. Sauer, E. A. Hinds, and M. R. Tarbutt. A high quality , efficiently coupled microwave cavity for trapping cold molecules. *J. Phys. B* **48**, 045001 (2015).

[Eng11] B. G. U. Englert, M. Mielenz, C. Sommer, J. Bayerl, M. Motsch, P. Pinkse, G. Rempe, and M. Zeppenfeld. Storage and Adiabatic Cooling of Polar Molecules in a Microstructured Trap. *Phys. Rev. Lett.* **107**, 263003 (2011).

[Eng13] B. G. U. Englert, Sisyphus-Kühlung von polyatomaren Molekülen, Phd thesis, Max-Planck-Institut für Quantenoptik, Garching, und Fakultät für Physik, Technische Universität München (2013).

[Epp97] A. T. J. B. Eppink and D. H. Parker. Velocity map imaging of ions and electrons using electrostatic lenses: Application in photoelectron and photofragment ion imaging of molecular oxygen. *Rev. Sci. Instrum.* **68**, 3477 (1997).

[Esh52] R. Eshbach and M. W. P. Strandberg. Rotational Magnetic Moments of $^1\Sigma$ Molecules. *Phys. Rev.* **85**, 24 (1952).

[Fab77] B. Fabricant, D. Krieger, and J. S. Muenter. Molecular beam electric resonance study of formaldehyde, thioformaldehyde, and ketene. *J. Chem. Phys.* **67**, 1576 (1977).

[Fai81] P. W. Fairchild, K. Shibuya, and E. K. C. Lee. Pressure dependence of fluorescence quantum yields and collision-induced rotational relaxation of single rotational levels of H_2CO ($\tilde{A}^1A_2,\ 4^1$). *J. Chem. Phys.* **75**, 3407 (1981).

[Fio98] A. Fioretti, D. Comparat, A. Crubellier, O. Dulieu, and P. Pillet. Formation of Cold Cs_2 Molecules through Photoassociation. *Phys. Rev. Lett.* **80**, 4402 (1998).

[Fit16] N. J. Fitch and M. R. Tarbutt. Principles and Design of a Zeeman-Sisyphus Decelerator for Molecular Beams. *ChemPhysChem* **17**, 1 (2016).

[Fly65] W. H. Flygare. Molecular Magnetic Moments and Susceptibility in Formaldehyde. *J. Chem. Phys.* **42**, 1563 (1965).

[Fre66] D. E. Freeman and W. Klemperer. Electric Dipole Moment of the $^1A_2$ Electronic State of Formaldehyde. *J. Chem. Phys.* **45**, 52 (1966).

[Glö15a] R. Glöckner, A. Prehn, B. G. U. Englert, G. Rempe, and M. Zeppenfeld. Rotational Cooling of Trapped Polyatomic Molecules. *Phys. Rev. Lett.* **115**, 233001 (2015).

[Glö15b] R. Glöckner, A. Prehn, G. Rempe, and M. Zeppenfeld. Rotational state detection of electrically trapped polyatomic molecules. *New J. Phys.* **17**, 055022 (2015).

[Glö16] R. Glöckner, Rotational-state cooling and detection of trapped CH_3F molecules, Phd thesis, Max-Planck-Institut für Quantenoptik, Garching, und Fakultät für Physik, Technische Universität München (2016).

[Gor66] R. G. Gordon. Spin-Rotation Interactions in Polyatomic Molecules. *J. Chem. Phys.* **44**, 1184 (1966).

[Gor70] W. Gordy and R. L. Cook. Microwave Molecular Spectra. Interscience Publishers, New York (1970).

[Gor17] I. E. Gordon, L. S. Rothman, C. Hill, R. V. Kochanov, Y. Tan, P. F. Bernath, M. Birk, V. Boudon, A. Campargue, K. V. Chance, B. J. Drouin, J. Flaud, R. R. Gamache, J. T. Hodges, D. Jacquemart, V. I. Perevalov, A. Perrin, K. P. Shine, M. H. Smith, J. Tennyson, G. C. Toon, H. Tran, V. G. Tyuterev, A. Barbe, A. G. Császár, V. M. Devi, T. Furtenbacher, J. J. Harrison, J. Hartmann, A. Jolly, T. J. Johnson, T. Karman, I. Kleiner, A. A. Kyuberis, J. Loos, O. M. Lyulin, S. T. Massie, S. N. Mikhailenko, N. Moazzen-ahmadi, H. S. P. Müller, O. V. Naumenko, A. V. Nikitin, O. L. Polyansky, J. V. Auwera, G. Wagner, J. Wilzewski, P. Wcis, S. Yu, and E. J. Zak. The HITRAN2016 molecular spectroscopic database. *J. Quant. Spec. Rad. Trans.* **203**, 3 (2017).

[Gra17] J. M. Gray, J. A. Bossert, Y. Shyur, and H. J. Lewandowski. Measurements of trap dynamics of cold OH molecules using resonance-enhanced multiphoton ionization. *Phys. Rev. A* **96**, 023416 (2017).

[Gre19] P. D. Gregory, M. D. Frye, J. A. Blackmore, E. M. Bridge, R. Sawant, J. M. Hutson, and S. L. Cornish. Sticky collisions of ultracold RbCs molecules. *Nat. Comm.* **10**, 3104 (2019).

[Guo16] M. Guo, B. Zhu, B. Lu, X. Ye, F. Wang, R. Vexiau, N. Bouloufa-maafa, G. Quéméner, O. Dulieu, and D. Wang. Creation of an Ultracold Gas of Ground-State Dipolar $^{23}Na^{87}Rb$ Molecules. *Phys. Rev. Lett.* **116**, 205303 (2016).

[Ham17] M. Hambach, Development of a magneto-optical trap for CaF molecules, Phd thesis, Imperial College London (2017).

[Hen28] V. Henri and S. A. Schou. Struktur und Aktivierung der Molekel des Formaldehyds. Eine Analyse auf Grund des ultravioletten Absorptionsspektrums des Dampfes. *Z. Physik* **49**, 774 (1928).

[Hen82] W. E. Henke, H. L. Selzle, T. R. Hays, E. W. Schlag, and S. H. Lin. Single rotational lifetimes of formaldehyde in a hypersonic jet. *J. Chem. Phys.* **76**, 1327 (1982).

[Hen12] A. B. Henson, S. Gersten, Y. Shagam, J. Narevicius, and E. Narevicius. Observation of Resonances in Penning Ionization Reactions at Sub-Kelvin Temperatures in Merged Beams. *Science* **338**, 234 (2012).

[Her66] G. Herzberg. Molecular Spectra and Molecullar Structure. III. Electronic Spectra and Electronic Structure of Polyatomic Molecules. Van Nostrand Reinhold, New York (1966).

[Her15] I. V. Hertel and C. Schulz. Atoms, Molecules and Optical Physics 2: Molecules and Photons - Spectroscopy and Collisions. Springer, Berlin (2015).

[Hin97] E. A. Hinds. Testing time reversal symmetry using molecules. *Phys. Scr.* **T70**, 34 (1997).

[Hog11] S. D. Hogan, M. Motsch, and F. Merkt. Deceleration of supersonic beams using inhomogeneous electric and magnetic fields. *Phys. Chem. Chem. Phys.* **13**, 18705 (2011).

[Hu19] M.-G. Hu, Y. Liu, D. D. Grimes, Y.-W. Lin, A. H. Gheorghe, R. Vexiau, N. Bouloufa-Maafa, O. Dulieu, T. Rosenband, and K.-K. Ni. Direct observation of bimolecular reactions of ultracold KRb molecules. *Science* **366**, 1111 (2019).

[Hud06] E. R. Hudson, C. Ticknor, B. C. Sawyer, C. A. Taatjes, H. J. Lewandowski, J. R. Bochinski, J. L. Bohn, and J. Ye. Production of cold formaldehyde molecules for study and control of chemical reaction dynamics with hydroxyl radicals. *Phys. Rev. A* **73**, 063404 (2006).

[Hud11] J. J. Hudson, D. M. Kara, I. J. Smallman, B. E. Sauer, M. R. Tarbutt, and E. A. Hinds. Improved measurement of the shape of the electron. *Nature* **473**, 493 (2011).

[Hüt68] W. Hüttner, M. Lo, and W. H. Flygare. Molecular g-Value Tensor, the Molecular Susceptibility Tensor, and the Sign of the Electric Dipole Moment in Formaldehyde. *J. Chem. Phys.* **48**, 1206 (1968).

[Hut12] N. R. Hutzler, H.-i. Lu, and J. M. Doyle. The Buffer Gas Beam: An Intense, Cold, and Slow Source for Atoms and Molecules. *Chem. Rev.* **112**, 4803 (2012).

[Ian13] R. Ianconescu, J. Tatchen, and E. Pollak. On-the-fly semiclassical study of internal conversion rates of formaldehyde. *J. Chem. Phys.* **139**, 154311 (2013).

[Ibr13] M. Ibrügger, Progress in opto-electrical cooling: Implementation of Formaldehyde and of an improved microwave source, Diploma thesis, Max-Planck-Institut für Quantenoptik, Garching, und Fakultät für Physik, Technische Universität München (2013).

[Iwa17] G. Z. Iwata, R. L. Mcnally, and T. Zelevinsky. High-resolution optical spectroscopy with a buffer-gas-cooled beam of BaH molecules. *Phys. Rev. A* **96**, 022509 (2017).

[Jac55] J. A. Jacquez and H. F. Kuppenheim. Theory of the Integrating Sphere. *J. Opt Soc. Am.* **45**, 460 (1955).

[Jar18] F. Jarisch and M. Zeppenfeld. State resolved investigation of Förster resonant energy transfer in collisions between polar molecules and Rydberg atoms. *New J. Phys.* **20**, 113044 (2018).

[Jin12] D. S. Jin and J. Ye. Introduction to Ultracold Molecules: New Frontiers in Quantum and Chemical Physics. *Chem. Rev.* **112**, 4801 (2012).

[Jun04] T. Junglen, T. Rieger, S. A. Rangwala, P. W. H. Pinkse, and G. Rempe. Slow ammonia molecules in an electrostatic quadrupole guide. *Eur. Phys. J. D* **31**, 365 (2004).

[Ket02] W. Ketterle. Nobel lecture: When atoms behave as waves: Bose-Einstein condensation and the atom laser. *Rev. Mod. Phys.* **74**, 1131 (2002).

[Kin43] G. W. King, R. M. Hainer, and P. C. Cross. The Asymmetric Rotor I. Calculation and Symmetry Classification of Energy Levels. *J. Chem. Phys.* **11**, 27 (1943).

[Kir13] M. Kirste, H. Haak, G. Meijer, and S. Y. T. van de Meerakker. A compact hexapole state-selector for NO radicals. *Rev. Sci. Instrum.* **84**, 073113 (2013).

[Koc19] C. P. Koch, M. Lemeshko, and D. Sugny. Quantum control of molecular rotation. *Rev. Mod. Phys.* **91**, 035005 (2019).

[Kon60] K. Kondo and T. Oka. Stark-Zeeman Effects on Asymmetric Top Molecules. Formaldehyde H_2CO. *J. Phys. Soc. Japan* **15**, 307 (1960).

[Kon19] S. S. Kondov, C. Lee, K. H. Leung, C. Liedl, I. Majewska, R. Moszynski, and T. Zelevinsky. Molecular lattice clock with long vibrational coherence. *Nat. Phys.* **15**, 1118 (2019).

[Koz17] I. Kozyryev, L. Baum, K. Matsuda, B. L. Augenbraun, L. Anderegg, A. P. Sedlack, and J. M. Doyle. Sisyphus Laser Cooling of a Polyatomic Molecule. *Phys. Rev. Lett.* **118**, 173201 (2017).

[Kre05] R. V. Krems. Molecules near absolute zero and external field control of atomic and molecular dynamics. *Int. Rev. Phys. Chem.* **24**, 99 (2005).

[Kre09] R. V. Krems, B. Friedrich, and W. C. Stwalley. Cold Molecules: Theory, Experiment, Applications. CRC Press, Boca Raton (2009).

[Kro75] H. W. Kroto. Molecular Rotation Spectra. John Wiley & Sons, London (1975).

[Kuz08] E. Kuznetsova, R. Côté, K. Kirby, and S. F. Yelin. Analysis of experimental feasibility of polar-molecule-based phase gates. *Phys. Rev. A* **78**, 012313 (2008).

[Lac17] J. H. Lacy, C. Sneden, H. Kim, and D. T. Jaffe. H_2, CO, and Dust Absorption through Cold Molecular Clouds. *ApJ* **838**, 66 (2017).

[Lem13] M. Lemeshko, R. V. Krems, J. M. Doyle, and S. Kais. Manipulation of molecules with electromagnetic fields. *Mol. Phys.* **111**, 1648 (2013).

[Liu20a] Y. Liu, D. D. Grimes, M.-G. Hu, and K.-K. Ni. Probing ultracold chemistry using ion spectrometry. *Phys. Chem. Chem. Phys.* **22**, 4861 (2020).

[Liu20b] Y. Liu, M.-g. Hu, M. A. Nichols, D. D. Grimes, T. Karman, H. Guo, and K.-k. Ni. Photo-excitation of long-lived transient intermediates in ultracold reactions. *Nat. Phys.* (2020).

[Man08a] J. G. Mangum, J. Darling, K. M. Menten, and C. Henkel. Formaldehyde Densitometry of Starburst Galaxies. *ApJ* **673**, 832 (2008).

[Man08b] D. Manura and D. Dahl. SIMION (R) 8.1 User Manual. Scientific Instrument Services, Inc. Ringoes, New Jersey (2008).

[Mar01] J. P. Marangos, Electromagnetically Induced Transparency, in Handb. Opt. Vol. IV Fiber Opt. Nonlinear Opt., chapter 23, McGraw-Hill, New York, 2nd edition (2001).

[Max05] S. E. Maxwell, N. Brahms, R. DeCarvalho, D. R. Glenn, J. S. Helton, S. V. Nguyen, D. Patterson, J. Petricka, D. Demille, and J. M. Doyle. High-Flux Beam Source for Cold, Slow Atoms or Molecules. *Phys. Rev. Lett.* **95**, 173201 (2005).

[May12] M. Mayle, B. P. Ruzic, and J. L. Bohn. Statistical aspects of ultracold resonant scattering. *Phys. Rev. A* **85**, 062712 (2012).

[May13] M. Mayle, G. Quéméner, B. P. Ruzic, and J. L. Bohn. Scattering of ultracold molecules in the highly resonant regime. *Phys. Rev. A* **87**, 012709 (2013).

[McC18] D. J. McCarron, M. H. Steinecker, Y. Zhu, and D. Demille. Magnetic Trapping of an Ultracold Gas of Polar Molecules. *Phys. Rev. Lett.* **121**, 013202 (2018).

[Men15] C. Meng, A. P. P. van der Poel, C. Cheng, and H. L. Bethlem. Femtosecond laser detection of Stark-decelerated and trapped methylfluoride molecules. *Phys. Rev. A* **92**, 023404 (2015).

[Mie10] M. Mielenz, Speichern von polaren Molekülen in einer mikrostrukturierten elektrischen Falle, Diploma thesis, Julius-Maximilians-Universität Würzburg (2010).

[Mil78] R. G. Miller and E. K. C. Lee. Single vibronic level photochemistry of formaldehydes in the $\tilde{A}^1A_2$ state: Radiative and nonradiative processes in H_2CO, HDCO, and D_2CO. *J. Chem. Phys.* **68**, 4448 (1978).

[Mit20] D. Mitra, N. B. Vilas, C. Hallas, L. Anderegg, B. L. Augenbraun, L. Baum, C. Miller, S. Raval, and J. M. Doyle. Direct Laser Cooling of a Symmetric Top Molecule. *Science* **369**, 1366 (2020).

[Möh85] G. R. Möhlmann. Formaldehyde Detection in Air by Laser-Induced Fluorescence. *Appl. Spectrosc.* **39**, 98 (1985).

[Mol14] P. K. Molony, P. D. Gregory, Z. Ji, B. Lu, M. P. Köppinger, C. R. L. Sueur, C. L. Blackley, J. M. Hutson, and S. L. Cornish. Creation of Ultracold Molecules in the Rovibrational Ground State. *Phys. Rev. Lett.* **113**, 255301 (2014).

[Moo83] C. B. Moore and J. C. Weisshaar. Formaldehyde Photochemistry. *Annu. Rev. Phys. Chem.* **34**, 525 (1983).

[Mot09] M. Motsch, Cold Guided Beams of Polar Molecules, Phd thesis, Technical University of Munich (2009).

[Mou75] D. C. Moule and A. D. Walsh. Ultraviolet Spectra and Excited States of Formaldehyde. *Chem. Rev.* **75**, 67 (1975).

[Mul55] R. S. Mulliken. Report on Notation for the Spectra of Polyatomic Molecules. *J. Chem. Phys.* **23**, 1997 (1955).

[Mül17] H. S. P. Müller and F. Lewen. Submillimeter spectroscopy of $H_2C^{17}O$ and a revisit of the rotational spectra of $H_2C^{18}O$ and $H_2C^{16}O$. *J. Mol. Spec.* **331**, 28 (2017).

[Nem94] G. Nemes and A. E. Siegman. Measurement of all ten second-order moments of an astigmatic beam by the use of rotating simple astigmatic (anamorphic) optics. *J. Opt Soc. Am. A* **8**, 2257 (1994).

[Ni08] K. Ni, S. Ospelkaus, M. H. G. de Miranda, A. Pe'er, B. Neyenhuis, J. J. Zirbel, S. Kotochigova, P. S. Julienne, D. S. Jin, and J. Ye. A High Phase-Space-Density Gas of Polar Molecules. *Science* **322**, 231 (2008).

[Ni10] K. Ni, S. Ospelkaus, D. Wang, G. Quéméner, B. Neyenhuis, M. H. G. de Miranda, J. L. Bohn, J. Ye, and D. S. Jin. Dipolar collisions of polar molecules in the quantum regime. *Nature* **464**, 1324 (2010).

[Nor16a] E. B. Norrgard, D. J. McCarron, M. H. Steinecker, M. R. Tarbutt, and D. DeMille. Submillikelvin Dipolar Molecules in a Radio-Frequency Magneto-Optical Trap. *Phys. Rev. Lett.* **116**, 063004 (2016).

[Nor16b] E. B. Norrgard, N. Sitaraman, J. F. Barry, D. J. Mccarron, M. H. Steinecker, and D. DeMille. In-vacuum scattered light reduction with cupric oxide surfaces for sensitive fluorescence detection. *Rev. Sci. Instrum.* **87**, 053119 (2016).

[Pan19] C. D. Panda, C. Meisenhelder, M. Verma, D. G. Ang, J. Chow, Z. Lasner, X. Wu, D. DeMille, J. M. Doyle, and G. Gabrielse. Attaining the shot-noise-limit in the ACME measurement of the electron electric dipole moment. *J. Phys. B At. Mol. Opt. Phys.* **52**, 235003 (2019).

[Par15] J. W. Park, S. A. Will, and M. W. Zwierlein. Ultracold Dipolar Gas of Fermionic $^{23}Na^{40}K$ Molecules in Their Absolute Ground State. *Phys. Rev. Lett.* **114**, 205302 (2015).

[Par16] G. B. Park, B. C. Kru, S. Meyer, A. M. Wodtke, and T. Scha. A 1+1' resonance-enhanced multiphoton ionization scheme for rotationally state-selective detection of formaldehde via the $\tilde{A}^1A_2 \leftarrow \tilde{X}^1A_1$ transition. *Phys. Chem. Chem. Phys.* **18**, 22355 (2016).

[Par17] J. W. Park, Z. Z. Yan, H. Loh, S. A. Will, and M. W. Zwierlein. Second-scale nuclear spin coherence time of ultracold $^{23}Na^{40}K$ molecules. *Science* **357**, 372 (2017).

[Pau53] W. Paul and H. Steinwedel. Ein neues Massenspektrometer ohne Magnetfeld. *Z. Naturforsch.* **8a**, 448 (1953).

[Pet18] M. Petzold, P. Kaebert, P. Gersema, M. Siercke, and S. Ospelkaus. A Zeeman slower for diatomic molecules. *New J. Phys.* **20**, 042001 (2018).

[Phi98] W. D. Phillips. Laser cooling and trapping of neutral atoms. *Rev. Mod. Phys.* **70**, 721 (1998).

[Pin80] J. P. Pinto, G. R. Gladstone, and Y. Yung. Photochemical Production of Formaldehyde in Earth's Primitive Atmosphere. *Science* **210**, 183 (1980).

[Pre12] A. Prehn, Cooling of an electrically trapped gas of Fluoromethane, Diploma thesis, Max-Planck-Institut für Quantenoptik, Garching, und Fakultät für Physik, Technische Universität München (2012).

[Pre16] A. Prehn, M. Ibrügger, R. Glöckner, G. Rempe, and M. Zeppenfeld. Optoelectrical Cooling of Polar Molecules to Submillikelvin Temperatures. *Phys. Rev. Lett.* **116**, 063005 (2016).

[Pre17] A. Prehn, R. Glöckner, G. Rempe, and M. Zeppenfeld. Fast, precise, and widely tunable frequency control of an optical parametric oscillator referenced to a frequency comb. *Rev. Sci. Instrum.* **88**, 033101 (2017).

[Pre18] A. V. Prehn, An Ultracold Gas of Electrically Trapped Formaldehyde, Phd thesis, Max-Planck-Institut für Quantenoptik, Garching, und Fakultät für Physik, Technische Universität München (2018).

[QP12] M. Quintero-Pérez, P. Jansen, and H. L. Bethlem. Velocity map imaging of a slow beam of ammonia molecules inside a quadrupole guide. *Phys. Chem. Chem. Phys.* **14**, 9630 (2012).

[Rab06] P. Rabl, D. Demille, J. M. Doyle, M. D. Lukin, R. J. Schoelkopf, and P. Zoller. Hybrid Quantum Processors: Molecular Ensembles as Quantum Memory for Solid State Circuits. *Phys. Rev. Lett.* **97**, 033003 (2006).

[Rab07] P. Rabl and P. Zoller. Molecular dipolar crystals as high-fidelity quantum memory for hybrid quantum computing. *Phys. Rev. A* **76**, 042308 (2007).

[Ran03] S. A. Rangwala, T. Junglen, T. Rieger, P. W. H. Pinkse, and G. Rempe. Continuous source of translationally cold dipolar molecules. *Phys. Rev. A* **67**, 043406 (2003).

[Rea82] W. G. Read and W. H. Flygare. The microwave spectrum and molecular structure of the acetylene-HF complex. *J. Chem. Phys.* **76**, 2238 (1982).

[Saf18] M. S. Safronova, D. Budker, D. Demille, D. F. J. Kimball, A. Derevianko, and C. W. Clark. Search for new physics with atoms and molecules. *Rev. Mod. Phys.* **90**, 025008 (2018).

[Sag05] J. M. Sage, S. Sainis, T. Bergeman, and D. DeMille. Optical Production of Ultracold Polar Molecules. *Phys. Rev. Lett.* **94**, 203001 (2005).

[Sár14] L. Sárkány, P. Weiss, H. Hattermann, and J. Fortágh. Controlling the magnetic-field sensitivity of atomic-clock states by microwave dressing. *Phys. Rev. A* **90**, 053416 (2014).

[Sch93] W. A. Schutte, L. J. Allamandola, and S. A. Sandford. Formaldehyde and Organic Molecule Production in Astrophysical Ices at Cryogenic Temperatures. *Science* **259**, 1143 (1993).

[Sch16] H. C. Schewe, D. Zhang, G. Meijer, R. W. Field, B. G. Sartakov, G. C. Groenenboom, A. van der Avoird, and N. Vanhaecke. Stark Interference of Electric and Magnetic Dipole Transitions in the A - X Band of OH. *Phys. Rev. Lett.* **116**, 153001 (2016).

[Scu97] M. O. Scully and M. S. Zubairy. Quantum Optics. Cambridge University Press, Cambridge (1997).

[See18] F. Seesselberg, N. Buchheim, Z.-k. Lu, T. Schneider, X.-y. Luo, E. Tiemann, I. Bloch, and C. Gohle. Modeling the adiabatic creation of ultracold polar ^{23}Na^{40}K molecules. *Phys. Rev. A* **97**, 013405 (2018).

[Shi67] T. Shigenari. Magnetic Hyperfine Structure and Zeeman Effect of the $J = 1$, $K = 1$ Transition of H_2CO. *J. Phys. Soc. Japan* **23**, 404 (1967).

[Shi81] K. Shibuya, P. W. Fairchild, and E. K. C. Lee. Single rotational level fluorescence quantum yields , radiative lifetimes , and nonradiative decay rates of S_1 D_2CO and H_2CO ($\tilde{A}^1A_2$, 4^1): Rotational dependence. *J. Chem. Phys.* **75**, 3397 (1981).

[Shu10] E. S. Shuman, J. F. Barry, and D. Demille. Laser cooling of a diatomic molecule. *Nature* **467**, 820 (2010).

[Sie86] A. E. Siegman. Lasers. University Science Books, Sausalito, California (1986).

[Sie98] A. E. Siegman. How to (Maybe) Measure Laser Beam Quality. *OSA TOPS* **17**, 184 (1998).

[Som11] C. Sommer, Construction and Operation of a Cryogenic Source for Cold Polar Molecules, Phd thesis, Max-Planck-Institut für Quantenoptik, Garching, und Fakultät für Physik, Technische Universität München (2011).

[Spa16] B. Spaun, B. Changala, D. Patterson, B. J. Bjork, O. H. Heckl, J. M. Doyle, and J. Ye. Continuous probing of cold complex molecules with infrared frequency comb spectroscopy. *Nature* **533**, 517 (2016).

[Tak63] K. Takagi and T. Oka. Millimeter Wave Spectrum of Formaldehyde. *J. Phys. Soc. Japan* **18**, 1174 (1963).

[Tak14] T. Takekoshi, L. Reichsöllner, A. Schindewolf, J. M. Hutson, C. R. Le Sueur, O. Dulieu, F. Ferlaino, R. Grimm, and H.-C. Nägerl. Ultracold Dense Samples of Dipolar RbCs Molecules in the Rovibrational and Hyperfine Ground State. *Phys. Rev. Lett.* **113**, 205301 (2014).

[Tar15] M. R. Tarbutt. Magneto-optical trapping forces for atoms and molecules with complex level structures. *New J. Phys.* **17**, 015007 (2015).

[Tha64] P. Thaddeus, L. C. Krisher, and J. H. N. Loubser. Hyperfine Structure in the Microwave Spectrum of HDO, HDS, CH_2O, and CHDO: Beam-Maser Spectroscopy on Asymmetric-Top Molecules. *J. Chem. Phys.* **40**, 257 (1964).

[Tha14] R. Thalman, K. J. Zarzana, M. A. Tolbert, and R. Volkamer. Rayleigh scattering cross-section measurements of nitrogen, argon, oxygen and air. *J. Quant. Spec. Rad. Trans.* **147**, 171 (2014).

[Tow75] C. H. Townes and A. L. Schawlow. Microwave Spectroscopy. Dover Publications, New York (1975).

[Tro09] N. Troscompt, A. Faure, L. Wiesenfeld, C. Ceccarelli, and P. Valiron. Rotational excitation of formaldehyde by hydrogen molecules: ortho-H_2CO at low temperature. *A&A* **493**, 687 (2009).

[Tru13] S. Truppe, R. J. Hendricks, S. K. Tokunaga, H. J. Lewandowski, M. G. Kozlov, C. Henkel, E. A. Hinds, and M. R. Tarbutt. A search for varying fundamental constants using hertz-level frequency measurements of cold CH molecules. *Nat. Comm.* **4**, 2600 (2013).

[Tru17a] S. Truppe, H. J. Williams, N. J. Fitch, M. Hambach, T. E. Wall, E. A. Hinds, B. E. Sauer, and M. R. Tarbutt. An intense, cold, velocity-controlled molecular beam by frequency-chirped laser slowing. *New J. Phys.* **19**, 022001 (2017).

[Tru17b] S. Truppe, H. J. Williams, M. Hambach, L. Caldwell, N. J. Fitch, E. A. Hinds, B. E. Sauer, and M. R. Tarbutt. Molecules cooled below the Doppler limit. *Nat. Phys.* **13**, 1173 (2017).

[Tru19] S. Truppe, S. Marx, S. Kray, M. Doppelbauer, S. Hofsäss, H. C. Schewe, N. Walter, J. Pérez-Ríos, B. G. Sartakov, and G. Meijer. Spectroscopic characterization of aluminum monofluoride with relevance to laser cooling and trapping. *Phys. Rev. A* **100**, 052513 (2019).

[Tsc15] T. V. Tscherbul and R. V. Krems. Tuning Bimolecular Chemical Reactions by Electric Fields. *Phys. Rev. Lett.* **115**, 023201 (2015).

[Tud06] M. Tudorie, P. Cacciani, J. Cosléou, F. Herlemont, M. Khelkhal, C. Puzzarini, S. Maret, and C. Kahane. Nuclear spin conversion of formaldehyde in protostar environments induced by non reactive collisions. *A&A* **453**, 755 (2006).

[Vac88] P. H. Vaccaro, F. Temps, S. Halle, J. L. Kinsey, and R. W. Field. Polarization-detected transient gain studies of relaxation processes in $v_4 = 1$ $\tilde{A}^1A_2$ formaldehyde-h_2. *J. Chem. Phys.* **88**, 4819 (1988).

[Vac89] P. H. Vaccaro, A. Zabludoff, M. E. Carrera-Patino, J. L. Kinsey, and R. W. Field. High precision dipole moments in $\tilde{A}^1A_2$ formaldehyde determined via Stark quantum beat spectroscopy. *J. Chem. Phys.* **90**, 4150 (1989).

[vB09] L. D. van Buuren, C. Sommer, M. Motsch, S. Pohle, M. Schenk, J. Bayerl, P. W. H. Pinkse, and G. Rempe. Electrostatic Extraction of Cold Molecules from a Cryogenic Reservoir. *Phys. Rev. Lett.* **102**, 033001 (2009).

[vD78] J. M. F. van Dijk, M. J. H. Kemper, J. H. M. Kerp, and H. M. Buck. Ab initio CI calculation of the radiationless transition of the $^1(n\pi^*)$ state of formaldehyde. *J. Chem. Phys.* **69**, 2462 (1978).

[vdM12] S. Y. T. van de Meerakker, H. L. Bethlem, N. Vanhaecke, and G. Meijer. Manipulation and Control of Molecular Beams. *Chem. Rev.* **112**, 4828 (2012).

[Vog20] K. K. Voges, P. Gersema, T. Hartmann, T. A. Schulze, A. Zenesini, and S. Ospelkaus. Formation of ultracold weakly bound dimers of bosonic $^{23}Na^{39}K$. *Phys. Rev. A* **101**, 042704 (2020).

[vZ14] A. von Zastrow, J. Onvlee, S. N. Vogels, G. C. Groenenboom, A. van der Avoird, and S. Y. T. van de Meerakker. State-resolved diffraction oscillations imaged for inelastic collisions of NO radicals with He, Ne and Ar. *Nat. Chem.* **6**, 216 (2014).

[Wal16] T. E. Wall. Preparation of cold molecules for high-precision measurements. *J. Phys. B At. Mol. Opt. Phys.* **49**, 243001 (2016).

[Wan13] B. X. Wang, M. Kirste, G. Meijer, and S. Y. T. van de Meerakker. Stark Deceleration of NO Radicals. *Z. Phys. Chem.* **227**, 1595 (2013).

[Wei79] J. C. Weisshaar and C. B. Moore. Collisionless nonradiative decay rates of single rotational levels of S_1 formaldehyde. *J. Chem. Phys.* **70**, 5135 (1979).

[Wei80] J. C. Weisshaar and C. B. Moore. Isotope, electric field, and vibrational state dependence of single rotational level lifetimes of S_1. *J. Chem. Phys.* **72**, 5415 (1980).

[Wei11] Q. Wei, S. Kais, B. Friedrich, and D. Herschbach. Entanglement of polar symmetric top molecules as candidate qubits. *J. Chem. Phys.* **135**, 154102 (2011).

[Wes17] C. M. Western. Journal of Quantitative Spectroscopy & Radiative Transfer PGOPHER: A program for simulating rotational, vibrational and electronic spectra. *J. Quant. Spectrosc. Radiat. Transf.* **186**, 221 (2017).

[Wil18] H. J. Williams, L. Caldwell, N. J. Fitch, S. Truppe, J. Rodewald, E. A. Hinds, B. E. Sauer, and M. R. Tarbutt. Magnetic Trapping and Coherent Control of Laser-Cooled Molecules. *Phys. Rev. Lett.* **120**, 163201 (2018).

[Wu17] X. Wu, T. Gantner, M. Koller, M. Zeppenfeld, S. Chervenkov, and G. Rempe. A cryofuge for cold-collision experiments with slow polar molecules. *Science* **358**, 645 (2017).

[Wu20] X. Wu, Z. Han, J. Chow, D. G. Ang, C. Meisenhelder, C. D. Panda, E. P. West, G. Gabrielse, J. M. Doyle, and D. DeMille. The metastable $Q^3\Delta_2$ state of ThO : a new resource for the ACME electron EDM search. *New J. Phys.* **22**, 023013 (2020).

[Xu18] S. Xu, Y. Yin, R. Gu, M. Xia, L. Xu, L. Chen, Y. Xia, and J. Yin. Note: Sensitive fluorescence detection through minimizing the scattering light by anti-reflective nanostructured materials. *Rev. Sci. Instrum.* **89**, 046103 (2018).

[Xu19] S. Xu, M. Xia, Y. Yin, R. Gu, Y. Xia, and J. Yin. Determination of the normal $A^2\Pi$ state in MgF with application to direct laser cooling of molecules. *J. Chem. Phys.* **150**, 084302 (2019).

[Yel06] S. F. Yelin, K. Kirby, and R. Coté. Schemes for robust quantum computation with polar molecules. *Phys. Rev. A* **74**, 050301(R) (2006).

[Yu19] P. Yu, L. W. Cheuk, I. Kozyryev, and J. M. Doyle. A scalable quantum computing platform using symmetric-top molecules. *New J. Phys.* **21**, 093049 (2019).

[Zep09] M. Zeppenfeld, M. Motsch, P. Pinkse, and G. Rempe. Optoelectrical cooling of polar molecules. *Phys. Rev. A* **80**, 041401(R) (2009).

[Zep12] M. Zeppenfeld, B. G. U. Englert, R. Glöckner, A. Prehn, M. Mielenz, C. Sommer, L. D. van Buuren, M. Motsch, and G. Rempe. Sisyphus cooling of electrically trapped polyatomic molecules. *Nature* **491**, 570 (2012).

[Zep13] M. Zeppenfeld, Electric Trapping and Cooling of Polyatomic Molecules, Phd thesis, Max-Planck-Institut für Quantenoptik, Garching, und Fakultät für Physik, Technische Universität München (2013).

[Zep17] M. Zeppenfeld. Nondestructive detection of polar molecules via Rydberg atoms. *EPL* **117**, 13002 (2017).

[Zho20] Y. Zhou, Y. Shagam, W. B. Cairncross, K. B. Ng, T. S. Roussy, T. Grogan, K. Boyce, A. Vigil, M. Pettine, T. Zelevinsky, J. Ye, and E. A. Cornell. Second-Scale Coherence Measured at the Quantum Projection Noise Limit with Hundreds of Molecular Ions. *Phys. Rev. Lett.* **124**, 053201 (2020).

List of Publications

High-resolution "Magic"-Field Spectroscopy on Trapped Polyatomic Molecules
A. Prehn, M. Ibrügger, G. Rempe, and M. Zeppenfeld.
Phys. Rev. Lett. **127**, 173602 (2021).

An experimental toolbox for the generation of cold and ultracold polar molecules
M. Zeppenfeld, T. Gantner, R. Glöckner, M. Ibrügger, M. Koller, A. Prehn, X. Wu, S. Chervenkov, and G. Rempe.
J. Phys.: Conf. Ser. **793**, 012035 (2017).

Optoelectrical cooling of polar molecules to submillikelvin temperatures
A. Prehn, M. Ibrügger, R. Glöckner, G. Rempe, and M. Zeppenfeld.
Phys. Rev. Lett. **116**, 063005 (2016).

Acknowledgements

Finally, I would like to acknowledge the people that have contributed over the years in various ways to the successful completion of this thesis.

First of all, I would like to thank my thesis advisor Gerhard Rempe for giving me the opportunity to work on the cutting edge research that is the field of ultracold molecules. Not only did he give me the chance to do my diploma thesis in his group but also welcomed me back to continue my work for a doctoral thesis. By leaving us great independence and offering guidance whenever needed, he provided us with ideal conditions to pursue our research. With his enthusiasm and interest in our work he always found time for discussions and stimulated further in-depth investigations with his critical thinking and accurate questions.

Secondly, I am thankful to Martin Zeppenfeld without whom there would be no 'Ultrastark' experiment. With his one of a kind creativity he provided a constant stream of ideas invaluable for the success of the experiment and also the completion of this thesis. I am especially grateful for the dedication he showed towards supporting me in overcoming one of the main hurdles to completing this thesis, the suppression of stray light. His efforts and support also until late in the evening were much appreciated. Over the course of the years I could learn many things from him, covering diverse topics such as molecule theory or how to approach a technical problem. Furthermore, I also thank him for carefully proof reading this thesis.

I also would like to thank the remaining 'Ultrastark' team I got to work with over the years. Barbara Englert introduced me to the world of molecules already during my diploma thesis. She never failed to make me laugh and I would like to thank her for the great times we had when sharing an office. Rosa Glöckner's curious nature and her willingness to always discuss and provide valuable input made it a pleasure to work with her. Alexander Prehn I want to thank for the collegial and successful cooperation over several years. He showed me many of the intricacies of the setup and his numerous improvements to the experimental apparatus made my life in the lab much easier also after he left the group. I also would like to thank the Master students Markus Krottenmüller, Erich Dobler and Fabian Salamon. Markus inherited me his microstructure project and left with an excellent basis established, allowing me to seamlessly continue the development. Erich performed the first measurement showing the feasibility of the LIF detection method. His independent way of working and his solution oriented mind made him an ideal student and I always enjoyed discussing his challenging questions. Fabian is working on the future of the cooling experiment and in the short time we shared an office he impressed me with his dedication and numerous, on point questions. Maximilian Löw I would like to thank for the nice working atmosphere and all the help he provided towards finishing this thesis. His seemingly infinite patience and

his persistence will certainly allow him to achieve good results even with the difficult situation of having to manage the experiment alone.

Special thanks go towards the former and current technicians of the group Josef Bayerl, Franz Denk, Helmuth Stehbeck, Tobias Urban, Johannes Siegl, Florian Furchtsam and Thomas Wiesmeier. Without them the realisation of such a complex setup as the LIF detection would have been impossible. With their technical ingenuity they provided invaluable support during the design and setting up phase of the experiment but were also available for every technical emergency that came up. I also enjoyed all of our informal conversations lightening up the day. I also want to thank Iris Anneser for her organisational support.

Thank you to the 'cryofuge superteam' made up from Sotir Chervenkov, Xing Wu, Thomas Gantner, Manuel Koller, Ferdinand Jarisch, Isabel Rabey, Florian Jung and Boom Phrompao for their helpfulness and friendship. They provided a great address to go to whenever I was facing a technical problem or was only looking for moral support. Thank you to Max and Izzy for proofreading my thesis in such a quick an efficient manner.

The remaining Rempe group I would like to thank for their openness to discussion, helpfulness, and in general the nice working atmosphere they provided. I very much enjoyed our 'class trips' to DPG or the group retreats and all other off-work activities like mountain trips, barbecues, and so on.

I also want to thank Ralf Meyer, Claudia Paulus, and Linda Mora at WSI for supporting me with our microstructure project and always finding time to discuss and explain my numerous requests and questions.

Finally, I thank my friends, family, and wife for their support over all these years. Without them finishing this thesis would have been an ordeal and they never failed to build me up after failures in the lab and provided distraction whenever needed. In particular Karol's unwavering belief in my capabilities and her encouragements were a great help and enabled me to stay motivated until the end.